

Novel electrolyte formulations for lithium metal batteries

ZHENGKUN XIE

Graduate School of Science and Technology

Hirosaki University

2020

ABSTRACT

Rechargeable lithium-metal batteries (LMBs) have been recognized as one of attractive energy storage devices since Li metal has an ultrahigh specific capacity as well as an ultralow standard negative electrochemical potential. However, due to the high reactivity of Li metal, Li dendrites are always generated in LMBs to shorten the cycle life of LMBs, which impedes the widespread deployment of high-energy density LMBs. Recently, tremendous efforts including the applications of artificial current collector substrate, anode coating layers, host matrix, solid-state electrolytes, concentrated electrolytes, electrolyte additives, and so on, have been devoted to the protection of Li metal anode to extend the cycle life of LMBs. Among all of those strategies, owing to the low cost and easy processing, the novel electrolyte formulations are considered as the most promising way to simply but effectively improve the performance of LMBs. In this dissertation, some novel electrolyte formulations, i.e., quasi-solid-state electrolyte, solid-state electrolyte, practical liquid electrolyte were developed for the high-energy density LMBs. The effects of various electrolytes on inducing a stable and robust electrode/electrolyte interfaces, decreasing the parasitic reactions between metallic Li and electrolytes, suppressing the growth of lithium dendrites, and prolonging the cycle life of LMBs were elucidated. These electrolyte formulations with broad compatibility could be considered as the candidates for the next-generation LMBs designs. The main progress can be briefly summarized as follows:

Firstly, a flexible poly-(ethylene oxide) (PEO)-lithium bis(trifluoromethanesulfonyl)imide) (LiTFSI) polymer electrolyte assisted with a bifunctional ionic liquid (IL) of tetrabutylphosphonium 2-hydroxypyridine (TBPHP) as well as a garnet-type fast-ion conducting ceramic of $\text{Li}_{6.4}\text{La}_3\text{Zr}_{1.4}\text{Ta}_{0.6}\text{O}_{12}$ (LLZTO) was fabricated via a solvent-free procedure and applied for the LMBs. It is found that the tetrabutylphosphonium cation (TBP^+) and 2-hydroxypyridine

anion (HP^-) of IL effectively tuned the crystallinity of PEO and enhanced lithium ion (Li^+) transference, respectively, and the TBPHP and LLZTO played a synergistic role in improving the performance of electrolyte. Meanwhile, the density functional theory (DFT) study was performed to understand the interaction between TBPHP and LiTFSI. As a result, the obtained $\text{PEO}_8\text{-LiTFSI-TBPHP-12.5\% LLZTO}$ composite SPE possessed a high ionic conductivity of $9.39 \times 10^{-4} \text{ S}\cdot\text{cm}^{-1}$ at 50°C and a wide electrochemical stability window (more than 5 V) with significantly promoted uniform Li plating/stripping properties. The LMBs assembled with quasi-solid-state electrolyte and LiFePO_4 cathode rendered excellent cycling stability with a high discharge capacity above $150 \text{ mAh}\cdot\text{g}^{-1}$ even after 100 cycles at 0.2 C and 50°C . Besides, the fabricated flexible pouch cell showed excellent performance. It is expected that such a bifunctional ionic liquid and conducting ceramic co-assisted polymer composite could be a promising solid electrolyte for the next generation of safe LMBs.

Secondly, in order to develop a solid-state electrolyte with lower cell operating temperature, faster ion conductivity, higher electrochemical as well as thermal stability, and excellent electrode/electrolyte compatibility for high-performance LMBs, a flexible and stable composite polymer electrolyte (CPE) composed of poly(vinylidene fluoride-hexafluoropropylene) (PVDF-HFP)- $\text{Li}_{6.4}\text{La}_3\text{Zr}_{1.4}\text{Ta}_{0.6}\text{O}_{12}$ (LLZTO) sandwiched by PEO-LiTFSI polymer skin layers in two sides (denoted as sandwich-type CPE) is fabricated and applied for the LMBs. In such a CPE membrane, the PEO-LiTFSI polymer layers not only ameliorated the ion conductivity of PVDF-HFP-LLZTO, but also improved the intimate contact with the electrodes. Meanwhile, the crystallinity of PEO as well as the PVDF-HFP polymer matrix was significantly reduced owing to the cross-linking of them at the interfacial sections so that the obtained CPE membrane had faster Li^+ ions transportation ability. Assembled with this sandwich-type CPE, the all-solid-state LiFePO_4 (Areal capacity: 1.5 mAh cm^{-2}) |Li-metal battery exhibited excellent rate performance and cycle

stability with a discharge capacity of 120.01 mAh g⁻¹ even after 300 cycles at 40 °C, also, other two all-solid-state LiCoO₂|Li-metal and LiNi_{1/3}Mn_{1/3}Co_{1/3}O₂|Li-metal batteries showed high voltage stability along with the satisfied energy density as well as excellent cycle performance. Moreover, the fabricated flexible pouch cell also exhibited outstanding performance, indicating its feasibility for the next generation of flexible LMBs.

Thirdly, to achieve a higher energy density with better compatibility in the practical applications of LMBs, a novel and reliable electrolyte additive, 2-Fluoropyridine (2-FP), was successfully applied to enhance the stability of different commercial liquid electrolytes and effectively improve the performance of LMBs. The 2-FP additive was found to play a critical role in the decrease of Li nucleation as well as deposition overpotential, and finally suppressing the Li-dendrites. As a result, the high-voltage LiNi_{1/3}Mn_{1/3}Co_{1/3}O₂ cathode (1.5 mAh cm⁻²)|Li metal cell using the commercial carbonate-based LiPF₆ electrolyte with 2% of 2-FP additive exhibited a stable capacity retention of 67.6% even after 300-cycle test with a coulombic efficiency as high as 99.89 % at 0.75 mA cm⁻². Meanwhile, in the case using another commercial ether-based LiTFSI electrolyte with it, the LiFePO₄ cathode (1.5 mAh cm⁻²)|Li metal cell also maintained long-term stability with high coulombic efficiency and the discharge capacity even with a small electrolyte amount and a high current density of 1.5 mA cm⁻². By combining the surface analysis with quantum chemistry calculations, it is verified that the stabilization effect by introduction of this additive at the extreme condition was resulted from the formation of a robust and stable solid electrolyte interphase (SEI), in which the LiF and Li₃N components could play a synergistic role in the improvement of SEI layer performance. Such a fluoropyridine molecule with good compatibility in the LMBs is expected to be a promising electrolyte additive for the next generation of LMBs.

ACKNOWLEDGMENTS

First of all, I would like to express my sincere gratitude to my supervisor Professor Dr. Abuliti Abudula and Professor Dr. Guoqing Guan for providing me an opportunity to join their team and giving access to the laboratory and research facilities, for their patience, motivation, and immense knowledge. Without their precious supports it would not be possible to conduct the Ph.D. study and related research. Prof. Guan guidance helped me in all the time of research and writing of papers.

Further, I would like to thank Associate Professor Dr. Akihiro Yoshida, Laboratory of Energy Conversion Engineering, Institute of Regional Innovation (IRI), Hirosaki University, for his thoughtful comments and recommendations on my Ph.D. research.

I would also like to acknowledge Professor Dr. Xiaogang Hao, Department of Chemical Engineering, Taiyuan University of Technology, China, for his helps respect to the chemical analysis and materials characterization.

My sincere thank also goes to the co-authors for their collaborative effort during data collection, and all members in our group for their helps and supports to my research.

I cannot forget to thank my family and Professor Dr. Baoxian Ye, Department of Chemistry, Zhengzhou University, China, for their unconditional support and persistent encouragement.

To conclude, I would like to acknowledge the ZiQoo Chemical Co. Ltd. Z. and scholarship from the China Scholarship Council for full supports along my Ph.D. study.

Thank you all.

ZHENGKUN XIE

TABLE OF CONTENTS

ABSTRACT.....	I
ACKNOWLEDGMENTS	IV
TABLE OF CONTENTS.....	V
LIST OF TABLES.....	VIII
LIST OF FIGURES	IX
Chapter 1 Introduction.....	1
1.1 General Introduction.....	1
1.2 Main strategies for advanced LMBs	4
1.2.1 Current collector designs	4
1.2.2 Artificial interface layer	8
1.2.3 Solid-state electrolyte.....	11
1.2.4 High-concentration liquid electrolyte	12
1.2.5 Dual-salt electrolyte	14
1.2.6 Electrolyte additive	15
1.2.7 Salt-solvent combination	16
1.3 Objective of this research	18
1.4 Scope of dissertation	19
References	20
Chapter 2 Experimental	31
2.1 Chemical reagents	31
2.2 Characterization.....	32
2.2.1 Scanning Electron Microscopy (SEM) and Energy Dispersive X-Ray Spectrometer (EDS)	32
2.2.2 Atomic force microscopy (AFM).....	32
2.2.3 X-Ray Diffraction (XRD)	32
2.2.4 Differential Scanning Calorimetry (DSC)	32

2.2.5 Thermogravimetric (TG)	32
2.2.6 X-ray photoelectron spectroscopy (XPS)	32
2.2.7 Contact angle analysis.....	33
2.3 Electrochemical Measurement	33
Chapter 3 Bifunctional ionic liquid and conducting ceramic co-assisted quasi-solid-state polymer electrolyte for lithium metal batteries.....	34
1. Introduction	34
3.2 Experimental	36
3.2.1 Preparation of ionic liquid and electrolyte membrane.....	36
3.2.2 Characterizations and electrochemical measurement	38
3.2.3 Cell assembly and test.....	39
3.2.4 Computational details	40
3.3 Results and discussion.....	40
3.3.1 Physicochemical properties of the prepared SPE membranes.....	40
3.3.2 Electrochemical stability window and ionic conductivity	45
3.3.3 Li ⁺ ion transference number.....	48
3.3.4 DFT theoretical calculations	49
3.3.5 Rate performance and cycle stability	50
3.4 Conclusions.....	57
References	58
Chapter 4 A sandwich-type composite solid-state electrolyte for lithium metal batteries with high areal capacity and cycling stability.....	66
4.1 Introduction	66
4.2 Experimental	69
4.2.1 Preparation of electrolyte membrane.....	69
4.2.2 Characterizations and electrochemical measurement	70
4.2.3 Cell assembly.....	71
4.3 Results and discussion.....	71

4.3.1 Physicochemical properties of the sandwich-type CPE membrane.....	72
4.3.2 Electrochemical stability window and ionic conductivity	77
4.3.3 Lithium ion transference number.....	82
4.3.4 Rate performance and cycle stability of LMBs	84
4.4 Conclusions	95
References	96
Chapter 5 Novel electrolyte additive assisted commercial electrolyte for long cycle life lithium metal batteries	104
5.1 Introduction	104
5.2 Experimental	106
5.2.1 Cell assembly and measurement.....	106
5.2.2 Cell characterizations and analysis	107
5.2.3 Computational details	108
5.3 Results and discussion.....	108
5.3.1 DFT calculations and wettability analysis	108
5.3.2 Electrochemical stability of the electrolyte.....	112
5.3.3 Performance of LMBs.....	119
5.4 Conclusions	131
References	132
Chapter 6 Conclusions and Prospect	139
6.1 Conclusions	139
6.2 Prospect	141
References	144
List of publications and presentations	145

LIST OF TABLES

Table 2.1 Chemical reagents used in this study.....	31
Table 3.1 Comparison of PEO-based polymer electrolytes for Li metal cells.	54
Table 4.1 Technological Parameters of LiFePO_4 sandwich-type CPE Li-metal ASSLBs.....	87
Table 4.2 Comparison of PVDF-HFP-based electrolyte for Li metal batteries.	95
Table 5.1 Comparison of various electrolyte additives for LMBs with different areal capacities.	131

LIST OF FIGURES

Fig. 1.1 The evolution of power and energy densities for various battery chemistries.	2
Fig. 1.2 The development and revival of Lithium metal anodes.	2
Fig. 1.3 Detriments of dendrites in Li metal anodes.	4
Fig. 3.1 Photographs of the prepared (A, C) PEO ₈ -LiTFSI-15%TBPHP and (B, D) PEO ₈ -LiTFSI-TBPHP-12.5%LLZTO SPE membranes at flat and bended states; The typical surface morphologies of (E) PEO ₈ -LiTFSI, (F) PEO ₈ -LiTFSI-15%TBPHP and (G) PEO ₈ -LiTFSI-TBPHP-12.5%LLZTO; (H) cross-sectional SEM image of PEO ₈ -LiTFSI-TBPHP-12.5%LLZTO.	41
Fig. 3.2 XRD patterns of the pure PEO, SPE samples, and LLZTO ceramic powder. The XRD pattern of cubic garnet Li ₅ La ₃ Nb ₂ O ₁₂ (JCPDS: 45-0109) is used as the reference.	42
Fig. 3.3 (A) DSC and (B) TGA curves of the prepared SPEs.	43
Fig. 3.4. Linear sweep voltammetry (LSV) curves of the prepared SPEs with the electrochemical stability window in the range of 2.0-6.2 V.	45
Fig. 3.5 Ionic conductivities of SPEs vs. temperature in the range of 25-80 °C.	46
Fig. 3.6 Ionic conductivities of the PEO ₈ -LiTFSI based composite electrolytes as a function of the weight percentages of (A) IL TBPHP and (B) TBPHP and ceramics filler LLZTO at different temperatures.	47
Fig. 3.7 Lithium-ion transference numbers of the prepared SPEs.	48
Fig. 3.8 A proposed ionic transport behavior in the PEO ₈ -LiTFSI-TBPHP-12.5% LLZTO SPE complex structure.	50
Fig. 3.9 Typical charge-discharge voltage profiles of LiFePO ₄ Li cells based on (A) PEO ₈ -LiTFSI-15wt% TBPHP and (B) PEO ₈ -LiTFSI-TBPHP-12.5% LLZTO SPEs at 50 °C with various rates; (C) Rate performance of the quasi-solid-state LiFePO ₄ Li cells with the PEO ₈ -LiTFSI-15 wt% TBPHP and PEO ₈ -LiTFSI-TBPHP-12.5% LLZTO SPEs at 50 °C; (D) Cycling stability of the LiFePO ₄ Li cells with different SPEs at 0.2 C and 50 °C.	52
Fig. 3.10 (A) AC impedance changes of the quasi-solid state LiFePO ₄ PEO ₈ -LiTFSI-TBPHP-12.5% LLZTO Li coin cell after different cycles at 0.2 C and 50 °C; (B) SEM image of surface morphology for this SPE membrane after 100 cycles test.	54
Fig. 3.11 SEM images of (A) the pristine Li metal electrode; and the Li anode surfaces obtained from the LiFePO ₄ Li cell with (B) PEO ₈ -LiTFSI-TBPHP-12.5 % LLZTO, (C) PEO ₈ -LiTFSI, and	

(D) routine LiTFSI/(DOL+DME, 1: 1 in volume) after cycles at 0.2 C.....	55
Fig. 3.12 Galvanostatic cycling curves of the Li PEO ₈ -LiTFSI-TBPHP-12.5% LLZTO Li symmetrical cells at different current densities at 50 °C. Insets show the enlarge view of cycling curves.	56
Fig. 3.13 Quasi-solid-state LiFePO ₄ PEO ₈ -LiTFSI-TBPHP-12.5%LLZTO Li metal pouch cell assembled to light the LED at (A) flat states, and well-running under (B) folding and (C) a corner cutting at room temperature.	57
Fig. 4.1 Photographs of the prepared PEO ₈ -LiTFSI/PVDF-HFP-15%LLZTO/PEO ₈ -LiTFSI sandwich-type CPE film at (A) flat and (B) bend states; The typical surface morphologies of (C) LLZTO powders and (D) sandwich-type CPE film; Cross-sectional (E) SEM image and (F) EDX mapping of sandwich-type CPE film where green, blue and red dots indicate the location of La, Zr, and Ta elements, respectively.	72
Fig. 4.2. AFM images of (A, B) PVDF-HFP-15% LLZTO CPE membrane and (C, D) sandwich-type CPE membrane.	73
Fig. 4.3 XRD patterns of pure PVDF-HFP, CPE samples, LLZTO ceramic powder and the diffraction pattern of cubic garnet Li ₅ La ₃ Nb ₂ O ₁₂ (space group: <i>Ia-3d</i> (230), JCPDS: 45-0109) as the reference.	74
Fig. 4.4 TGA curves of the CPEs.	75
Fig. 4.5 DSC test results of the prepared electrolyte membranes.	76
Fig. 4.6 Linear sweep voltammetry (LSV) curves of the prepared CPEs in the range of 2.0-6.5 V at 40 °C with a scan rate of 1 mV s ⁻¹ . Inset shows the enlarge view of LSV curves.	77
Fig. 4.7 Ionic conductivities of CPEs vs. temperature in the range of 23-100 °C.....	78
Fig. 4.8 Impedance spectra of (A) the PEO ₈ -LiTFSI/PVDF-HFP-LLZTO (PPL) two-layer CPE membrane as a function of the weight percentage of ceramics filler LLZTO at 40 °C and (B) the sandwich-type CPE membranes working at a temperature ranged from 23 to 100 °C; (C) The compared EIS spectra of PVDF-HFP-15%LLZTO CPE and the sandwich-type CPE membranes at ambient temperature. The inset shows the equivalent circuit.	79
Fig. 4.9 TGA curve of the sandwich-type CPE.	80
Fig. 4.10 (A) Impedance spectra and (B) ionic conductivities of the sandwich-type CPE membrane with liquid electrolyte vapor from 30 to 100 °C.	81
Fig. 4.11 DC polarization curve for Li sandwich-type CPE Li cell under a polarization voltage of 10 mV. The insets show the equivalent circuit and EIS before and after the polarization,	

respectively. 82

Fig. 4.12 (A) Initial charge-discharge profiles at different rates and (B) rate performance of the LiFePO_4 | sandwich-type CPE |Li-metal battery; (C) cycling stability of all-solid-state LiFePO_4 |Li cells with the sandwich-type CPE at 0.2 C and 40 °C. 84

Fig. 4.13 (A) Cross-sectional SEM image of the obtained thin sandwich-type CPE membrane (50 μm); (B) The typical surface morphology; (C) Cross-sectional SEM image of the obtained thin Li metal with Cu current collector; (D) is the enlarged image of (C); (E, F) EDX mapping and analysis of the obtained thin Li metal with Cu current collector where yellow line indicates the Cu elements. 87

Fig. 4.14 (A) AC impedance changes of the all-solid-state LiFePO_4 |sandwich-type CPE|Li-metal cell after different cycles at 0.2 C and 40 °C, the inset is the equivalent circuit; (B) SEM image of surface morphology for the sandwich-type CPE membrane against Li metal after 300 cycles test. 88

Fig. 4.15 Galvanostatic cycling curves of the (A) Li| sandwich-type CPE |Li and (B) the Li| 1M LiPF_6 in EC: DEC |Li symmetrical cells at different current densities. 89

Fig. 4.16 SEM images of surface morphologies for the Li anodes obtained from the LiFePO_4 |Li cell with (A) PEO_8 -LiTFSI/PVDF-HFP-15%LLZTO/ PEO_8 -LiTFSI sandwich-type CPE and (B) 1 M LiPF_6 / (EC: DEC, 1: 1 in volume) after 100 cycles at 0.2 C. 90

Fig. 4.17 Typical charge-discharge curves and cycling stability of all-solid-state (A, B) LiCoO_2 |Li-metal and (C, D) $\text{LiNi}_{1/3}\text{Mn}_{1/3}\text{Co}_{1/3}\text{O}_2$ |Li-metal cells with the sandwich-type CPE at 0.1 C and 40 °C. 92

Fig. 4.18 The all-solid-state pouch LiFePO_4 |Li metal cell assembled with sandwich-type CPE to light the LED at (A) flat state, (B) bending, and (C) folding states at room temperature. 93

Fig. 4.19 A schematic diagram of (a) the garnet LLZTO electrolyte with massive Li dendrites growth, (b) structure of the sandwich-type CPE with a flat Li anode surface and (c) the contact behavior of sandwich-type CPE with Li metal. 93

Fig. 5.1 (A) The molecular orbitals and energies for the HOMO and LUMO of the 2-FP and other solvents; (B) Schematic of solvation effect between Li^+ and solvents. The grey, white, red, blue, green, and purple spheres represent atoms of carbon, hydrogen, oxygen, nitrogen, fluorine, and lithium, respectively; (C) Summary of the binding energy between solvents and lithium ions in different electrolyte solutions and vacuum. 109

Fig. 5.2 The length changes of C-F bonds during the reduction of 2-FP molecule via the DFT theoretical calculations, where green and blue dots represent the locations of F and N atoms,

respectively.	111
Fig. 5.3 Contact angles of the LiPF_6 electrolyte (A) and LiPF_6 with 2% of 2-FP electrolyte additive (B) drops on the Celgard 2400 PP separator.	112
Fig. 5.4 (A) Illustration of Li nucleation and deposition on the Cu foil electrode with and without electrolyte additive; (B) Voltage profiles of Li Cu cells with the LiPF_6 electrolytes in the absence and presence of 2% of 2-FP electrolyte additive. Insets show two enlarged views of voltage profiles.	113
Fig. 5.5 (A) Coulombic efficiencies of Li Cu cells with the LiPF_6 electrolytes in the absence and presence of 2% of 2-FP electrolyte additive at a current density of 0.5 mA cm^{-2} and (B) EIS of Li Cu cells after two different cycles. Inset shows the enlarged view of EIS spectra.	114
Fig. 5.6 SEM images of the deposited Li on the Cu substrate in Li Cu cells: cross-section views and top views using LiPF_6 electrolyte without (A, B) and with (C, D) 2% of 2-FP electrolyte additive after the 50-cycle test. Scale bar: $10 \mu\text{m}$	116
Fig. 5.7 Cycling performances of the Li Li symmetrical cells with LiPF_6 electrolyte in the absence and presence of 2% of 2-FP electrolyte additive at a current density of 1 mA cm^{-2}	117
Fig. 5.8 (A) Cycling performance of LiFePO_4 Li metal batteries using the carbonate-based LiPF_6 electrolyte ($60 \mu\text{L}$) at 1 C and 30°C ; (B) Cycling performances of NMC111 Li metal batteries using the LiPF_6 electrolytes without and with 2% of 2-FP electrolyte additive under 30°C	119
Fig. 5.9 Voltage curves as a function of cycle number of NMC111 Li batteries using (A) LiPF_6 electrolyte, (B) LiPF_6 with 2% of 2-FP electrolyte additive at 0.5 C and 30°C	120
Fig. 5.10 Cycling performance of LiFePO_4 Li metal batteries using the LiTFSI electrolytes without and with 2% of 2-FP electrolyte additive at 1.5 mA cm^{-2} and 30°C	121
Fig. 5. 11 SEM images of the Li anode surfaces before (A) and after cycling test of LiFePO_4 Li metal batteries with LiTFSI electrolyte in the absence (B) and presence (C, D) of 2% of 2-FP electrolyte additive.....	123
Fig. 5.12 XPS spectra of F 1s and N 1s for Li metal retrieved from LiFePO_4 Li metal batteries with the LiTFSI electrolyte in the absence (A, C) and presence (B, D) of 2% of 2-FP electrolyte additive.	124
Fig. 5.13 Cyclic voltammogram curves of Li Graphite cells in (A) LiPF_6 electrolyte, (B) LiPF_6 electrolyte with 2% of 2-FP electrolyte additive at a scan rate of 0.1 mV s^{-1} . Insets show the enlarge views of CV curves.	126
Fig. 5.14 Cycling performances of NMC111 Li metal batteries using the LiPF_6 electrolytes without	

and with 2% of Pyridine electrolyte additive under 30 °C.	127
Fig. 5.15 SEM images of the NMC111(A-C) and LiFePO ₄ (D-F) cathode surfaces before (A, D) and after cycling tests in the absence (B, E) and presence (C, F) of 2% 2-FP electrolyte additive. Scale bar: 50 μm.	128
Fig. 5.16 A proposed evolution of SEI layer compositions with the electrolytes in the absence and presence of the 2-FP electrolyte additive.	130

Chapter 1 Introduction

1.1 General Introduction

Rechargeable lithium-ion batteries (LIBs), first commercialized in 1990 by Sony Corp, are widely used in the mobile phones, electric vehicles and smart grids. In the commercial LIBs, the graphite matrix with a theoretical capacity as low as 372 mAh g^{-1} is the dominant choice for the anode manufacturing in order to achieve the safety requirement [1]. To improve the energy storage capacity, lithium (Li) metal is regarded as the ideal anode since it is a very light metal (0.534 g cm^{-3}) with an ultrahigh specific capacity (3862 mAh g^{-1}) and also has the most negative standard electrochemical potential (-3.040 V vs. the standard hydrogen electrode) among the possible anode materials, moreover, the batteries using a Li metal anode could deliver a higher operating voltage (around 0.1 V) than the current commercial graphite anode, which ensuring a further increase in energy density [2]. As proved in **Fig. 1.1** and **1.2**, benefiting from the abandonment of Li^+ ion host materials, the Lithium metal batteries (LMBs) could accomplish a remarkably high energy density at the designs level. This is consistent with the previous reports that replacing the graphite anode with a lithium metal anode has increased the specific energy (Wh kg^{-1}) and energy density (Wh L^{-1}) of batteries by approximately 35% and 50%, respectively [3]. More importantly, the use of a Li metal anode will save the cost associated with graphite anode production, avoid the use of expensive N-Methyl-2-Pyrrolidone (NMP) solvent and simplifying the preparation procedure produce by slurry coating followed with drying [4]. As above outlined, the Li metal could be regarded as a “Holy Grail” anode in high-energy density battery designs.

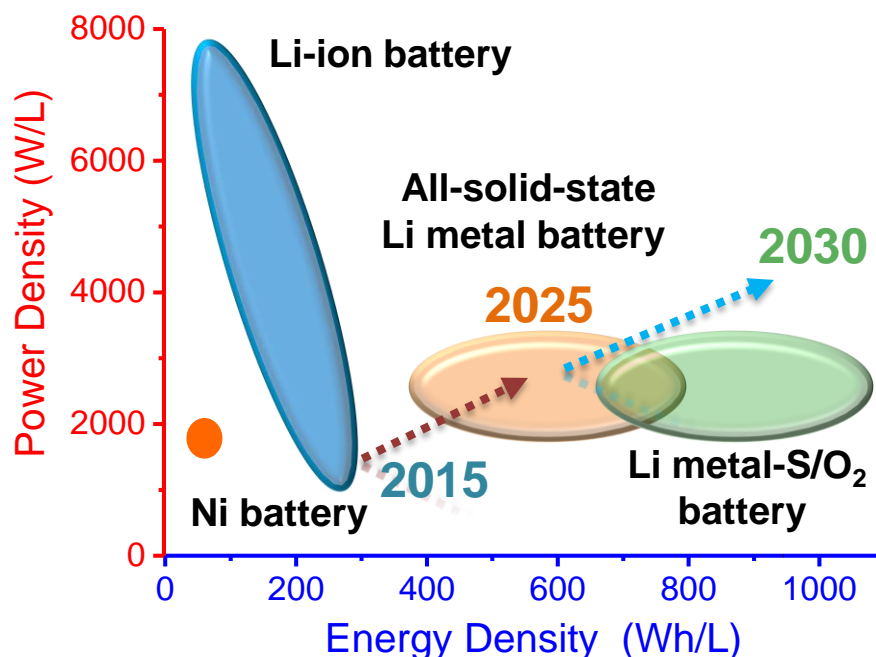


Fig. 1.1 The evolution of power and energy densities for various battery chemistries.



Fig. 1.2 The development and revival of Lithium metal anodes.

However, as displayed in **Fig. 1.3**, the growth of Li dendrites, limited Coulombic efficiency and severe parasitic reactions with the components in the routine liquid electrolytes always occur in the batteries during Li deposition/stripping since the active Li metal could react with nearly all

dipolar aprotic organic solvents [5]. Thus, the widespread deployment of high-energy density Lithium metal batteries (LMBs) is severely hindered. To date, the anode with a large excess amount of Li metal was always employed in most of researches so that the real specific capacity is not so high [6]. For example, by overusing of 200% Li metal, the volume energy density of LMBs decreased from a theoretical capacity of 2060 to 687 mAh L⁻¹, which is even lower than that of graphite anode (719 mAh L⁻¹) [7]. Moreover, the Li metal with the excess thickness (Li metal anode thickness > 30 μm) could either cause the failure operation of LMBs at an early stage by rapid depleting the lean electrolyte or act as a lithium reservoir with flooded electrolyte to create an illusion of prolonged the cycle life of LMBs [8]. More seriously, the large excess of lithium metal anode in LMBs could lead to vigorous burning and explosion in the case of electric vehicle accidents and some extreme conditions. Thus, decreasing the Li metal amount by using an ultrathin Li metal anode (e.g., < 30 μm, ideally 20 μm or less) could achieve a higher energy density with higher safety in the practical applications [3]. However, although Li foil market allows for easy trading with the modest price of US\$300–400 kg⁻¹, the price for processing it to ultra-thin one (limited excess Li metal anode) could even exceed US\$1,000 kg⁻¹ since the highly reactive Li metal with strong adhesion property always requires more complex manufacturing techniques and strict operating conditions, such as evaporation, deposition, multiple rolling, punching, and dry atmosphere so that its cost is significantly higher than the current graphite-based anode (ca. US\$20 kg⁻¹) [9-11]. Furthermore, due to the rapid growth in the demand for lithium batteries and limited global lithium reserves, the price of Li (based on Li₂CO₃, data from *metalary.com*) has increased about fourfold in the past decade. Meanwhile, extracting lithium from the lithium-rich salt lakes or seawater yet another critical bottleneck affecting the inexpensive shaping technologies for the Li metal anode. All in all, if the costs of thin Li foil and its processing decrease significantly, the LMBs still have a bright future.

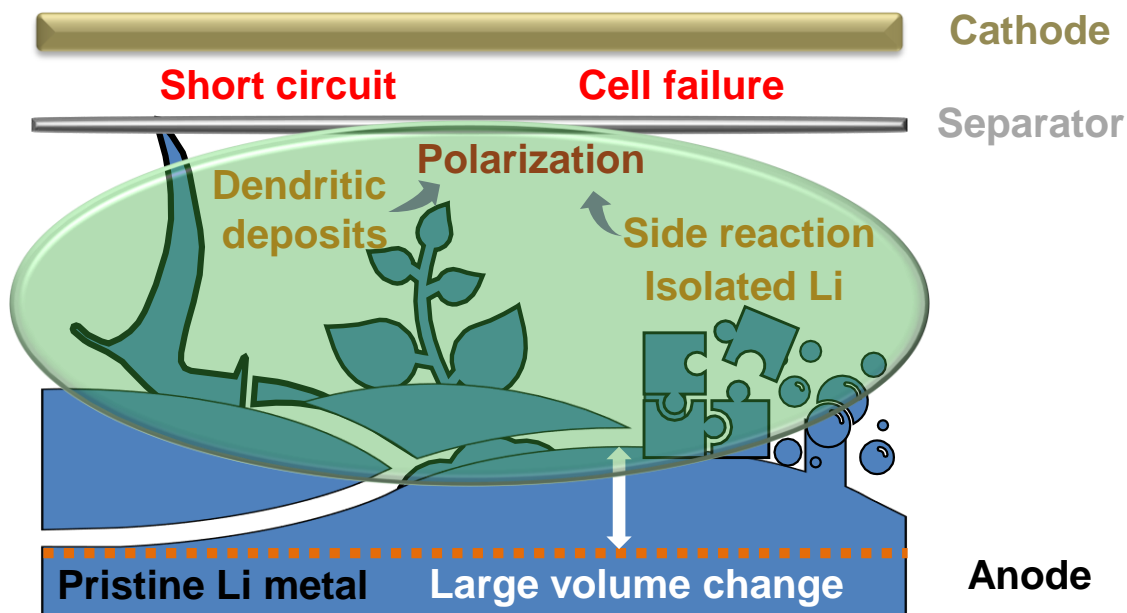


Fig. 1.3 Detriments of dendrites in Li metal anodes.

Herein, the progress and prospects in the development of LMBs are critically reviewed. The main strategies with significant contributions in the history of the research and development (R&D) of the LMBs, including the applications of current collector engineering, artificial interface, and electrolyte formulations, are summarized. They are discussed in the following sections and the challenges in the R&Ds of advanced LMBs are outlined.

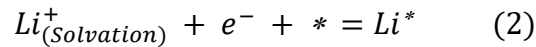
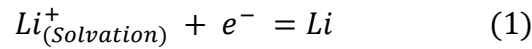
1.2 Main strategies for advanced LMBs

1.2.1 Current collector designs

It is known that during the first charge in the LMBs system, the Li ions stored in the cathode are nucleated as metallic lithium and deposited on the anode, which is significantly different from the intercalation reaction between lithium ions and graphite anode to form Li-graphite intercalation compound [10]. As for the anode current collector, it is found that the high density (8.96 g cm^{-3}) of the Cu foil is in fact not suitable for the LMBs with high energy density although it renders a

good compatibility with graphite-based anodes of commercial LIBs [12]. In addition, as reported, the Cu foil current collector usually has high interface energy with Li, which can cause the rising of deposition overpotential and affect the morphology of deposited Li and the subsequent solid electrolyte interphase (SEI) formation, even leading to dendrite formation [13-14]. Therefore, it is important to select the materials for the current collector substrate of anode to enable the practical application of LMBs.

Considering the corrosion stability, chemical reactivity, electronic conductivity, abundance, and cost, as demonstrated by Pande *et al.* [15], most of the transition metals-based (i.e. Fe, Ti, Mn, V, Cr) and the fully lithiated alloy-based current collector (i.e. Li-Zn, Li-Mg, Li-Ca, Li-B, Li-Al, Li-Ga, Li-Si, Li-Sn, Li-Cd, Li-Ag) remain the ability to further improve the specific energy of LMBs by replacing the Cu current collector. Moreover, regardless of the energy density, with the aid of density functional theory (DFT) calculations, the effects of candidate substrate surface on the initial Li nucleation overpotential and growth behavior have been elucidated based on their relationships with the adsorption free energy and the surface diffusion energy, respectively [16]. It is confirmed that the lower nucleation overpotential and the weaker surface diffusion barrier enable the two-dimensional growth of deposited Li on the surface of the current collector [17]. Herein, the related energy level and limiting potential (U) can be calculated based on the following equations [15, 18]:



$$U = - \frac{(\Delta G_{Li^{*}} - \Delta G_{Li})}{e} \quad (3)$$

Where $\text{Li}^+_{(\text{solvation})}$ represents the solvated Li^+ ion, * represents the adsorption site on the substrate surface. However, it should be noted that the nucleation overpotential order of above candidate substrates did not show the pronounced improvement of Li nucleation behavior when compared to the Cu substrate [15]. Beyond these considerations, as discussed by Jung *et al.*, the growth behavior of plating Li on a target substrate also be controlled by surface energy ($\gamma_{\text{substrate}}$, γ_{crystal}), interfacial energy (γ_i), and two-phase contact angle (θ), the island growth or film growth model could be identified by the Young equation. When the growth follows the island growth mode, large voids could be inevitably formed between the Li islands, resulting in the formation of highly reactive surfaces, which finally generate the dendritic Li, leading to a low CE and cycle life lost in LMBs [19]. Thus, it is important to screen the current collector substrates which can modulate Li deposition behavior by using DFT calculations is important for the R&Ds of LMBs at the first step.

The Miller indices of the planes in a cubic metal crystal structure is another key factor that influences lithium plating [20]. For instance, the (111) facet of face-centered cubic (FCC) metal Cu displays the lower nucleation overpotential as well as weaker Li diffusion energy barrier when compared to its (100) and (110) facets, which should more suitable for the full Li coverage on it. Moreover, the calculated surface energy 1.40 J m^{-2} of Cu (111) is also lower than other two Miller indices in Cu, i.e., 1.93 J m^{-2} of (110) and 2.01 J m^{-2} of (100) facet, which is also benefited to the formation of a homogeneous film-growth layer of Li metal. As such, increasing the fraction of the (111) facet on the Cu substrate surface could induce a uniform and dendrites-free Li deposition [15]. Such a phenomenon can be also found on the (110) facet of body-centered cubic (bcc) crystals of Fe and Cr, and the $(11\bar{2}0)$ facet of the hexagonal close-packed (hcp) crystal such as Zr and Ti. Meanwhile, Meanwhile, Gu *et al.* demonstrated that the lithiophilic Cu(100) surface induced by electrochemical faceting enables a more uniform Li deposition and stable cycling stability than the pristine Cu(111) surface among the different types of Cu current collectors, including Cu foil, Cu

mesh and Cu foam [21], these results are consistent with their DFT calculation results between Li(110) facet and the low Miller index surface of Cu. However, these conclusions differ from those reported by Pande and co-workers in that after electrochemical faceting, the roughness of Cu decreases from 174 nm to 27 nm, which reduces the local current density and ensures a more uniform Li distribution. On the other hand, due to the low Li coverage during the initial Li deposition process, the Cu(100) facet does have a lower nucleation overpotential than that Cu(111) facet, which may affect the crystallographic orientation of subsequent bulk deposition [22].

In contrast to transition-metal current collectors, most miller indices surface of the Li-alloy compounds displayed almost no nucleation overpotentials. In addition, when considering the diffusion energy barrier, it's also confirmed that all Li alloys have average activation energies as low as 0.05 eV, which will help in redistribution of the uneven plated Li over time. Overall, the use of alloy-types of current collectors, including Li-Zn, Li-B, Li-Al, Li-Si, Li-Sn, Li-Cd, Li-Ag, and so on, should be better than the current applied Cu foil for LMBs [15]. To date, some of alloy-based current collectors have been experimentally tested in an dendrites-free anode [23]. By improving the surface uniformity and decreasing the nucleation overpotential, the dendrites-free Li can be effectively formed on the alloy-based current collectors, which indeed improve the cycle life and safety of LMBs with high specific energy density. However, the cost for the fabrication of alloy-based current collectors is high since some special methods such as magnetic sputtering technology are necessary [24]. Moreover, after repeated alloying-dealloying in long-term cycles, the alloy layer may crack and form a new alloy layer with Li, which will further consume the limited amount of lithium and lean electrolyte, leading to the reduction in the Coulombic efficiency (CE) as well as capacity retention of LMBs. Therefore, these factors need to take into consideration in designing an alloy current collector substrate.

Besides, fabrication of special micro- and/or nano-structures of the current collector has also

been proven to enable uniform Li deposition and prolong the cycle life of LMBs. For instance, the current collector with a 3D porous structure could contribute to the increase of available nucleation surface area, the decrease of localized current density, and redistribution of the Li^+ flux, leading to uniform deposition with dendrite growth. As proved, Umh *et al.* fabricated the dendritic Cu superstructure using a facile dynamic H_2 -bubble template method, which constrained the dendrite growth as well as the formation of bulk Li in the network structure of the current collector [25]. When considering these special structures, how to decrease the construction cost and how to achieve the desired morphology and porosity should be the key issues [26]. Notably, a cleaning step for most current collectors is required in order to remove the passivation layer consisting of metal oxides since they may react with active Li to form a variety of lithiated compounds [27]. In a conclusion, besides the optimizations of Miller index surface and alloy design, the current collector with a 3D porous structure could overcome the anode volume expansion, uneven deposition and channel clogging.

1.2.2 Artificial interface layer

While these state-of-the-art current collector designs can enhance cycle life and energy-density of AFLBs, designing an artificial interface layer on the anode could not only induce a uniform Li deposition, lower the localized current density caused by the heterogeneous and rough surface of the current collector like Cu foil, but also enhance the adhesion of Li plating to substrates and generate a more robust SEI layer to effectively suppress the parasitic reactions between deposited Li and electrolyte [28-29]. A scalable approach has been applied for the precise interface regulating of Cu substrate to prolong the cycle life of LMBs. Artificial interface layer can be prepared by the spin coating technology, physical/chemical vapor deposition, and self-assembly on the substrate, or by formation of the coordinate bond directly on the substrate [30-31]. For instance, Hwang's group fabricated a nanosized polyethylene oxide (PEO) film as artificial interface layer via spin

coating method [28]. Due to the strong interaction between the ether oxygen groups of PEO polymer chains and the Li^+ ions, the PEO layer not only enabled a well-distributed Li^+ ion flux but also shielded the direct contact between metallic Li and the highly reactive electrolyte. As a result, the synergistic effect between the homogeneous Li^+ flux and the encapsulation of plated Li by the PEO induced the dendrites-free Li deposition as well as the formation of a thin SEI layer with high-quality. However, it should be noted that the huge volume fluctuation of the plated Li could exceed PEO layer flexibility, which can limit the cycle life of the LMBs. To solve this issue, Abbrha *et al.* designed a novel alternative interface layer comprising of ceramic electrolyte $\text{Li}_7\text{La}_{2.75}\text{Ca}_{0.25}\text{Zr}_{1.75}\text{Nb}_{0.25}\text{O}_{12}$, polyvinylidene fluoride (PVDF) and LiClO_4 salt by electrospinning method. With a ceramic electrolyte content up to 84%, this composite electrolyte coating layer (2 μm) not only effectively improved the mechanical stability, suppressed the formation of Li dendrites, but also induced a LiCl-rich SEI formation [32]. Further, Hwang's group maintained the high mechanical stability of the interface layer by growing ultrathin multilayer-graphene (MLG) over Cu via chemical vapor deposition (CVD) method [33]. Such a lightweight MLG coating layer has many advantages such as improving the Li adhesion on the substrate, enhancing the wettability of the electrode interface and achieving uniform Li-ion flux during cycling by π -electron delocalization [34-35]. Moreover, such a graphene layer has high mechanical strength (1 TPa versus 4.9 GPa of Li) and ultimate tensile strength, which enables the prevention of Li dendrite penetration and mitigates the large volume expansion during the Li plating/stripping process [36]. Wondimkun *et al.* also improved the cycling stability of LMBs by using a binder-free ultra-thin spin-coated GO as an artificial layer [37]. Meanwhile, Tu *et al.* also used an atomic-layer-deposited Al_2O_3 to effectively stabilize the electrode interface, in detail, the anchored compact Li on the current collector by the pinhole-free Al_2O_3 coating layer (15 nm) contributed to the enhanced Li deposition stability, and limited the formation of electronically disconnected or isolated Li [38].

To mitigate the volume changes of anode during cycling, Liu *et al.* prepared a viable 3D composite host layer, which not only decreased the local current density by providing an electronic conductive network, but also reduced the void formation during the Li plating [39]. Besides these physical coating layers, Kang *et al.* used the benzotriazole (BTA) molecule with lithiophilic function groups of the N atom to modify the Cu foil surface, which made the metallic Li deposition uniformly [40]. As a result, only by immersing Cu foil in the BTA solution for 5 minutes, the cell can cycling maintain a stable cycling by the BTA-Cu coordination bond. In addition, Li *et al.* found that a thin-layer Cu_3N coating enabled the uniform Li ion flux, and effectively suppressed the parasitic reactions as well as dendrite Li growth on the Cu substrate [41]. Herein, the negligible CE decay of cell was resulted from the *in-situ* formation of robust $\text{Li}_3\text{N}/\text{Cu}$ current collector via the Cu_3N conversion. Moreover, it has been widely proved that Li_3N played a crucially important role in the property of the robust and stable SEI layer [42].

Although remarkable breakthrough in dendrite suppression have been demonstrated by depositing the ceramic-based artificial interface layer with high Young's modulus, the economic viability and nano-particle emissions originated from the physical/chemical vapor deposition technology remain as the major issues [43]. In contrast, the preparation of artificial interface layer by spin-coating of polymer has some advantages such as economically viable, ease of preparation, and light weight. More importantly, it is compatible with the current applying manufacturing infrastructure for the graphite-based anode. Meanwhile, other alternative approaches such as Langmuir-Blodgett (LB) film technology, electrochemical deposition and molecular beam epitaxy growth can also be adopted to improve the quality of interface layer [44]. In addition, it is proved that pursuing extremely high mechanical strength of interface layer is meaningless [45]. Instead, improving the structural uniformity of interface layer should be more important for enhancing the stability of SEI since it can regulate the Li^+ ion flux and reduce the roughness of the Cu foil (e.g.,

bare Cu: 26.5 nm; Cu@GO: 13.4 nm) [37]. Furthermore, the coating thickness of artificial interface layer should be another key factor to affect the performance of LMBs since the interfacial impedance has a strong relationship with the layer thickness. An ultra-thin artificial interface layer with uniform thickness could not only weaken the internal resistance of the battery, but also provide more space for the cathode, improving the volumetric energy density of the LMBs. In addition, it should be noted that the interface layer could also avoid the lithiation/de-lithiation and alloying reactions to result in the large volume expansion and cracks in the SEI layer during the cycling process.

Altogether, these studies and insights have provided new opportunities for current collector engineering design that can be extended to LMBs with various electrolyte formations. It's worth noting that the electrolyte engineering plays a more important role than current collector itself since the cell performance is principally determined by SEI components, and to make LMBs viable, the advanced electrolyte formulations should be developed in parallel with the novel design for current collector engineering.

1.2.3 Solid-state electrolyte

The electrolyte formulation engineering can be considered as the center of LMBs [5]. The cell performance is principally determined by SEI components, and it is usually induced by the electrolyte properties. In general, the suitable electrolyte formulation could reduce the parasitic reactions with the continuous consumption of active Li and the electrolyte, suppress the growth of Li dendrites, and finally extend the cycle life of the LMBs [3]. As the “Holy Grail” electrode, Li metal has been plagued by continuous parasitic reactions with liquid electrolyte components. Based on the concept to reduce the side reactions and high shear modulus, it is believed that substituting the flammable liquid electrolyte with the solid-state electrolyte could maintain the dendrite-free Li deposition, which is necessary for solving the cycling stability and safety issues

[46]. Hence, solid-state electrolytes, including inorganic-, polymer- and organic/inorganic hybrids-based electrolytes are considered as the most promising for the practical application of LMBs in the near future [47-50]. Despite the rapid development in the last decade, the low ionic conductivity and high interfacial resistance remain a bottleneck in manufacturing of LMBs with solid-state electrolytes [51-52]. Moreover, the oxide-based inorganic solid electrolytes are always fabricated using a complicated synthesis process at high temperatures, which may increase the cost of LMBs, for sulfide-based inorganic solid electrolytes, toxic H_2S is easily generated in the presence of moisture and results in some safety problem. In contrast, the polymer/inorganic hybrids-based electrolytes have the advantage of ensuring the adequate ionic conductivity and reducing the electrolyte-electrode interfacial resistance of batteries. Hence, by combining the unique advantages of hybrid electrolytes with high-energy density Li metal anode, the all-solid-state LMBs will be valuable for designing safe as well as high-energy density devices.

1.2.4 High-concentration liquid electrolyte

Simply increasing the salt concentration in the liquid electrolyte has been proved to be an effective way to achieve dendrites-free anode [53-54]. The concentrated electrolyte (e.g., >3 M) could demonstrate unique characteristics, which are remarkably distinct from the conventional dilute electrolyte (e.g., 1 M). Herein, since the fraction of free solvent molecules in the concentrated electrolyte is very low, the salt-solvent combination is prone to shift the location of lowest unoccupied molecular orbital (LUMO) from the solvent towards the salt, which could result in the preferential reduction of Li-salt anions combination, leading to the formation of durable and inorganic components rich SEI or cathode electrolyte interphase (CEI), thereby improving the availability of Li^+ ions [55-56]. A plenty of uncoordinated solvent molecules in routine 1 M electrolyte has been proved by a molecular dynamic (MD) simulation [53, 56]. In addition, it is reported that the inorganic components rich SEI layer with low surface diffusion barrier, suitable

surface energy, and multiple diffusion pathway are benefit for the two-dimensional growth of metallic Li [57-58]. To date, various concentrated electrolytes have been proposed and tested in the LMBs. For examples, as the concentrated 4 M lithium bis(fluorosulfonyl)imide (LiFSI) electrolyte was used in the LMBs, the side reactions between the free solvent and metallic Li was effectively reduced, robust SEI was induced by the anions, and high Li⁺ flux was achieved. As a result, different from the generation of numerous dead Li in the dilute electrolyte, the morphology of the plated Li was shiny and compact, and the LMBs exhibited a satisfactory capacity retention [56]. Consistent with these works, Hwang's group applied 3 M LiFSI in ether-based electrolyte and 2 M LiPF₆ in a carbonate-based electrolyte respectively in the Lithium batteries, and also found that the cycle performance was greatly improved [59, 60]. Herein, the enhanced cycling stability of cells was considered to be originated from the synergistic effects between the slow initial deposition rate and the formation of ROCO₂Li and LiF rich-flexible SEI.

In certain cases, the unique high-voltage stability of the concentrated electrolytes is attributed to the Li salt-anion occupying most of the inner Helmholtz layer in the cathode, which could reduce the residual of easily oxidizable solvent molecules. Also, forming a more uniform CEI could prevent the lattice oxygen exposure [61]. As such, benefits to a smaller fraction of flammable free solvent molecules and lattice oxygen exposure, the risks of high-voltage LMBs can be significantly lowered. As a conclusion, compared to other proposals, by using the concentrated electrolyte should be a facile yet effective strategy, which can meet most of current requirements for high-energy density LMBs without the additional manufacturing processes. Moreover, the economic cost of concentrated Li salt could be reduced with the large-scale application and extensive industrial development in the future.

1.2.5 Dual-salt electrolyte

As stated by Xu *et al.*, the further increasing in salt concentration from 4.6 M to 6.9 M does not provide a significant positive effect on LMBs, which may attribute to increased viscosity, decreased ionic conductivity, and poor ability to wet polymer separators [62]. As a supplement to high-concentration electrolyte, dual Li salt electrolyte was emerged, by which the synergistic effect between the salts and dipolar aprotic organic solvents benefits to the formation of thin protective SEI as well as CEI layers, and thereby improving the CE and lifespan of LMBs [63]. Alvarado *et al.* deeply investigated the morphology of Li deposition and SEI formation mechanism in a 4.6 M LiFSI + 2.3 M lithium bis(trifluoromethanesulfonyl)imide) (LiTFSI)-dimethyl ether (DME) dual-salt electrolyte system, and it is found that a great deal of voids in both routine 1 M LiPF₆ and 4 M LiFSI electrolyte, and the highly reactive surface of porous Li typically led to a low CE and a decreased cycle life for LMBs. In stark contrast, with the dual-salt electrolyte, the plated Li in the (110) crystalline orientation with a densely packed lithium columns morphology appeared. Mechanism analysis indicated that the presence of LiTFSI kinetically hindered the degradation of LiFSI so that it can serve as a more effective F-donator. In particular, these reduced dual-anion fragments can introduce entirely distinct interphases, promoting a robust and inorganic-rich SEI formation. Interestingly, the protective CEI was generated from the LiFSI decomposition on the cathode surface, as opposed to the SEI formation. Meanwhile, the LiTFSI contributed to the high-voltage stabilization by shielding the electrolyte solvent from direct contact with the radical cathode surface [62, 63]. Consistent with Alvarado and co-workers, the effect of 2 M LiFSI-1 M LiTFSI dual-salt electrolyte on the formation of higher mechanical modulus, lower solubilities, faster ion transport inorganic components richer SEI, such as LiF, Li₂O, and Li_xNO_y, was also identified again by Beyene *et al.* [63]. Besides, Rodriguez *et al.* recently further demonstrated that some inorganics such as LiNO₃ was favorable over the above costly LiFSI species since it has a

high level of coordination ability to aggregate the solvate-Li⁺ structure [64]. Despite these improvements, the high cost of such dual-salt electrolytes with high concentrations is still the huge barricade to meet the requirements for commercialization. In order to address this issue, the dual-salt designs with a dilute salt concentration has been explored by Weber *et al.* [65], they also confirmed that the uniform Li deposition in the dual-salt electrolyte was originated from the organic/inorganic fluorine components rich SEI since this robust and low porosity SEI layer could effectively minimize the side reactions between plated Li and the electrolyte.

In a conclusion, through the co-reduction or self-sacrifice effect of the dual/multiple-salts in the electrolyte, more reliable electrode-electrolyte interfaces as well as ion transmission in AFLBs can be realized. In addition, the increase in viscosity of multiple-salts electrolyte may suppress the corrosion of current collectors such as Al, reduce the degradation of cathodes, and improve the safety of electrolytes by decreasing the fraction of free solvent [56, 67]. It is reported that the oxidation onset threshold of the ether-based electrolyte was even pulled above 5 V with this design [82]. Regardless of these pronounced advantages, the cycle life of LMBs with this electrolyte as well as limited excess Li anode is still limited also due to the continuous consumption of electrolyte salts and limited Li during the stripping and plating processes [65]. Some strategies such as tuning the property of salt using a well-designed solvent and decreasing the fractions of unpair ion fragments could be adopted to hinder the consumption of electrolyte salt.

1.2.6 Electrolyte additive

Recently, considering low cost and easy processing, tremendous electrolyte additives have been applied to improve the performance of Li metal anode [68-70]. As the electrolyte additive (normally, below 10% either in weight or in volume), it usually has the ability for inducing the generation of a robust SEI or CEI layer to effectively suppress the parasitic reactions between electrodes and electrolyte [71]. Various electrolyte additives have been applied to improve the

performance of Li metal anode. For instance, carbonate-based additives like fluoroethylene carbonate (FEC) [72], alkali metal salt-based additives like lithium difluoro(oxalate)borate (LiDFOB) [73], ionic liquids like 1-dodecyl-1-methylpyrrolidinium bis(fluorosulfonyl)imide (Pyr1(12)FSI) [74], nitrates-based compounds like $\text{La}(\text{NO}_3)_3$ [75], trace amount of water [20], sulphides and related additives like Li_2S_8 [76], multifunctional additives like tris (2, 2, 2-trifluoroethyl) phosphite [77], and so on. It is well known that the preferential reduction of electrolyte additive is one of the key factors to determine whether it can be used to tailor the properties of the passivation layer on the surface of Li anode [71]. Nevertheless, the energy density of LMBs may decrease when considerable electrolyte additives consumed the limited amount of Li. Thus, the amount of additive in the electrolyte should be controlled. In addition, due to the thermodynamical instability of the fully delithiated cathode, the electrolyte additive should be well-designed to form a robust CEI layer to block the generation of reactive transition metal-oxygen radical species. Meanwhile, the synergetic effect of such electrolyte additives should be further enhanced by other strategies like the current collector engineering as a fore mentioned to reduce the rate of active Li depletion.

1.2.7 Salt-solvent combination

Tuning electrode/electrolyte interphase chemistry via electrolyte engineering was also proved to play a decisive role in prolonging the cycle life of LMBs, of which the dual salt electrolyte design with a low concentration is one of the most economically viable options. This way differs from the above-mentioned ways by selecting of solvents and/or optimization of salt-solvent combinations. The solvent in the conventional electrolyte is a key factor for the cycling reversibility of LMBs since the reactions between Li and the solvents played an important role in LMBs [78]. For example, the feasibility of LMBs with a carbonate-based solvent is severely limited due to the intrinsic instability of carbonates with Li metal [79]. It should be noted that the

electrolyte could be continuously reduced by the Li with high Fermi level even under the driving force of thermodynamics in the rest state [80]. As an evidence, when employing these carbonate-based solvents to assemble the LMBs with zero-excess Li anode and $\text{LiNi}_{1/3}\text{Mn}_{1/3}\text{Co}_{1/3}\text{O}_2$ as well as LiFePO_4 cathodes, the first cycle loss were as high as 77% and 75%, respectively [81, 82]. Inspired by replacement of carbonate functional group of FEC with dimethylsulfamoyl group, Xue *et al.* developed a novel "full fluorosulfonyl" electrolyte by combining commercially available dimethylsulfamoyl fluoride (FSA) solvent and LiFSI salt. Benefiting from totally removing all carbonate-based solvent from electrolyte system and the formation of a desirable electrode–electrolyte interface (EEI) layers, the FSA-contained LMBs is revealed to possess senior capacity retention, about 2.5 times higher than popular FEC solvent [83]. Although extreme chemical reactivity of Li metal can react with nearly all dipolar aprotic organic solvents, various short ether-based electrolytes with low viscosity were found to be less reactive with the plated Li as compared to the carbonates. Thus, the reduced dendrite formation was realized, and meanwhile, the reduction potential of DME was also as low as 1.68 V against Li/Li^+ , indicating the limited side reaction of Li metal with DME solvent [84]. Beyond these, Aurbach *et al.* proved that the reduced 1,3-dioxolane (DOL) can generate polar oligomer to stabilize the SEI [85]. Consistent with these works, the order of Li plating efficiency in the cells with same parameters is 1.53 M LiTFSI in propylene carbonate (PC) < 1 M LiTFSI in EC:DEC < 1.86 M LiTFSI in EC \approx 1 M LiTFSI + 0.2 M LiNO_3 in DOL:DME, as noted by Nilsson's group [86].

It is usually considered that maximizing the ionic conductivity of electrolyte could result in an optimal cell performance, and thus, the electrolyte with a concentration of 1 M is commercially utilized owing to the high ionic conductivity and suitable cost [87]. However, in the cases of using either concentrated electrolytes or dual-salt electrolytes, drastic differences in cycling stability of LMBs were observed. Thus, the degree of salt dissociation and strength of solvation factors need

to take into consideration in designing a new salt-solvent combination for LMBs because they directly dictate the formation of SEI and the ionic conductivity of electrolyte. For example, each solvated Li^+ can be coordinated by 1.14 oxygens from TFSI⁻ anion while only 0.93 oxygens from FSI⁻ anion, yielded by molecular dynamic simulation in Li^+ solvate structure [15, 88]. Moreover, since the cost of LMBs is also dependent on a variety of factors involving both the salts and solvents, high viscoelastic and costly ionic liquid-based solvent should be avoided. In addition, due to the energy density of LMBs as a function of the average discharge voltage (Power P is equal to the voltage times current), the high-voltage stability of designed salt-solvent combination is another noteworthy factor for high-energy density LMBs. Overall, the state-of-the-art salt-solvent combination is one of the most promising roadmaps to achieve the breakthrough development for commercial LMBs.

1.3 Objective of this research

In consideration of the ultrahigh theoretical specific capacity of the Li metal as anode as well as a higher operating voltage of the LMBs, the Li metal anode is regarded a critical step on the roadmap to improve energy density and develop next-generation highly safe LMBs, and it has already attracted increasing attention. As described, we spotlight the research hotspots, technical hurdles, and practical application of the LMBs. These research hotspots including the designs of current collector substrates, the construction of artificial interface layers, and the combination of electrolyte formulations, which also demonstrate the importance of the electrolyte formulations as indispensable strategies in advanced LMBs in respects to the inducing of a stable and robust electrode/electrolyte interface, decreasing of the parasitic reactions and continuous consumption of metallic Li and electrolytes, suppressing of the Li dendrites growth, prolonging of the cycle lifespan of AFBs, and enabling of the superior electrochemical as well as thermal stability.

Despite these positive developments, there remain many more challenges that need to be addressed to meet the benchmark requirements for commercialization of LMBs. Hereupon, the objective of this study is the development of novel electrolyte formulations to realize a breakthrough in safe LMBs with high energy density as well as long lifespan. By combining the advantages of solid-state-electrolyte, designing an LMB with high ionic conductivity, low interfacial resistance, and excellent cycling lifetime is credible. Meanwhile, the advanced liquid electrolyte formulations can afford unique insights to suppress the growth of Li dendrites, reduce the depletion of lean electrolyte, and importantly, provide broad compatibility with the current manufacturing industry of LIBs.

1.4 Scope of dissertation

Chapter 1: The main progress and remaining obstacles for the development of LMBs are comprehensively discussed and the feasibility and limitations of the state-of-the-art LMBs designs are also emphasized. Moreover, the objectives of this study respect to electrolyte formulations are stated.

Chapter 2: The synthesis and preparation process of various electrolyte formations, characterization and measurements method are presented.

Chapter 3: A PEO-LiTFSI SPE assisted with a bifunctional ionic liquid of tetrabutylphosphonium 2-hydroxypyridine as well as a garnet-type fast-ion conducting ceramic of $\text{Li}_{6.4}\text{La}_3\text{Zr}_{1.4}\text{Ta}_{0.6}\text{O}_{12}$ was fabricated via a solvent-free procedure and applied for the LMBs. The ionic conductivity, electrochemical and thermal stability, lithium-ion transference number were investigated systematically. The synergistic effects between the ionic liquid and the Li salt as well as the PEO chain were testified by experimental investigations and DFT calculations. Moreover, the quasi-

solid-state LMBs assembled with this SPE was fabricated and evaluated.

Chapter 4: A flexible and low cost composite polymer electrolyte (CPE) composed of poly(vinylidene fluoride-hexafluoropropylene) (PVDF-HFP)- $\text{Li}_{6.4}\text{La}_3\text{Zr}_{1.4}\text{Ta}_{0.6}\text{O}_{12}$ (LLZTO) sandwiched by PEO-lithium bis (trifluoromethylsulfonyl)imide (LiTFSI) polymer skin layers in two sides (named as sandwich-type CPE film) was fabricated and applied for the all-solid-state lithium metal battery. The coin cells and pouch cells with this sandwich-type solid-state electrolyte were assembled and evaluated.

Chapter 5: A novel and reliable electrolyte additive, 2-Fluoropyridine (2-FP), was applied to enhance the stability of commercial liquid electrolytes and improve the cycling stability of LMBs. By combining the surface analysis with DFT calculations, the evolution of molecular structure and reaction mechanism of electrolyte additive were identified. The cell performance of LMBs with $\text{LiNi}_{1/3}\text{Mn}_{1/3}\text{Co}_{1/3}\text{O}_2$ as well as LiFePO_4 cathode and routine electrolyte were further evaluated.

Chapter 6: General conclusions of this research and the challenges and prospects for the future work were presented.

References

- [1] K. Xu, Electrolytes and Interphases in Li-Ion Batteries and Beyond, Chem. Rev. 114 (2014) 11503–11618.
- [2] H. Li, Practical evaluation of Li-ion batteries, Joule 3 (2019) 908-919.
- [3] P. Albertus, S. Babinec, S. Litzelman, A. Newman, Status and challenges in enabling the lithium metal electrode for high-energy and low-cost rechargeable batteries, Nat. Energy 3

- (2018) 16–21.
- [4] A.P. Cohn, N. Muralidharan, R. Carter, K. Share, C.L. Pint, Anode-free sodium battery through in situ plating of sodium metal, *Nano Lett.* 17 (2017) 1296–1301.
 - [5] J. Liu, Z. Bao, Y. Cui, E.J. Dufek, J.B. Goodenough, P. Khalifah, Q. Li, B.Y. Liaw, P. Liu, A. Manthiram, Y.S. Meng, V.R. Subramanian, M.F. Toney, V. V Viswanathan, M.S. Whittingham, J. Xiao, W. Xu, J. Yang, X. Q. Yang, J.G. Zhang, Pathways for practical high-energy long-cycling lithium metal batteries, *Nat. Energy* 4 (2019) 180–186.
 - [6] W. Xu, J. Wang, F. Ding, X. Chen, E. Nasybulin, Y. Zhang, J.G. Zhang, Lithium metal anodes for rechargeable batteries, *Energy Environ. Sci.* 7 (2014) 513–537.
 - [7] A.J. Louli, M. Genovese, R. Weber, S.G. Hames, E.R. Logan, J.R. Dahn, Exploring the Impact of Mechanical Pressure on the Performance of Anode-Free Lithium Metal Cells, *J. Electrochem. Soc.* 166 (2019) A1291–A1299.
 - [8] L. Yu, S. Chen, H. Lee, L. Zhang, M.H. Engelhard, Q. Li, S. Jiao, J. Liu, W. Xu, J.G. Zhang, A localized high-concentration electrolyte with optimized solvents and lithium difluoro(oxalate)borate additive for stable lithium metal batteries, *ACS Energy Lett.* 3 (2018) 2059–2067.
 - [9] R. Schmuck, R. Wagner, G. Hörpel, T. Placke, M. Winter, Performance and cost of materials for lithium-based rechargeable automotive batteries, *Nat. Energy* 3 (2018) 267–278.
 - [10] J. Schnell, H. Knörzer, A.J. Imbsweiler, G. Reinhart, Solid versus liquid-A bottom-up calculation model to analyze the manufacturing cost of future high-energy batteries, *Energy Technol.* 8 (2020) 1901237.
 - [11] M.H. Ryou, Y.M. Lee, Y. Lee, M. Winter, P. Bieker, Mechanical surface modification of lithium metal: towards improved Li metal anode performance by directed Li plating, *Adv. Funct. Mater.* 25 (2015) 834–841.

- [12] R. Zhang, X. R. Chen, X. Chen, X. B. Cheng, X.Q. Zhang, C. Yan, Q. Zhang, Lithiophilic sites in doped graphene guide uniform lithium nucleation for dendrite-free lithium metal anodes, *Angew. Chem. Int. Ed.* 56 (2017) 7764-7768.
- [13] J. Wang, H. Wang, J. Xie, A. Yang, A. Pei, C.-L. Wu, F. Shi, Y. Liu, D. Lin, Y. Gong, Y. Cui, Fundamental study on the wetting property of liquid lithium, *Energy Storage Mater.* 14 (2018) 345–350
- [14] A. Pei, G. Zheng, F. Shi, Y. Li, Y. Cui, Nanoscale nucleation and growth of electrodeposited lithium metal, *Nano Lett.* 2017, 17 (2017) 1132-1139.
- [15] V. Pande, V. Viswanathan, Computational Screening of Current Collectors for Enabling Anode-Free Lithium Metal Batteries, *ACS Energy Letters* 4 (2019) 2952-2959.
- [16] S.M. Sharada, T. Bligaard, A. C. Luntz, G.J. Kroes, J. K. Nørskov, SBH10: A benchmark database of barrier heights on transition metal surfaces, *J. Phys. Chem. C* 121 (2017) 19807–19815.
- [17] K. Yan, Z. Lu, H.W. Lee, F. Xiong, P.C. Hsu, Y. Li, J. Zhao, S. Chu, Y. Cui, Selective deposition and stable encapsulation of lithium through heterogeneous seeded growth, *Nat. Energy* 1 (2016) 16010.
- [18] J. Hummelshøj, A. Luntz, J. Nørskov, Theoretical evidence for low kinetic overpotentials in Li-O₂ electrochemistry, *J. Chem. Phys.* 138 (2013) 034703.
- [19] J. Jung, D. Hwang, I. Kristanto, S.K. Kwak, S.J. Kang, Deterministic growth of a sodium metal anode on a pre-patterned current collector for highly rechargeable seawater batteries, *J. Mater. Chem. A* 7 (2019) 9773-9781.
- [20] Y. Li, Y. Li, A. Pei, K. Yan, Y. Sun, C.L. Wu, L.M. Joubert, R. Chin, A. L. Koh, Y. Yu, J. Perrino, B. Butz, S. Chu, Y. Cui, Atomic structure of sensitive battery materials and interfaces revealed by cryo-electron microscopy, *Science* 358 (2017) 506–510.

- [21] Y. Gu, H.Y. Xu, X.G. Zhang, W.W. Wang, J.W. He, S. Tang, J.W. Yan, D.Y. Wu, M.S. Zheng, Q.F. Dong, B.W. Mao, Lithiophilic faceted Cu(100) surfaces: High utilization of host surface and cavities for Lithium metal anodes, *Angew. Chem. Int. Ed.* 58 (2019) 3092-3096.
- [22] A. Milchev, M.I. Montenegro, A galvanostatic study of electrochemical nucleation, *J. Electroanal. Chem.* 333 (1992) 93–102.
- [23] S.S. Zhang, X. Fan, C. Wang, A tin-plated copper substrate for efficient cycling of lithium metal in an anode-free rechargeable lithium battery, *Electrochim. Acta* 258 (2017) 1201-1207.
- [24] S. Liu, X. Zhang, R. Li, L. Gao, J. Luo, Dendrite-free Li metal anode by lowering deposition interface energy with Cu₉₉Zn alloy coating, *Energy Storage Mater.* 14 (2018) 143-148.
- [25] H.N. Umh, J. Park, J. Yeo, S. Jung, I. Nam, J. Yi, Lithium metal anode on a copper dendritic superstructure, *Electrochem. Commun.* 99 (2019) 27-31.
- [26] H. Liu, E. Wang, Q. Zhang, Y. Ren, X. Guo, L. Wang, G. Li, H. Yu, Unique 3D nanoporous/macroporous structure Cu current collector for dendrite-free lithium deposition, *Energy Storage Mater.* 17 (2019) 253-259.
- [27] P. Schmuki, From Bacon to barriers: a review on the passivity of metals and alloys, *J. Solid State Electrochem.* 6 (2002) 145-164.
- [28] A.A. Assegie, J.H. Cheng, L.M. Kuo, W.N. Su, B.J. Hwang, Polyethylene oxide film coating enhances lithium cycling efficiency of an anode-free lithium-metal battery, *Nanoscale* 10 (2018) 6125-6138.
- [29] E. Kazyak, K. N. Wood, N. P. Dasgupta, Improved cycle life and stability of lithium metal anodes through ultrathin atomic layer deposition surface treatments, *Chem. Mater.* 27 (2015) 6457-6462.
- [30] S.S. Zhang, Problem, Status, and Possible Solutions for Lithium Metal Anode of

- Rechargeable Batteries, ACS Appl. Energy Mater. 1 (2018) 910–920.
- [31] D. Lin, Y. Liu, A. Pei and Y. Cui, Nanoscale perspective: Materials designs and understandings in lithium metal anodes, Nano Res. 10 (2017) 4003-4026.
- [32] L.H. Abrha, T.A. Zegeye, T.T. Hagos, H. Sutiono, T.M. Hagos, G.B. Berhe, C.J. Huang, S.K. Jiang, W.N. Su, Y.W. Yang, B.J. Hwang, $\text{Li}_7\text{La}_{2.75}\text{Ca}_{0.25}\text{Zr}_{1.75}\text{Nb}_{0.25}\text{O}_{12}@\text{LiClO}_4$ composite film derived solid electrolyte interphase for anode-free lithium metal battery, Electrochim. Acta 325 (2019) 134825.
- [33] A.A. Assegie, C.C. Chung, M.C. Tsai, W.N. Su, C.W. Chen, B.J. Hwang. Multilayer-graphene-stabilized lithium deposition for anode-Free lithium-metal batteries, Nanoscale 11 (2019) 2710-2720.
- [34] F. Yao, F. Güneş, H.Q. Ta, S.M. Lee, S.J. Chae, K.Y. Sheem, C.S. Cojocaru, S.S. Xie, Y.H. Lee, Diffusion mechanism of lithium ion through basal plane of layered graphene, J. Am. Chem. Soc. 134 (2012) 8646–8654.
- [35] J.S. Kim, D.W. Kim, H.T. Jung, J.W. Choi, Controlled lithium dendrite growth by a synergistic effect of multilayered graphene coating and an electrolyte additive, Chem. Mater. 27 (2015) 2780-2787.
- [36] C. Lee, X. Wei, J.W. Kysar, J. Hone, Measurement of the elastic properties and intrinsic strength of monolayer graphene, Science, 321 (2018) 385–388.
- [37] Z.T. Wondimkun, T.T. Beyene, M.A. Weret, N.A. Sahalie, C.J. Huang, B. Thirumalraj, B.A. Jote, D. Wang, W.N. Su, C.H. Wang, G. Brunklaus, M. Winter, B.J. Hwang, Binder-free ultra-thin graphene oxide as an artificial solid electrolyte interphase for anode-free rechargeable lithium metal batteries, J. Power Sources 450 (2020) 227589.
- [38] Z. Tu, M.J. Zachman, S. Choudhury, K.A. Khan, Q. Zhao, L.F. Kourkoutis, L.A. Archer, Stabilizing protic and aprotic liquid electrolytes at high-bandgap oxide interphases, Chem.

- Mater. 30 (2018) 5655-5662.
- [39] H. Liu, X. Yue, X. Xing, Q. Yan, J. Huang, V. Petrova, H. Zhou, P. Liu, A scalable 3D lithium metal anode, *Energy Storage Mater.* 16 (2019) 505-511.
 - [40] T. Kang, J. Zhao, F. Guo, L. Zheng, Y. Mao, C. Wang, Y. Zhao, J. Zhu, Y. Qiu, Y. Shen, L. Chen, Dendrite-free lithium anodes enabled by a commonly used copper antirusting agent, *ACS Appl. Mater. Interfaces* 12 (2020) 8168-8175.
 - [41] Q. Li, H. Pan, W. Li, Y. Wang, J. Wang, J. Zheng, X. Yu, H. Li, L. Chen, Homogeneous interface conductivity for lithium dendrite-free anode, *ACS Energy Lett.* 3 (2018) 2259-2266.
 - [42] K. Park, J. B. Goodenough, Dendrite-suppressed lithium plating from a liquid electrolyte via wetting of Li_3N , *Adv. Energy Mater.* 7 (2017) 1700732.
 - [43] P.O. Oviroh, R. Akbarzadeh, D. Pan, R.A.M. Coetzee, T.C. Jen, New development of atomic layer deposition: processes, methods and applications, *Sci. Technol. Adv. Mater.* 20 (2019) 465-496.
 - [44] M.S. Kim, J.H. Ryu, Deepika, Y.R. Lim, I.W. Nah, K.R. Lee, L.A. Archer, W.I. Cho, Langmuir-Blodgett artificial solid-electrolyte interphases for practical lithium metal batteries, *Nat. Energy* 3 (2018) 889–898.
 - [45] X. Shen, R. Zhang, X. Chen, X.B. Cheng, X. Li, Q. Zhang, The failure of solid electrolyte interphase on Li metal anode: structural uniformity or mechanical strength ?, *Adv. Energy Mater.* 10 (2020) 1903645.
 - [46] L. Yue, J. Ma, J. Zhang, J. Zhao, S. Dong, Z. Liu, G. Cui, L. Chen, All solid-state polymer electrolytes for high-performance lithium ion batteries, *Energy Storage Mater.* 5 (2016) 139–164.
 - [47] Q. Liu, Z. Geng, C. Han, Y. Fu, S. Li, Y. B. He, F. Kang, B. Li, Challenges and perspectives

- of garnet solid electrolytes for all solid-state lithium batteries, *J. Power Sources* 389 (2018) 120–134.
- [48] Z. Zhang, Y. Shao, B. Lotsch, Y.S. Hu, H. Li, J. Janek, L.F. Nazar, C.W. Nan, J. Maier, M. Armand, L. Chen, New horizons for inorganic solid state ion conductors, *Energy Environ. Sci.* 11 (2018) 1945–1976.
- [49] R. Fang, S. Zhao, Z. Sun, D.W. Wang, H.M. Cheng, F. Li, More reliable lithium-sulfur batteries: status, solutions and prospects, *Adv. Mater.* 29 (2017) 1606823.
- [50] J. Mindemark, M. J. Lacey, T. Bowden, D. Brandell, Beyond PEO-alternative host materials for Li⁺-conducting solid polymer electrolytes, *Prog. Polym. Sci.* 81 (2018) 114–143.
- [51] X. Fan, L. Chen, O. Borodin, X. Ji, J. Chen, S. Hou, T. Deng, J. Zheng, C. Yang, S.-C. Liou, K. Amine, K. Xu, C.S. Wang, Non-flammable electrolyte enables Li-metal batteries with aggressive cathode chemistries, *Nat. Nanotechnol.* 13 (2018) 715.
- [52] Y. Jin, K. Liu, J. Lang, D. Zhuo, Z. Huang, C. Wang, H. Wu, Y. Cui, An intermediate temperature garnet-type solid electrolyte-based molten lithium battery for grid energy storage, *Nat. Energy* 3 (2018) 732–738.
- [53] Y. Yamada, J. Wang, S. Ko, E. Watanabe, A. Yamada, Advances and issues in developing salt-concentrated battery electrolytes, *Nat. Energy* 4 (2019) 269–280.
- [54] L. Suo, Y.S. Hu, H. Li, M. Armand, L. Chen, A new class of solvent-in-salt electrolyte for high-energy rechargeable metallic lithium batteries, *Nat. Commun.* 4 (2013) 1481.
- [55] T. Hosaka, K. Kubota, H. Kojima, S. Komaba, Highly concentrated electrolyte solutions for 4 V class potassium-ion batteries, *Chem. Commun.* 54 (2018) 8387–8390.
- [56] J. Qian, W.A. Henderson, W. Xu, P. Bhattacharya, M. Engelhard, O. Borodin, J.G. Zhang. High rate and stable cycling of lithium metal anode, *Nat. Commun.* 6 (2015) 6362.
- [57] J. Vatamanu, O. Borodin, G. D. Smith, Molecular dynamics simulation studies of the

- structure of a mixed carbonate/LiPF₆ electrolyte near graphite surface as a function of electrode potential, *J. Phys. Chem. C* 116 (2011) 1114–1121.
- [58] C. Ling, D. Banerjee, M. Matsui, Study of the electrochemical deposition of Mg in the atomic level: why it prefers the non-dendritic morphology, *Electrochim. Acta* 76 (2012) 270–274.
- [59] T.T. Beyene, B.A. Jote, Z.T. Wondimkun, B.W. Olbassa, C.J. Huang, B. Thirumalraj, C.H. Wang, W.N. Su, H. Dai, B.J. Hwang, Effects of concentrated salt and resting protocol on solid electrolyte interface formation for improved cycle stability of anode-free lithium metal batteries, *ACS Appl. Mater. Interfaces* 11 (2019) 31962–31971.
- [60] T.T. Hagos, B. Thirumalraj, C.J. Huang, L.H. Abrha, T.M. Hagos, G.B. Berhe, H.K. Bezabh, J. Cherng, S.F. Chiu, W.N. Su, B.J. Hwang, Locally concentrated LiPF₆ in a carbonate-based electrolyte with fluoroethylene carbonate as a diluent for anode-free lithium metal batteries, *ACS Appl. Mater. Interfaces* 11 (2019) 9955–9963.
- [61] J. Vatamanu, O. Borodin, Ramifications of water-in-salt interfacial structure at charged electrodes for electrolyte electrochemical stability, *J. Phys. Chem. Lett.* 8 (2017) 4362–4367.
- [62] J. Alvarado, M.A. Schroeder, T.P. Pollard, X. Wang, J.Z. Lee, M. Zhang, T. Wynn, M. Ding, O. Borodin, Y.S. Meng, K. Xu, Bisalt ether electrolytes: a pathway towards lithium metal batteries with Ni-rich cathodes, *Energy Environ. Sci.* 12 (2019) 780–794.
- [63] T.T. Beyene, H.K. Bezabh, M.A. Weret, T.M. Hagos, C.J. Huang, C.H. Wang, W.N. Su, H. Dai, B.J. Hwang. Concentrated dual-salt electrolyte to stabilize Li metal and increase cycle life of anode free Li-metal batteries, *J. Electrochem. Soc.* 166 (2019) A1501–A1509.
- [64] R. Rodriguez, R.A. Edison, R.M. Stephens, H.H. Sun, A. Heller, C.B. Mullins. Separator-free and concentrated LiNO₃ electrolyte cells enable uniform lithium electrodeposition, *J. Mater. Chem. A* 8 (2020) 3999–4006.

- [65] R. Weber, M. Genovese, A.J. Louli, S. Hames, C. Martin, I.G. Hill, J.R. Dahn. Long cycle life and dendrite-free lithium morphology in anode-free lithium pouch cells enabled by a dual-salt liquid electrolyte, *Nat. Energy* 4 (2019) 683-689.
- [66] H Liu, X.B. Cheng, Z. Jin, R. Zhang, G. Wang, L.Q. Chen, Q.B. Liu, J.Q. Huang, Q. Zhang, Recent advances in understanding dendrite growth on alkali metal anodes, *EnergyChem* 1 (2019)100003.
- [67] K. Matsumoto, K. Inoue, K. Nakahara, R. Yuge, T. Noguchi, K. Utsugi, Suppression of aluminum corrosion by using high concentration LiTFSI electrolyte, *J. Power Sources* 231 (2013) 234-238.
- [68] H. Zhang, G. G. Eshetu, X. Judez, C. Li, L. M. R. Martínez, and M. Armand, Electrolyte additives for lithium metal anodes and rechargeable lithium metal batteries: progresses and perspectives, *Angew. Chem. Int. Ed.* 57 (2018) 15002-15027.
- [69] N. von Aspern, G.V. Röschenthaler, M. Winter, I. Cekic-Laskovic, Fluorine and lithium: ideal partners for high-performance rechargeable battery electrolytes, *Angew. Chem. Int. Ed.* 58 (2019)15978-16000.
- [70] Y. Ma, Z. Zhou, C. Li, L. Wang, Y. Wang, X. Cheng, P. Zuo, C. Du, H. Huo, Y. Gao, G. Yin, Enabling reliable lithium metal batteries by a bifunctional anionic electrolyte additive, *Energy Storage Mater.* 11 (2018) 197–204.
- [71] T. Yang, W. Fan, C. Wang, Q. Lei, Z. Ma, L. Yu, X. Zuo, J. Nan, 2,3,4,5,6-Pentafluorophenyl methanesulfonate as a versatile electrolyte additive matches $\text{LiNi}_{0.5}\text{Co}_{0.2}\text{Mn}_{0.3}\text{O}_2$ /graphite batteries working in a wide-temperature range, *ACS Appl. Mater. Interfaces* 10 (2018) 31735–31744.
- [72] X.Q. Zhang, X.B. Cheng, X. Chen, C. Yan, Q. Zhang, Fluoroethylene carbonate additives to render uniform Li deposits in lithium metal batteries, *Adv. Funct. Mater.* 27 (2017)

1605989.

- [73] L. Yu, S. Chen, H. Lee, L. Zhang, M. H. Engelhard, Q. Li, S. Jiao, J. Liu, W. Xu, J. G. Zhang, A localized high-concentration electrolyte with optimized solvents and lithium difluoro(oxalate)borate additive for stable lithium metal batteries, *ACS Energy Lett.* 3 (2018) 2059-2067.
- [74] D.J. Yoo, K.J. Kim, J.W. Choi, The synergistic effect of cation and anion of an ionic liquid additive for lithium metal anodes, *Adv. Energy Mater.* 8 (2018) 1702744.
- [75] S. Liu, G. Li, X. Gao, Lanthanum nitrate as electrolyte additive to stabilize the surface morphology of lithium anode for lithium–sulfur battery, *ACS Appl. Mater. Interfaces* 8 (2016) 7783–7789.
- [76] J. Qian, W. Xu, P. Bhattacharya, M. Engelhard, W.A. Henderson, Y. Zhang, J.G. Zhang, Dendrite-free Li deposition using trace-amounts of water as an electrolyte additive, *Nano Energy* 15 (2015) 135–144.
- [77] W. Li, H. Yao, K. Yan, G. Zheng, Z. Liang, Y.M. Chiang, Y. Cui, The synergetic effect of lithium polysulfide and lithium nitrate to prevent lithium dendrite growth, *Nat. Commun.* 6 (2015) 7436.
- [78] X.Q. Zhang, X. Chen, X.B. Cheng, B.Q. Li, X. Shen, C. Yan, J.Q. Huang, Q. Zhang, Highly stable lithium metal batteries enabled by regulating the solvation of lithium ions in nonaqueous electrolytes, *Angew. Chem. Int. Ed.* 57 (2018) 5301-5305.
- [79] D. Aurbach, M. L. Daroux, P. W. Faguy, E. Yeager, Identification of surface films formed on lithium in propylene carbonate solutions, *J. Electrochem. Soc.* 134 (1987) 1611-1620.
- [80] K. Leung, C. M. Tenney, Toward first principles prediction of voltage dependences of electrolyte/electrolyte interfacial processes in lithium ion batteries, *J. Phys. Chem. C.* 117 (2013) 24224-24235.

- [81] J.J. Woo, V.A. Maroni, G. Liu, J.T. Vaughey, D.J. Gosztola, K. Amine, Z. Zhang, Symmetrical impedance study on inactivation induced degradation of lithium electrodes for batteries beyond lithium-ion, *J. Electrochem. Soc.* 161 (2014) A827–A830.
- [82] T. Doi, Y. Shimizu, M. Hashinokuchi, M. Inaba, Dilution of highly concentrated LiBF_4 /propylene carbonate electrolyte solution with fluoroalkyl ethers for 5-V $\text{LiNi}_{0.5}\text{Mn}_{1.5}\text{O}_4$ positive electrodes, *J. Electrochem. Soc.* 164 (2017) A6412–A6416.
- [83] W. Xue, Z. Shi, M. Huang, S. Feng, C. Wang, F. Wang, J. Lopez, B. Qiao, G. Xu, W. Zhang, Y. Dong, R. Gao, Y. Shao-Horn, J.A. Johnson, J. Li. FSI-inspired solvent and “full fluorosulfonyl” electrolyte for 4 V class lithium-metal batteries, *Energy Environ. Sci.* 13 (2020) 212-220.
- [84] M.S. Park, S.B. Ma, D.J. Lee, D. Im, S.G. Doo, O. Yamamoto, A highly reversible lithium metal anode, *Sci. Rep.* 4 (2014) 3815-3822.
- [85] D. Aurbach, Review of selected electrode–solution interactions which determine the performance of Li and Li ion batteries, *J. Power Sources*, 89 (2000) 206-218.
- [86] V. Nilsson, A. Kotronia, M. Lacey, K. Edström, P. Johansson. Highly concentrated LiTFSI-EC electrolytes for lithium metal batteries, *ACS Appl. Energy Mater.* 3 (2020) 200-207.
- [87] K. Xu, Electrolytes and interphases in Li-ion batteries and beyond, *Chem. Rev.* 114 (2014) 11503-11618.
- [88] V. Lesch, S. Jeremias, A. Moretti, S. Passerini, A. Heuer, O. Borodin, A combined theoretical and experimental study of the influence of different anion ratios on lithium ion dynamics in ionic liquids, *J. Phys. Chem. B* 118 (2014) 7367-7375.

Chapter 2 Experimental

2.1 Chemical reagents

Table 2.1 Chemical reagents used in this study.

Chemical reagents		Grade	Producer
Poly (ethylene oxide)	PEO	$M_w = 6 \times 10^5$	SIGMA-ALDRICH
Lithium			
Bis(trifluoromethanesulfonyl)imide	LiTFSI	>98.0%	SIGMA-ALDRICH
Tetrabutylphosphonium hydroxide	TBPOH	40 wt. %	SIGMA-ALDRICH
2-Hydroxypyridine	2-HP	97.0%	SIGMA-ALDRICH
$Li_{6.4}La_3Zr_{1.4}Ta_{0.6}O_{12}$	LLZTO	$D = 5.6 \mu m$	TOSHIMA CORP.
Poly(vinylidene fluoride-co-hexafluoropropylene)	PVDF-HFP	$M_w = 4 \times 10^5$	SIGMA-ALDRICH
2-Fluoropyridine	2-FP	98.0%	SIGMA-ALDRICH
Pyridine	--	99.0%	WAKO
1 M $LiPF_6$ in ethylene carbonate (EC): diethyl carbonate (DEC) (1:1 vol.%)	1 M $LiPF_6$ in EC: DEC) (1:1 vol.%)	99.0%	SIGMA-ALDRICH
1 M LiTFSI in 1,3-dioxolane (DOL): 1,2-Dimethoxyethane (DME) (1:1 vol.%) with 1% $LiNO_3$	1 M LiTFSI in DOL: DME (1:1 vol.%) +1% $LiNO_3$	99.0+%	XIAMEN TOB NEW ENERGY TECHNOLOGY
Li foil	Li	100 μm	HONJO CHEMICAL
Lithium Iron(II) Phosphate	$LiFePO_4$	1.5 mAh cm^{-2}	HOHSEN CORP.
Lithium cobalt oxide	$LiCoO_2$	1.5 mAh cm^{-2}	HOHSEN CORP.
Lithium Nickel Manganese Cobalt Oxide	$LiNi_{1/3}Mn_{1/3}Co_{1/3}O_2$	1.5 mAh cm^{-2}	HOHSEN CORP.

2.2 Characterization

2.2.1 Scanning Electron Microscopy (SEM) and Energy Dispersive X-Ray Spectrometer (EDS)

The surface morphology and elemental distribution of sample were performed via a scanning electron microscopy (SEM, Hitachi SU8010, Japan) system equipped with a Horiba Scientific energy dispersive spectrometer (EDS) at an acceleration voltage of 15-20.0 kV. The dried sample was put on conductive carbon tape which attached to the specimen stub.

2.2.2 Atomic force microscopy (AFM)

The AFM images were collected using an AFM Nano Navi II instrument, Japan at ambient temperature.

2.2.3 X-Ray Diffraction (XRD)

The phase composition of the material was characterized by XRD (Rigaku Smart Lab X-Ray Diffractometer, Japan) with Cu K α radiation ($\lambda = 1.5405 \text{ \AA}$) in a 2θ range from 10° to 60° , and the scanning rate of $10^\circ \cdot \text{min}^{-1}$. Phase identification was achieved through comparison of obtained XRD patterns to those of “Joint Committee on Powder Diffraction Standards (JCPDS)”.

2.2.4 Differential Scanning Calorimetry (DSC)

Firstly, all the samples were sealed in an Al pan, thereafter, the DSC measurements were carried out on a TA Instrument (Seiko Instrument Inc. EXSTAR 6000, Japan) with a heating rate of $10^\circ \text{C} \cdot \text{min}^{-1}$ under an Ar atmosphere.

2.2.5 Thermogravimetric (TG)

The TG curves was recorded using a TA machine (TA-60WS, SHIMADZU, Japan) with a DTG-60 analysis model under N₂ atmosphere.

2.2.6 X-ray photoelectron spectroscopy (XPS)

The chemical compositions of surface film including the SEI layer on the Li anode were

measured by X-ray photoelectron spectroscopy (Thermo Fisher Scientific ESCALAB 250Xi XPS System, USA) using 200W monochromatized Al K α radiation as the X-ray source. The contents of different species in the SEI layers were obtained by fitting the whole XPS spectra using CasaXPS software.

2.2.7 Contact angle analysis

The contact angle measurement was carried out by using a contact angle meter (DMe-201, Kyowa Interface Science Co. Ltd., Japan) at room temperature.

2.3 Electrochemical measurement

The electrochemical impedance spectroscopy (EIS), direct current (DC) polarization, and voltammetry test of cell were carried out using a VersaSTAT 4 electrochemical station (Princeton Applied Research, USA). The cycling performance of batteries were investigated by charge/discharge galvanostatic tests with HJ1020mSD8 (Hokuto Denko Corporation Co., Ltd., Japan) and LANHE CT2001A (Wuhan LAND Electronics Co., Ltd., China) cell testing system.

In detail, the ionic conductivity measurements electrolytes were sandwiched between two stainless steel blocking electrodes and mounted in the coin cell. The EIS of electrolyte was measured with an alternating current (AC) amplitude of 5 mV in the frequency range of 10^5 -0.1 Hz. The lithium-ion transference (t_{Li+}) number of the electrolyte was measured in a symmetric Li/electrolyte/Li cell with a DC polarization voltage of 10 mV associated with the EIS measurement. The initial (I_0) and steady (I_{ss}) currents were obtained from a DC polarization test. R_0 and R_{ss} were obtained from the EIS measurement with the frequency between 1 MHz and 0.01 Hz, representing the interface impedance before and after the test, respectively. The electrochemical stability of the electrolytes was evaluated via voltammetry with the stainless-steel plate or cathode material as working electrode and Li metal as the reference and counter electrodes.

Chapter 3 Bifunctional ionic liquid and conducting ceramic co-assisted quasi-solid-state polymer electrolyte for lithium metal batteries

1. Introduction

Nowadays, almost all commercial lithium-ion batteries (LIBs) use liquid electrolytes with high lithium ion conductivity. However, the leakage, flammability, chemical and thermal instability of the liquid electrolytes result in safety problems. With the wide applications of electric vehicles and portable devices, it becomes more and more important to develop safe LIBs [1]. Recently, the lithium metal batteries (LMBs) with solid-state or quasi-solid-state electrolytes are being intensively pursued by many researchers [2, 3]. To date, sulfide-based electrolytes such as $\text{Li}_2\text{S-P}_2\text{S}_5$, $\text{Li}_2\text{S-SiS}_2$ and $\text{Li}_{10}\text{GeP}_2\text{S}_{12}$ [4-6]; oxides-based electrolytes such as $\text{Li}_{1+x}\text{Al}_x\text{Ti}_{2-x}(\text{PO}_4)_3$ (LATP) [7], $\text{Li}_x\text{La}_3\text{M}_2\text{O}_{12}$ ($\text{M} = \text{Ta, Nb, Zr}$) [8] and $\text{Li}_{3x}\text{La}_{2/3-x}\text{TiO}_3$ [9], and solid polymer electrolytes (SPEs) such as poly-(ethylene oxide) (PEO)-lithium salts based ones like PEO-lithium bis-trifluoromethanesulphonimide (LiTESI) [10], PEO-LiTFSI (lithium bis(trifluoromethylsulfonyl)imide)- $\text{Mg}_2\text{B}_2\text{O}_5$ [11], PEO- $\text{LiClO}_4\text{-Li}_{0.33}\text{La}_{0.557}\text{TiO}_3$ [12], cellulose-poly(propylene carbonate)-lithium salts [13], interpenetrating poly(ether acrylate)-lithium salts [14] and PVDF (polyvinylidene fluoride)-lithium salts [15] have been developed as the solid-state electrolytes for LMBs. Among them, sulfide- and oxide-based electrolytes are always fabricated using a complicated synthesis process at high temperatures, and as they are assembled with the electrodes, large electrolyte-electrode interfacial resistance is always unavoidable, limiting their large-scale applications. Also, for sulfide-based electrolytes, toxic H_2S is easily generated in the presence of moisture and results in some safety problem [16]. In contrast, SPEs have the advantage to reduce the electrolyte-electrode interfacial resistance despite the low ionic conductivity at room

temperature [8]. To date, it is still full of challenges to develop solid electrolytes with high performance as well as stability for LMBs.

The PEO-lithium salts (e.g., LiTFSI, LiBF₄, and LiClO₄) based SPEs with relatively high ability to transfer Li⁺ ions are the most studied SPEs [17]. Especially, they are easily modified by sulfides and/or oxides to improve the performance [18]. Several strategies including introducing ionic liquids (ILs), ceramic fillers, and block/grafted copolymers have been explored to improve the low-temperature ionic conductivity of SPEs [16, 19]. Herein, introducing of ILs into the SPEs is one of the most promising approaches to further improve the performance since the ILs have many unique characteristics such as low volatility, good thermal stability, wide electrochemical window, low flammability and tunable ionic conductivity [20, 21]. Various types of ILs have been applied to modify SPEs. For instance, the ILs containing 1-ethyl-3-methylimidazolium (EMIM⁺) [22], tetraethylammonium (N₂₂₂₂⁺) [23], N-methyl-N-propylpyrrolidinium (Py₁₃⁺) [24], tributylmethylphosphonium (P₁₄₄₄⁺) [25], and Li(tetraglyme) (Li(G4)₁⁺) [26] cations or tetrafluoroborate (BF₄⁻) [27], tricyanomethide (C(CN)₃⁻) [28], trifluoromethylsulfonate (TfO⁻) [29], bis(trifluoromethyl-sulfonyl)imide (TFSI⁻) [30], and bis(pentafluoroethane-sulfonyl)imide (BETI⁻) [31] anions are the typical ones. It is also reported that incorporating the ionic liquid into a polymer matrix could result in a quasi-solid-state-electrolyte [1].

In our previous study, a new kind of IL called tetrabutylphosphonium 2-hydroxypyridine (TBPHP) was successfully synthesized through a solvent-free procedure and applied in CO₂ capture [32]. Based on the experimental investigations and DFT calculations, it was confirmed that the α -C₁ atom of cation TBP⁺ in TBPHP has high electronegativity after the proton transfer so that it possesses an intense interaction with the carbon atom in the CO₂ molecule. Similarly, since PEO has the -CH₂-CH₂-O- repeating units with high electronegativity site [33, 34], which could also have a strong interaction with the cation of TBPHP. Meanwhile, the crystallinity of PEO could

be reduced via the cross-linking between the polymer chains of PEO and TBPHP [35, 36], which can enhance the performance of SPEs. In this study, TBPHP was used for the modification of PEO-lithium salts based SPEs.

$\text{Li}_{6.4}\text{La}_3\text{Zr}_{1.4}\text{Ta}_{0.6}\text{O}_{12}$ (LLZTO), a garnet-type fast-ion conducting ceramic electrolyte with a high bulk conductivity (more than $10^{-3} \text{ S cm}^{-1}$ at ambient temperature), a wide potential window range (above 6 V vs. Li/Li^+), low cost (only 0.037\$ g^{-1}), high elastic constant as well as shear moduli (more than 55 GPa), and excellent chemical stability against Li metal, is one of the most promising electrolyte candidates for the solid-state LMBs [37, 38]. As it was used as the ceramic filler in the polymer matrix, it is found that the ionic conductivity, mechanical property and thermal stability of the whole SPEs were effectively enhanced [39, 40].

In this study, the bifunctional TBPHP and the cubic garnet-type structure electrolyte LLZTO were used together to modify the PEO-LiTFSI based SPEs. With the assistance of both the TBPHP and LLZTO, it is expected to obtain a flexible and stable composite SPE membrane with improved ionic conductivity, widened thermal and electrochemical stability window, and enhanced mechanical and interfacial properties. As a result, a quasi-solid-state $\text{LiFePO}_4|\text{Li}$ battery assembled with $\text{PEO}_8\text{-LiTFSI-TBHP-12.5wt\% LLZTO}$ SPE (PEO/LiTFSI mole ratio of 8) exhibited excellent rate performance and cycle stability with a negligible discharge capacity decay up to 151 mAh g^{-1} even after 100 cycles at 50 °C. Moreover, the fabricated flexible pouch cell also showed excellent performance, indicating its feasibility for the flexible quasi-solid-state LMBs.

3.2 Experimental

3.2.1 Preparation of ionic liquid and electrolyte membrane

Firstly, a convenient liquid-liquid phase reaction method was utilized to synthesize ionic liquids (IL) of tetrabutylphosphonium 2-hydroxypyridine (IL TBPHP). In brief, a certain amount of 2-hydroxypyridine (2-HP) was dissolved in ethanol, and then, added dropwise into

tetrabutylphosphonium hydroxide solution (TBP), and kept stirring for 24 hours at an ambient temperature; subsequently, transferred to a vacuum oven at 70 °C for 48 h.

Based on the measurements, the following information on TBPHP can be summarized: TBPHP is a kind of room-temperature ionic liquid with thermal stability up to 250 °C and decomposed completely at about 350 °C. It has a viscosity of 193 cP at 20 °C, an ionic conductivity of $5.65 \times 10^{-4} \text{ S} \cdot \text{cm}^{-1}$ at 30 °C, a melting point of around -70 °C, an electrochemical window of 4.06 V (Pt). The dipole moment of cation and anion of TBPHP is 11.17 D with binding energy of -343.88 kJ mol⁻¹.

Blank SPE was prepared with a PEO/LiTFSI mole ratio of 8 since this ratio (PEO₈-LiTFSI) showed a high ionic conductivity. Then, the IL TBPHP added into it, and the optimum amount was determined by varying the ILs amount from 0 to 20 wt% (referred to as PEO₈-LiTFSI-X% TBPHP). It was found that the PEO₈-LiTFSI-15%TBPHP mixture was the best one. Thereafter, the LLZTO powder mixed with PEO₈-LiTFSI-15%TBPHP powder, and its optimum amount was determined by adjusting the LLZTO powder amount from the LLZTO powder amount from 0 to 15 wt%. (i.e., 0:100, 2.5: 97.5, 5: 95, 7.5: 92.5, 10: 90, 12.5: 97.5 and 15: 85, respectively, referred to as PEO₈-LiTFSI-TBPHP- X% LLZTO).

To understand the effects of cation and anion in TBPHP for SPE, the PEO₈-LiTFSI-15%TBP and PEO₈-LiTFSI-15% HP were prepared and measured. Due to the TBP is a strong base electrolyte since it has a pH of 14.66 at 1 mol L⁻¹, TBP⁺ cations should exist in the PEO₈-LiTFSI-15%TBP SPE. As for PEO₈-LiTFSI-15%HP, in which HP⁻ anions was resulted from 2-HP reaction with LiOH, and in this case, HP⁻ anions should be also existed.

In more detail, PEO₈-LiTFSI-15%TBP and PEO₈-LiTFSI-15% HP prepared as follows. Firstly, TBP solution was dried in a vacuum oven at 60 °C for 24 h to remove the moisture. Then, the calculated amount of the TBP was directly mixed with PEO₈-LiTFSI to obtain PEO₈-LiTFSI-

15%TBP. Meanwhile, 2-hydroxypyridine (2-HP) and LiOH with a mole ratio of 1 were grinded in a carnelian mortar for 10 min, and then dried in a vacuum oven at 60 °C for 24 h, and finally, mixed with PEO₈-LiTFSI to obtained PEO₈-LiTFSI-15% HP.

The obtained PEO₈-LiTFSI-15%TBP and PEO₈-LiTFSI-15%HP were ground continuously in a carnelian mortar until a rough sheet film was obtained. After that, the film was sealed and transferred to a vacuum oven at 75 °C and maintained for 12 h. Finally, the composite SPE membrane was prepared by pressing under 2 MPa without any organic solvent at ambient temperature for 5 h. As such, a uniform composite membrane with a thickness of ~100 μm was obtained. Comparing with the solvent casting method, this one should be an environment-friendly procedure since it can reduce the emission of volatile organic compounds (VOCs). Unless otherwise noted, all samples prepared in an Ar-filled glove box.

3.2.2 Characterizations and electrochemical measurement

The morphology of the electrolyte membrane was characterized via a SEM technology. The crystal structure of SPE was determined by X-ray diffraction (XRD) in the 2θ range of 10-60°. Differential scanning calorimetry (DSC) measurements were carried out on a TA Instrument (Seiko Instrument Inc. EXSTAR 6000) with a heating rate of 10 °C min⁻¹ from 25 to 150 °C under an Ar atmosphere. TGA curves were obtained by a thermogravimetric analysis instrument (DTG-60H) with a heating rate of 10 °C min⁻¹ from 25 °C to 550 °C under N₂ atmosphere.

For electrochemical measurements, the obtained composite SPE was sandwiched between two stainless steel blocking electrodes. Electrochemical impedance spectroscopy was measured by a Princeton electrochemical station VersaSTAT 4 with an AC amplitude of 5 mV in the frequency range of 10⁵-0.1 Hz at temperatures ranged from 25 to 80 °C. Ionic conductivity σ was calculated based on the following equation:

$$\sigma = \frac{R}{L \cdot S} \quad (1)$$

Where R represents the resistance according to EIS measurement, L represents the thickness of the composite SPE membrane, and S stands for the area of the polymer electrolyte membrane. In this work, the area of the polymer electrolyte membrane equals to the area of stainless-steel blocking electrodes.

The lithium-ion transference (t_{Li+}) number of the SPE was measured in a symmetric Li/SPE/Li cell with a DC polarization voltage of 10 mV associated with the AC impedance measurement. The initial (I_0) and steady (I_{ss}) currents were obtained from a DC polarization test. R_0 and R_{ss} were obtained from the AC impedance measurement with the frequency between 1 MHz and 0.01 Hz, representing the interface impedance before and after the test, respectively. t_{Li+} was calculated by the following equation:

$$t_{Li+} = \frac{I_{ss}(\Delta v - I_0 R_0)}{I_0(\Delta v - I_{ss} R_{ss})} \quad (2)$$

Where ΔV is the voltage polarization applied, I_{ss} and R_{ss} are the steady-state current and resistance, respectively, I_0 and R_0 are the initial current and resistance, respectively. Potentiostatic coulometry measurement was employed to evaluate the electrical conductivity of the prepared SPEs at 50 °C.

The electrochemical stability window of the SPE was evaluated via linear sweep voltammetry in the potential range from 2.5 to 6.2 V at a scanning rate of 1 mV s⁻¹ with a stainless-steel plate as working electrode and Li metals as the reference and counter electrodes.

3.2.3 Cell assembly and test

LiFePO₄ (LFP) cathode and Li metal anode were employed to assemble solid-state batteries. Herein, LFP, carbon black (Super-P), and poly (vinylidene fluoride) (PVDF) binder (80:10:10 by weight) were thoroughly dispersed in *N*-methyl-2-pyrrolidone solvent and the resultant slurry was coated on Al foil by using a film applicator (BEVS Industrial Co., Ltd. Japan). The electrode sheets

were dried at 100 °C for 24 h before use. The typical active material loading amount was about $2.0 \pm 0.1 \text{ mg cm}^{-2}$. For cells assembly, the obtained SPE membrane (diameter: 16 mm) was sandwiched between different cathode foil (diameter: 12 mm) and Li foil (diameter: 12 mm), and placed into CR2025-type coin cell case, and then pressed at 750 psi for further measurements.

CR2025-type $\text{LiFePO}_4|\text{Li}$ coin cells with the prepared SPEs were tested with an SD8data testing system (Hokuto Denko Corporation Co., Ltd. Japan). All the batteries were assembled without using a separator or additional liquid electrolyte in an Ar-filled glove box (with water and oxygen contents of below 0.01 ppm).

3.2.4 Computational details

The binding energy (E_b) between the cation and anion ion in the prepared SPEs was calculated using the COSMO continuum solvation model of DMOL3 module in Material Studio. The binding energy (E_b) was defined as following: $E_b = E_{\text{combine}} - E_{\text{cation}} - E_{\text{anion}}$, where E_{combine} , E_{cation} , and E_{anion} are the total energies of the cation-anion complex, the cation, and anion, respectively.

3.3 Results and discussion

3.3.1 Physicochemical properties of the prepared SPE membranes

Simple tests identified that the obtained composite SPE membrane was freestanding with excellent mechanical flexibility (**Fig. 3.1A, B, C, and D**), indicating that it is feasible for fabricating wearable LMBs. SEM images show that all SPE membranes had smooth surfaces without any phase separation (**Figs. 3.1E, F, and G**). From the cross-sectional SEM image of $\text{PEO}_8\text{-LiTFSI-TBPHP-12.5\%LLZTO}$, it is observed that the thickness was around 100 μm , where the PEO-Li salt polymer and ceramic particles of LLZTO were thoroughly intermingled (**Fig. 1H**). Besides, in the presence of IL of TBPHP, the whole film was in a solid state at room temperature, indicating that the IL was well combined with other materials. In this study, to increase the mechanical strength of PEO-based electrolyte, the garnet-type LLZTO electrolyte was

incorporated since it has the high elastic constant as well as shear moduli. However, the high mechanical strength could affect the interface contact between the electrolyte and the electrode. In this case, the addition of IL TBPHP could wet the electrodes so that the interface contact becomes well. To obtain the optimum IL TBPHP addition amount, the electrolytes with different amounts of IL TBPHP were prepared and tested. We found that the electrolyte showed a huge interface resistance due to the poor contact when the ratio of TBPHP in electrolyte was over 30%. Therefore, the optimum IL TBPHP addition amount is important for such electrolytes.

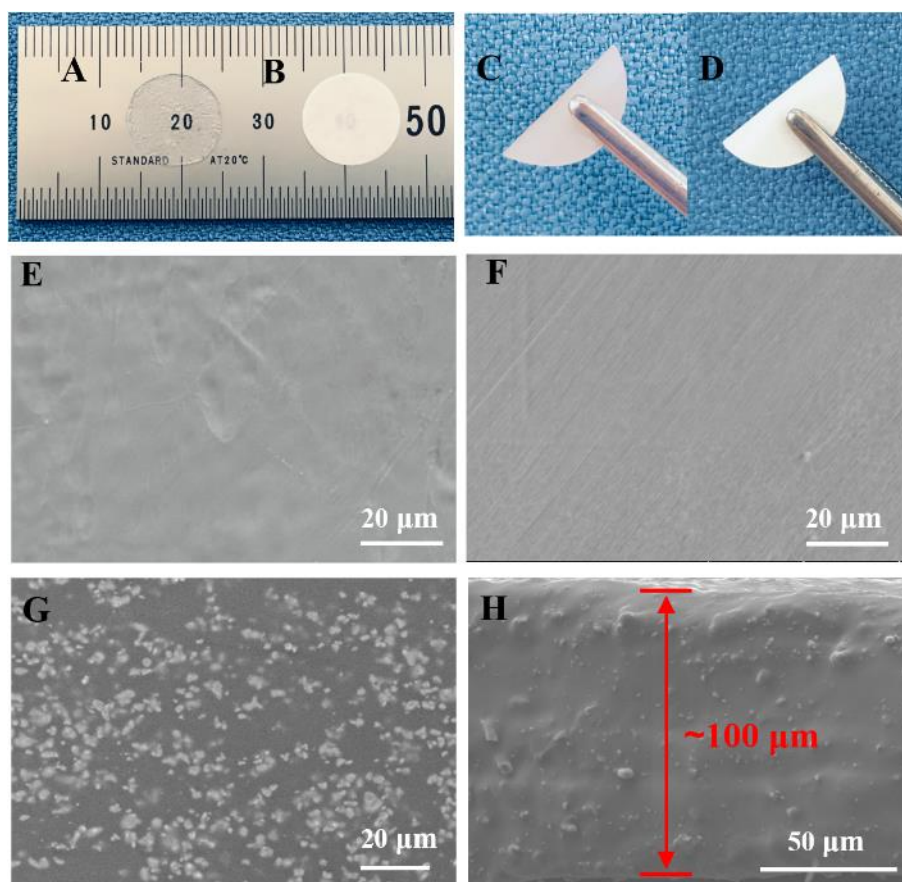


Fig. 3.1 Photographs of the prepared (A, C) PEO₈-LiTFSI-15%TBPHP and (B, D) PEO₈-LiTFSI-TBPHP-12.5%LLZTO SPE membranes at flat and bended states; The typical surface morphologies of (E) PEO₈-LiTFSI, (F) PEO₈-LiTFSI-15%TBPHP and (G) PEO₈-LiTFSI-TBPHP-12.5%LLZTO; (H) cross-sectional SEM image of PEO₈-LiTFSI-TBPHP-12.5%LLZTO.

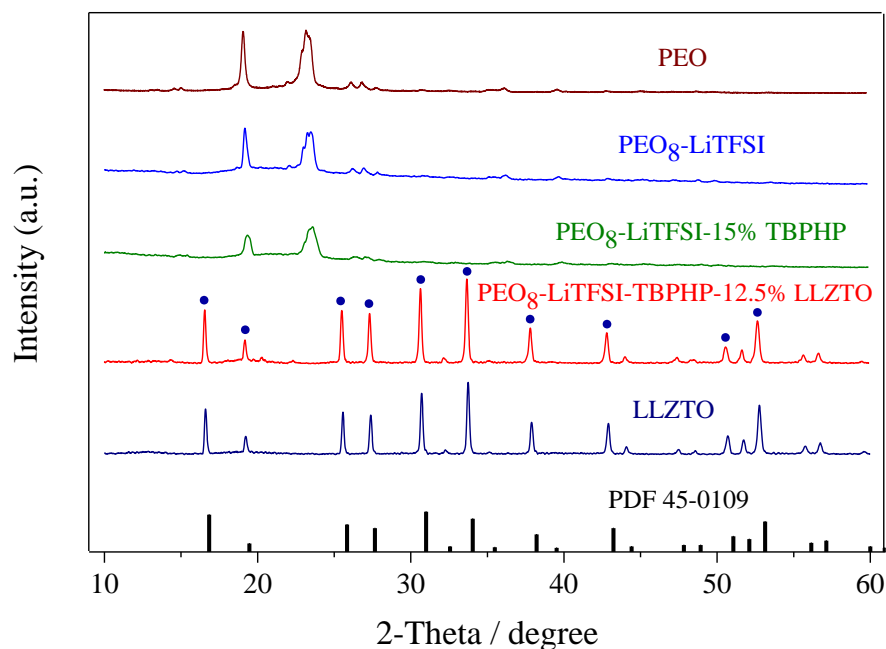


Fig. 3.2 XRD patterns of the pure PEO, SPE samples, and LLZTO ceramic powder. The XRD pattern of cubic garnet $\text{Li}_5\text{La}_3\text{Nb}_2\text{O}_{12}$ (JCPDS: 45-0109) is used as the reference.

As can be seen from **Fig. 3.2**, XRD pattern of the pure PEO consisted of two intense peaks ($2\theta = 19^\circ$ and 23°), indicating the presence of crystalline phase of PEO. After the incorporation with the LiTFSI and TBPHP ($\text{PEO}_8\text{-LiTFSI-15\%TBPHP}$), the typical diffraction peaks of PEO became broader with a much lower intensity than that with only the LiTFSI, indicating that incorporating of IL TBPHP decreased the crystalline phase structure of PEO and resulted in the formation more amorphous phases [41]. It is reported that the embracing of large cations by the $-\text{CH}_2\text{CH}_2\text{OCH}_2-$ polymeric segments of PEO can result in the trans-conformation and expansion of PEO [35]. For example, in the presence of IL $\text{N}_{4111}\text{TFSI}$, the $-\text{CH}_2\text{CH}_2\text{OCH}_2-$ polymeric segments of PEO can embrace the cation of IL to affect the fluid dynamics [36]. In this work, the PEO could also embrace the cation of IL TBPHP with the similar structure as the IL $\text{N}_{4111}\text{TFSI}$. Meanwhile, the anion of IL TBPHP should be also distributed along the PEO chain to form an interconnected "linear comb" in order to maintain the electro-neutrality, which could restrain PEO crystallization. As for the final

SPE (PEO₈-LiTFSI-TBHP-12.5%LLZTO), the crystalline peaks of PEO almost disappeared although all diffraction peaks of LLZTO powder, which matched well with the standard XRD pattern of the known the cubic garnet-type structure Li₅La₃Nb₂O₁₂ (JCPDS: 45-0109), had no any changes.

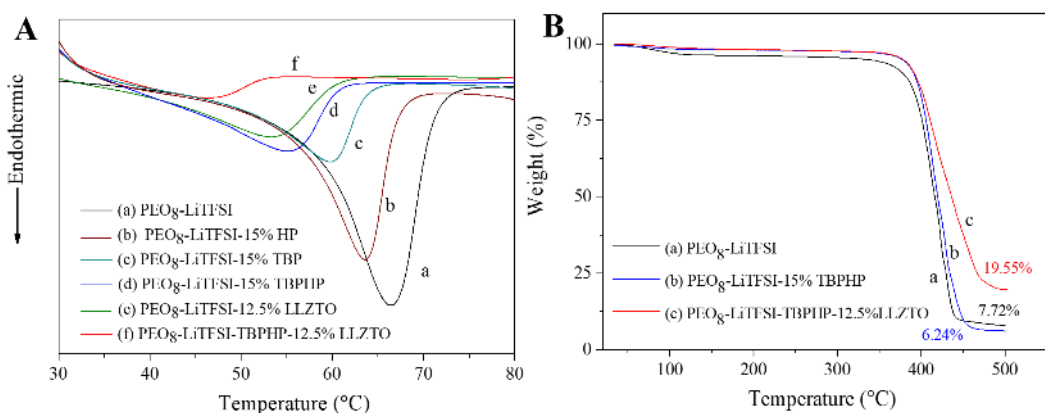


Fig. 3.3 (A) DSC and (B) TGA curves of the prepared SPEs.

It is reported that the chains in the PEO matrix can transport Li⁺ ions through irregular segmental motions, which could be promoted with the increase in amorphous regions [12, 13]. As shown in **Fig. 3A**, the endothermic peaks at 66.5, 55.2 and 47.1°C in the DSC curves of the neat PEO₈-LiTFSI, PEO₈-LiTFSI-15%TBPHP and PEO₈-LiTFSI-TBPHP-12.5%LLZTO SPEs, respectively, corresponded to the melting temperatures (T_m) of them. One can see that the T_m of SPE shifted to the lower temperature with a significant decrease of the peak intensity as the TBPHP or LLZTO was incorporated. Meanwhile, the calculated crystallinity values (χ_c) were 64.10%, 35.23%, and 10.80% for the neat PEO₈-LiTFSI, PEO₈-LiTFSI-15%TBPHP and PEO₈-LiTFSI-TBPHP-12.5%LLZTO SPEs, respectively. As stated above, the TBP⁺ cation in TBPHP played a plasticizing role to increase the amorphous phase in the SPEs and simultaneously, the ceramic filler also affected the crystallization rate of polymer matrix by preventing the agglomeration of the polymer chains and decreasing the rate of the recrystallization processes of the polymer host

to increase the amorphous phase [39, 41]. As a result, the segmental motion of the polymer network was enhanced to facilitate the movement of ions. To understand the effect of cation and anion in TBPHP comprehensively, the T_m values of PEO₈-LiTFSI-15% TBP and PEO₈-LiTFSI-15% HP were also measured, which were 59.7 °C and 63.6 °C respectively (**Fig. 3.3A**), and the calculated crystallinity values (χ_c) were 36.04% and 52.88% for the PEO₈-LiTFSI-15% TBPHP and PEO₈-LiTFSI-15% HP SPEs, respectively. These indicate that the main change of PEO crystallinity was caused by the incorporation of TBP cation in PEO₈-LiTFSI-15% TBPHP electrolyte. This result is consistent with the previous study [32]. Moreover, it is found that the cation TBP-based compound had a rich phase behavior in the solid state, which could also affect the performance of SPEs [32, 42]. Furthermore, it should be noted that the anions of TFSI⁻ could be trapped by TBP⁺, which will be beneficial for the ion transportation, meanwhile, the chemical and mechanical interactions between ceramic particles (LLZTO) and the polymer matrix could result in the decrease of PEO crystallinity [38, 40, 43]. Therefore, in this study, the synergistic effect of the TBPHP and ceramic electrolyte LLZTO resulted in the faster Li⁺ ions transportation in the PEO₈-LiTFSI-TBPHP-12.5%LLZTO SPE.

The thermal stability of the electrolyte was evaluated by thermogravimetric analysis (TGA). As shown in **Figs. 3.3B**, according to the thermogravimetric derivative results, the weights of all SPEs maintained almost unchanged until a temperature of about 330 °C. The PEO₈-LiTFSI started to decompose at 331.1 °C. However, with the addition of TBPHP, the PEO₈-LiTFSI-15%TBPHP remained stable until 368 °C, and with the co-addition of LLZTO, the PEO₈-LiTFSI-TBPHP-12.5%LLZTO showed the highest thermal stability with an initial decomposition temperature of 377 °C. These results indicated that the addition of TBPHP effectively improved the stability of SPEs. Herein, due to the decrease in PEO crystallinity and evaporation of the ionic liquid at a temperature as high as 500 °C, the mass loss of PEO₈-LiTFSI-15%TBPHP was a little higher than

the case without the TBPHP addition [44]. In contrast, the mass loss decreased to a great extent as the LLZTO filler was introduced since the LLZTO is stable even at a high temperature. Besides, the LLZTO filler could act as a barrier between the electrode and electrolyte to ensure safety even in extreme operation conditions.

3.3.2 Electrochemical stability window and ionic conductivity

The electrochemical window of the SPEs is a crucial parameter for achieving high-energy density in the high-voltage LMBs. As can be seen from **Fig. 3.4**, compared to the neat PEO₈-LiTFSI SPE membrane, the electrochemical windows of PEO₈-LiTFSI-15%TBPHP and PEO₈-LiTFSI-TBPHP-12.5%LLZTO were stable until the voltages increased up to 4.5 V and 5.0 V versus Li/Li⁺, respectively. Herein, the excellent electrochemical stability should be attributed to the superior oxidative stability of TBPHP, LLZTO and its surface passivation layer [40, 43]. These results indicate that the obtained SPEs worked well with a high-voltage cathode in LMBs.

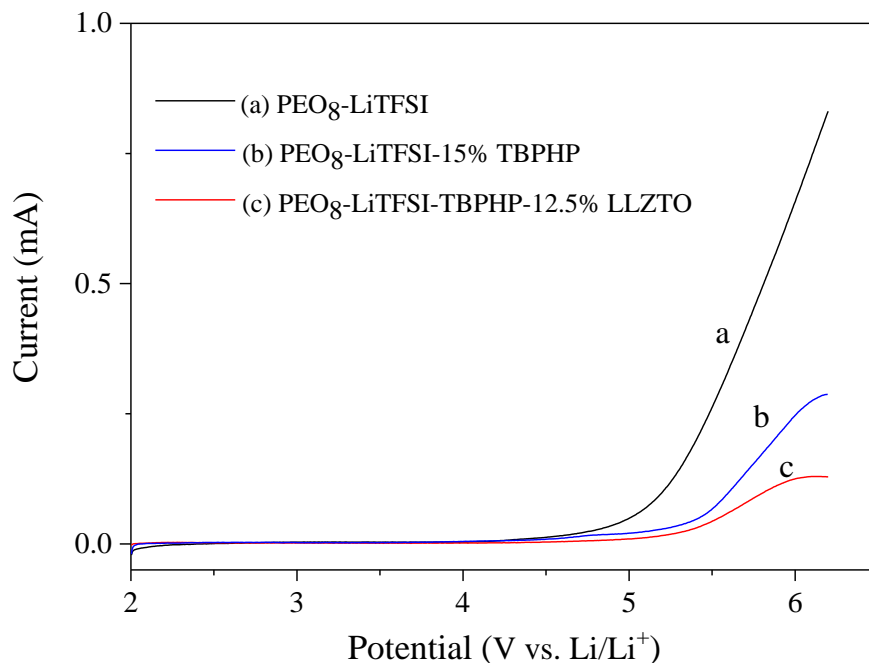


Fig. 3.4. Linear sweep voltammetry (LSV) curves of the prepared SPEs with the electrochemical stability window in the range of 2.0-6.2 V.

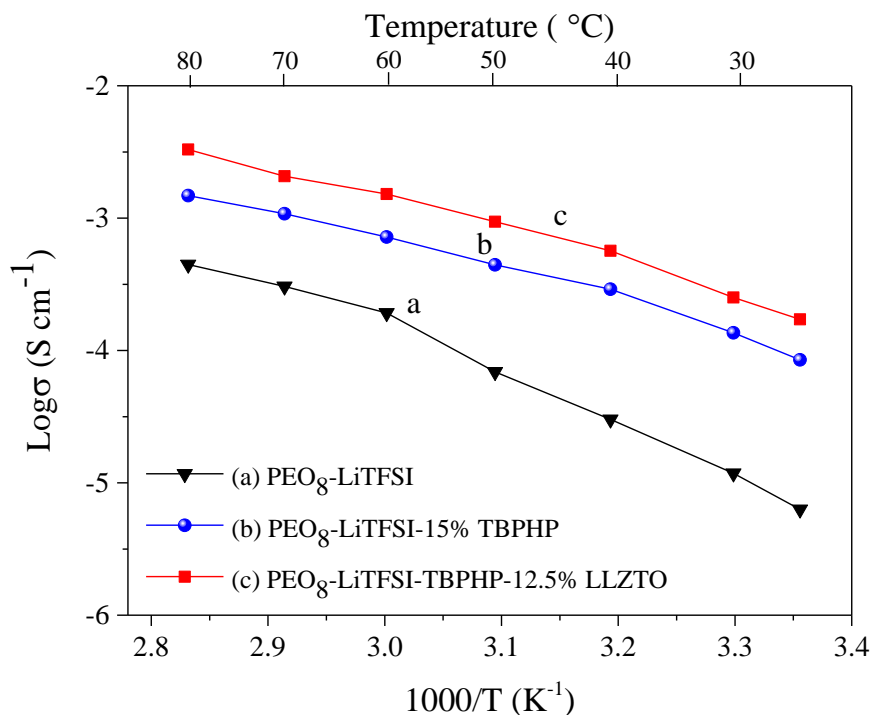


Fig. 3.5 Ionic conductivities of SPEs vs. temperature in the range of 25-80 °C.

The ionic conductivity of SPE is mainly featured by either cation or vacancy conduction properties [43]. **Fig. 3.5** shows the ionic conductivities of the prepared PEO₈-LiTFSI, PEO₈-LiTFSI-15%TBPHP and PEO₈-LiTFSI-TBPHP-12.5%LLZTO SPE membranes at a temperature range of 25-80 °C. One can see that the PEO₈-LiTFSI-15%TBPHP exhibited a preferable ionic conductivity of $1.36 \times 10^{-4} \text{ S} \cdot \text{cm}^{-1}$ and $4.43 \times 10^{-4} \text{ S} \cdot \text{cm}^{-1}$ at 30 °C and 50 °C, respectively, which were approximately 10 times higher than those of TBPHP-free PEO₈-LiTFSI SPEs. After the addition of TBPHP, the crystallinity of PEO was reduced, which promoted the segmental motion of polymer chains in PEO, resulting in a higher ion transportation ability. Comparing to other PEO based SPEs with the inert fillers such as Al₂O₃ ($1.0 \times 10^{-6} \text{ S} \cdot \text{cm}^{-1}$ at room temperature) [45] and IL of N-methyl-N-propylpiperdinium bis(fluorosulfonyl)imide (PP₁₃FSI) ($6.45 \times 10^{-5} \text{ S} \cdot \text{cm}^{-1}$ at room temperature) [46], the PEO₈-LiTFSI-15%TBPHP exhibited a much higher ionic conductivity. Moreover, the ionic conductivity was further enhanced by the incorporation of the ceramic

electrolyte LLZTO. That is, the PEO₈-LiTFSI-TBPHP-12.5% LLZTO showed a superior ionic conductivity of $2.51 \times 10^{-4} \text{ S}\cdot\text{cm}^{-1}$ at 30 °C and up to as high as $9.39 \times 10^{-4} \text{ S}\cdot\text{cm}^{-1}$ at 50 °C, which approached a value of $1 \times 10^{-3} \text{ S}\cdot\text{cm}^{-1}$ as some of the liquid electrolytes. The notable improvement in ionic conductivity of SPEs at both room and elevated temperatures should be resulted from the multiple ion conducting channels consisting of the polymer segments, LLZTO crystals, and heterogeneous interfaces existed in PEO₈-LiTFSI-TBPHP-12.5% LLZTO SPEs.

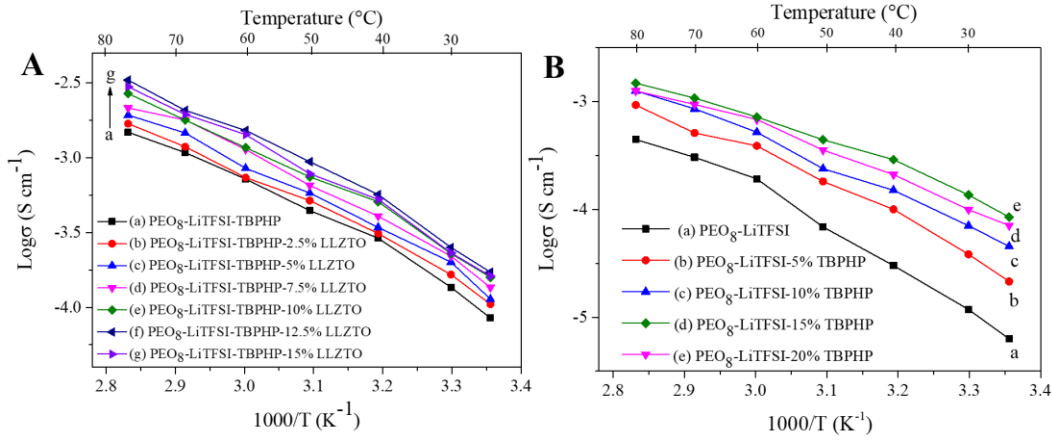


Fig. 3.6 Ionic conductivities of the PEO₈-LiTFSI based composite electrolytes as a function of the weight percentages of (A) IL TBPHP and (B) TBPHP and ceramics filler LLZTO at different temperatures.

The ionic conductivities of the prepared SPEs with different compositions are shown in **Fig. 3.6**. One can see that the ionic conductivity decreased by adding of excessive TBPHP or LLZTO. It is possible that the excessive additives could decrease the interface contact, increase the interface impedance in the composite SPEs [40, 47]. In addition, based on the potentiostatic coulometry measurements at 50 °C, the electronic conductivities of PEO₈-LiTFSI, PEO₈-LiTFSI-15%TBPHP, and PEO₈-LiTFSI-TBPHP-12.5% LLZTO SPEs are $3.980 \times 10^{-8} \text{ S cm}^{-1}$, $5.672 \times 10^{-8} \text{ S cm}^{-1}$, $4.83 \times 10^{-8} \text{ S cm}^{-1}$, respectively. Therefore, the ionic conductivity of them plays the main role in the entire conductivity apparently. Lastly, taking the ionic conductivity and discharged capacity into

account, 50 °C was chosen as the optimum operating temperature of LMBs.

3.3.3 Li⁺ ion transference number

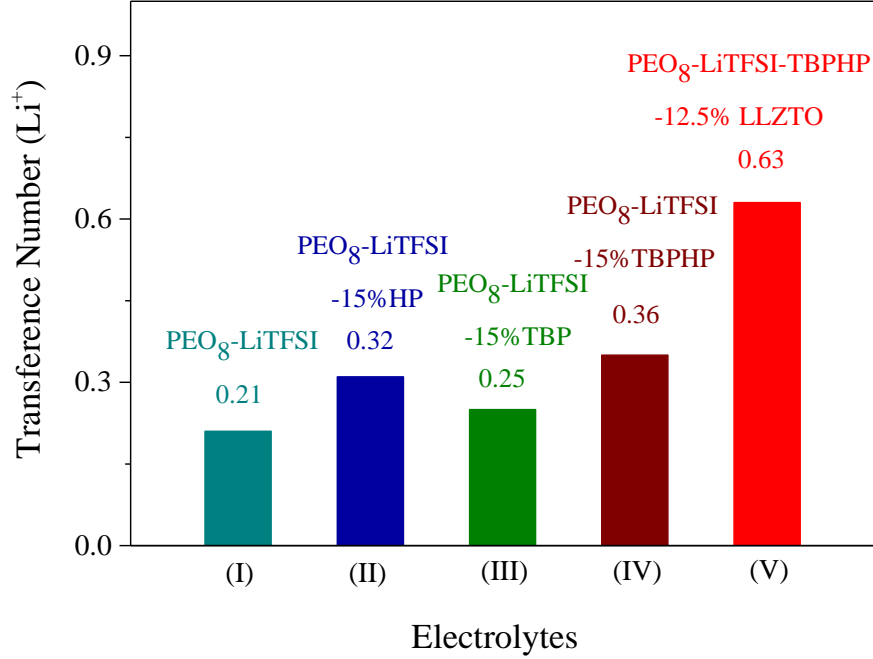


Fig. 3.7 Lithium-ion transference numbers of the prepared SPEs.

Lithium-ion transference number t_{Li^+} is an essential parameter to evaluate the performance of prepared SPEs. There were four ionic species, i.e., Li⁺, TBP⁺, HP⁻ and TFSI⁻, in the SPEs after TBPHP incorporation. Among them, the specific contribution of Li⁺ ions in this ionic conductivity based on t_{Li^+} should be more important. In this study, the t_{Li^+} was investigated by a combined AC/DC technique as described in the experimental section and the value of t_{Li^+} was calculated by equation (2). As shown in **Fig. 3.7**, the t_{Li^+} of the PEO₈-LiTFSI-15% TBPHP SPE was approximately 0.36, which was comparable to those of commercial electrolytes (t_{Li^+} =0.2-0.5), and suitable for the battery application [14, 48]. Moreover, compared with the t_{Li^+} values of PEO₈-LiTFSI (0.21), PEO₈-LiTFSI-12.5% LLZTO (0.43), PEO-LiTFSI-20% LLZTO (0.38) and PEO-0.5 LLZTO (0.2) [43, 49], TBPHP should also contribute to the high t_{Li^+} like the garnet-type

structure electrolyte LLZTO. Herein, to investigate the effect of TBPHP addition in more details, orthogonal experiments were designed and conducted. As a result, the t_{Li^+} values of PEO₈-LiTFSI-15% TBP and PEO₈-LiTFSI-15% HP were 0.25 and 0.32, respectively, demonstrating that the anion HP⁻ had great influence on the increase of t_{Li^+} . Herein, HP⁻ anions was resulted from 2-HP reaction with LiOH. It is possible that the electronegative atom (N and O) located on anion HP⁻ could be coordinated with Li⁺ ions easily, facilitating the dissociation of lithium salt. Some researchers considered that the coordination with Li⁺ ions can reduce the tendency of free mobile anions moving to the opposite direction of cations, weakening the barrier for the cation transportation [43]. Furthermore, as indicated above, due to the plasticization effect, TBP⁺ could effectively inhibit the crystallinity of PEO. Hence, benefited from the individual and synergistic effects of TBP⁺ cation and HP⁻ anion in TBPHP, the lithium ion transfer was accelerated. As a result, the PEO₈-LiTFSI-15% TBPHP SPE membrane had a higher t_{Li^+} . Furthermore, with the introduction of ceramic filler LLZTO, the Li transference number could be enhanced more since the LLZTO itself had a high t_{Li^+} (~1) [38]. As a result, the PEO₈-LiTFSI-TBPHP-12.5% LLZTO exhibited a t_{Li^+} as high as 0.63.

3.3.4 DFT theoretical calculations

To understand the synergistic effects and the behaviors of cations (Li⁺ and TBP⁺) and anions (TFSI⁻ and HP⁻) in SPE, DFT theoretical calculations of the chemical bonding ability were performed. In general, the negative value of binding energy indicates the stability after the interaction [50]. Based on the calculation results, the binding energies between cations and anions were -0.1458, -0.1031, -0.2023, and -0.2787 Ha for TBPHP, TBPTFSI, LiTFSI, and LiHP, respectively. Compared $E_b(\text{TBPHP})$ with $E_b(\text{LiTFSI})$ and $E_b(\text{LiHP})$, it can be concluded that the anion HP⁻ coordinated with Li⁺ ions more strongly in SPE. As such, the dissociation of lithium salt of LiTFSI was facilitated while the Li⁺ ion number donated by the ceramics electrolyte was increased [15] so

that the hybrid SPE, i.e., PEO₈-LiTFSI-TBPHP-12.5% LLZTO, exhibited the highest t_{Li^+} (0.63). Meanwhile, compared $E_b(TBPTFSI)$ with $E_b(LiTFSI)$, a strong interaction between repeating units in the PEO chain and TBP⁺ cations in TBPHP was found, which resulted in a significant crystallinity decrease in the polymer. This is beneficial for the ion transport in PEO [1]. In addition, the DSC results in **Fig.3** were also agreement with these DFT calculations.

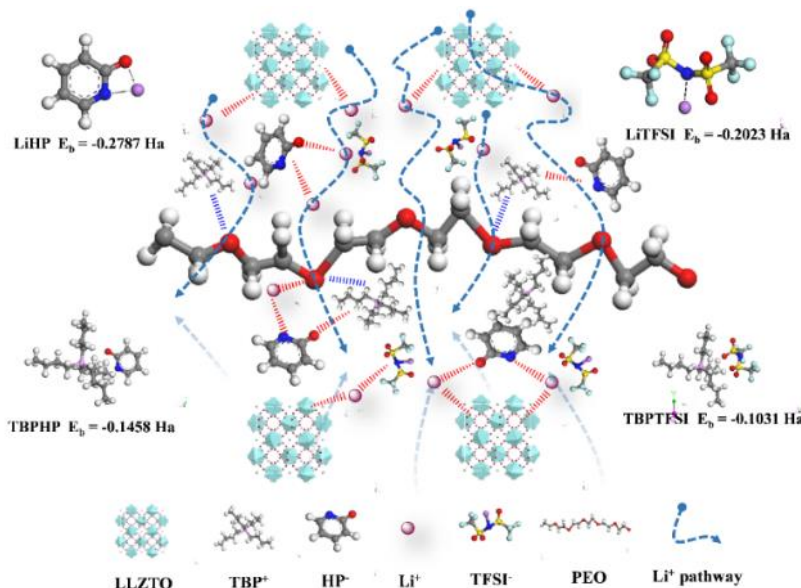


Fig. 3.8 A proposed ionic transport behavior in the PEO₈-LiTFSI-TBPHP-12.5% LLZTO SPE complex structure.

According to the results mentioned above, a proposed ionic transport mechanism in PEO₈-LiTFSI-TBPHP-12.5% LLZTO complex structure can be presented in **Fig. 3.8** based on previous reports [11, 15].

3.3.5 Rate performance and cycle stability

To verify the applicability of the PEO-TBPHP-LLZTO SPEs in the LMBs, quasi-solid-state LiFePO₄|Li batteries with the PEO₈-LiTFSI, PEO₈-LiTFSI-15%TBPHP, and PEO₈-LiTFSI-TBPHP-12.5%LLZTO SPEs were assembled individually. The initial charge-discharge profiles of the LiFePO₄| PEO₈-LiTFSI-15% TBPHP | Li and LiFePO₄| PEO₈-LiTFSI-TBPHP-12.5% LLZTO

| Li at 50 °C with different rates are shown in **Fig. 3.9A** and **3.9B**. The LiFePO₄|Li cell with the PEO₈-LiTFSI-15% TBPHP SPE membrane in a voltage range of 2.8-4.0 V delivered a high discharge capacity of 136.2 mAh g⁻¹ at 0.1 C, which reached 80.1 % of the theoretical value. Even though the plateau region was hard to be observed in the initial charge-discharge profiles, the LiFePO₄|Li cell still offered high discharge capacities of 129.7, 113.7, 80.7 and 64.9 mAh g⁻¹ at rates of 0.2, 0.5, 1 and 2 C, respectively. The observed rate performance was much higher than that of the similar battery systems in the previous studies, especially with the large current density [51, 52]. As shown in **Fig. 3.9C**, after the end of cycling at 2 C, the discharge capacity was recovered to 131.5 mAh g⁻¹ as the rate returned to 0.1 C, reaching 96.5% of the initial discharge capacity. These types of voltage profiles could be resulted from the high polarization of SPEs as the similar reported results [51, 53]. Furthermore, due to the excellent mechanical and electrochemical properties, the LiFePO₄ |PEO₈-LiTFSI-TBPHP-12.5% LLZTO| Li battery exhibited a clear potential plateau in a voltage range of 2.9-3.8 V at 50 °C (**Fig. 3.9B**), indicating a good reversible cycling property with the specific capacities of approximately 153.1, 149.6, 142.8, 115.3 and 93.7 mAh g⁻¹ at 0.1, 0.2, 0.5, 1 and 2 C, respectively. After the end of further cycling at a high rate of 2 C, the discharge capacity was still boosted to 152.7 mAh g⁻¹ when the rate returned to 0.1 C, even reaching 99.7% of the initial discharge capacity.

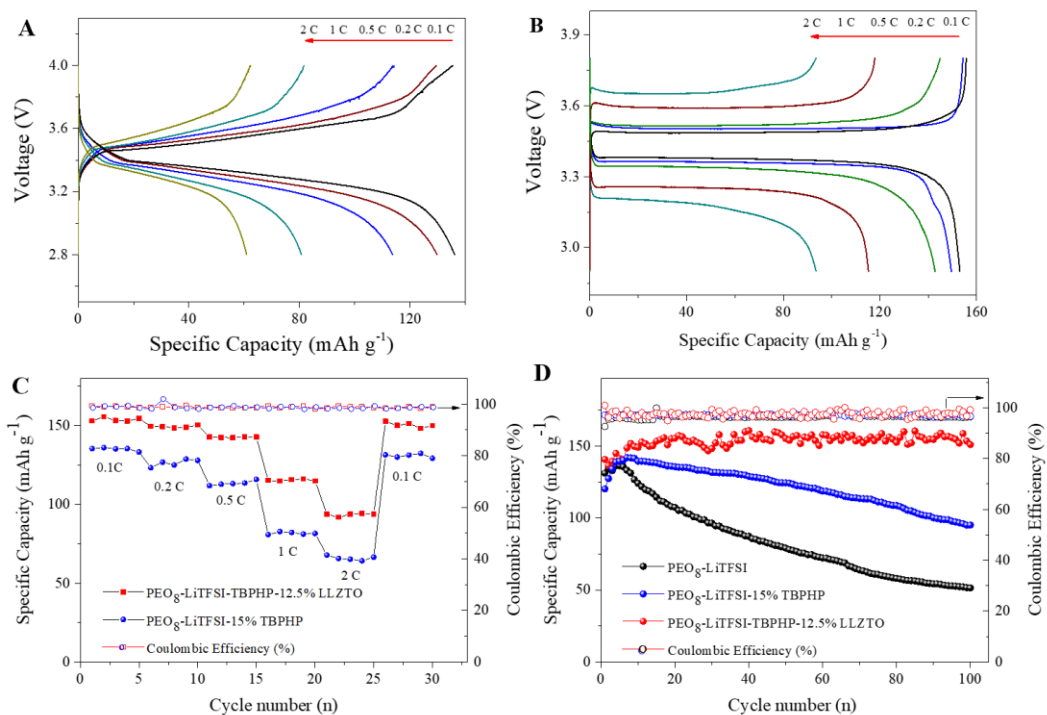


Fig. 3.9 Typical charge-discharge voltage profiles of LiFePO₄|Li cells based on (A) PEO₈-LiTFSI-15wt% TBPHP and (B) PEO₈-LiTFSI-TBPHP-12.5% LLZTO SPEs at 50 °C with various rates; (C) Rate performance of the quasi-solid-state LiFePO₄|Li cells with the PEO₈-LiTFSI-15 wt% TBPHP and PEO₈-LiTFSI-TBPHP-12.5% LLZTO SPEs at 50 °C; (D) Cycling stability of the LiFePO₄|Li cells with different SPEs at 0.2 C and 50 °C.

Cycle performances of the quasi-solid-state-LMBs were also evaluated with a high rate of 0.2 C at 50 °C. As shown in **Fig. 3.9D**, lower discharge capacities were obviously observed in the first few cycles. It should be attributed to the structural reorganization of the electrodes as well as the electrolyte and the formation of new electrolyte/electrode interfaces. In general, the electrolyte species could infiltrate into the electrode structure in the initial few cycles, also resulting in the low discharge capacity [48, 54]. The discharge capacity of the LiFePO₄|Li cell with the PEO₈-LiTFSI SPE membrane in the voltage range of 2.8-4.0 V exhibited a rapid decay from 131.1 to 51.4 mAh g⁻¹ within 100 cycles.

In contrast, the $\text{LiFePO}_4|\text{Li}$ cell with the $\text{PEO}_8\text{-LiTFSI-15\% TBPHP}$ SPE showed higher cycling stability with a discharge capacity of 95.1 mAh g^{-1} after 100 cycles, indicating enhanced cycling stability in comparison with the TBPHP-free electrolyte. As indicated above, this superior cycling stability should be also attributed to the existing of more stable electrolyte/anode interface, higher t_{Li^+} , lower crystallinity of polymer matrix PEO and lower interfacial impedance with the interlayers wetted by the IL TBPHP. As described in the section of DFT calculations, the anion HP^- can coordinate with Li^+ ions more strongly in electrolyte. In this case, based on the space-charge theory related to the nonaqueous electrolytes, when Li ions travel close to the anode side, the ion transport is mainly driven by the electric field since more HP^- existed there, which can adjust the Li^+ distribution well. Moreover, it is reported that a portion of immobilized anions could contribute to the stable electrodeposition in the anode and increase the cell lifetime. Thus, the existence of HP^- could also play the same role to form the more stable electrolyte/anode interface during the lithium plating/stripping process [43, 55, 56].

Interestingly, the quasi-solid-state $\text{LiFePO}_4|\text{Li}$ cell with the $\text{PEO}_8\text{-LiTFSI-TBPHP-12.5\% LLZTO}$ SPE membrane still possessed a high discharge capacity 151 mAh g^{-1} with a coulombic efficiency of 99.2 % even after 100 cycles, nearly 88.8% of the theoretical value. In contrast, the solid-state $\text{LiFePO}_4|\text{Li}$ cell with the $\text{PEO}_8\text{-LiTFSI-12.5\% LLZTO}$ SPE membrane only rendered a discharge capacity 123.8 mAh g^{-1} after 60 cycles with the same condition. These results together with **Table 3.1** indicate that this strategy is attractive to enhance the discharge capacity as well as the cycling stability by incorporating the TBPHP and LLZTO ceramic filler.

Table 3.1 Comparison of PEO-based polymer electrolytes for Li metal cells.

SPEs	Cathode	Discharge Capacity (mAh g ⁻¹)	T (°C)	Cycles	Ref
PEO-LiTFSI-LLZTO	LiFePO ₄	139.10 (0.2 C)	55	100	[38]
PEO-LiTFSI-LLZTO (Al-doped) ^a	LiFePO ₄	134.85 (0.1 C)	60	100	[43]
PEO/LiClO ₄ -LLZTO	LiFePO ₄	140 (1 C)	60	100	[49]
PEO-LiTFSI-LLZTO	LiFePO ₄	127.35 (0.1 C)	60	200	[40]
PEO/LLZTO@BT ^b	LiFePO ₄	121 (0.5 C)	25	150	[57]
PEO-LiTFSI-60% LLZTO-10% SN ^c	LiFePO ₄	151.1 (0.5 C)	60	200	[58]
PIL-LiTFSI-LATP ^d	LiFePO ₄	141.3 (1.0 C)	60	250	[59]
POSS-PrMIM ^e	LiFePO ₄	128 (0.1 C)	22	56	[52]
PEO-LiTFSI-LC-IL ^f	LiFePO ₄	150 (0.2 C)	30	80	[60]
PEO ₈ -LiTFSI-15% TBPHP		95.1 (0.2 C)			
PEO ₈ -LiTFSI-TBPHP-12.5% LLZTO	LiFePO ₄	151 (0.2 C)	50	100	This Work

^a: Al-doped Li_{6.75}La₃Zr_{1.75}Ta_{0.25}O₁₂ (LLZTO); ^b: 1-Butyl-3-methylimidazolium bis(trifluoromethanesulfonyl)imide (BT ionic liquid); ^c: Succinonitrile (SN); ^d: 1-vinyl-3-ethylimidazolium bis(trifluoromethanesulfonyl)imide ionic liquid (PIL)- Li_{1.3}Al_{0.3}Ti_{1.7}(PO₄)₃; ^e: polyhedral oligomeric silsesquioxane ionic liquids; ^f: 1,4-bis(4-(60-acryloxy-hexyloxy) benzoyloxy)-2-toluene (LC), (1-ethyl-3-methylimidazolium bis(trifluoromethylsulfonyl)imide) (IL).

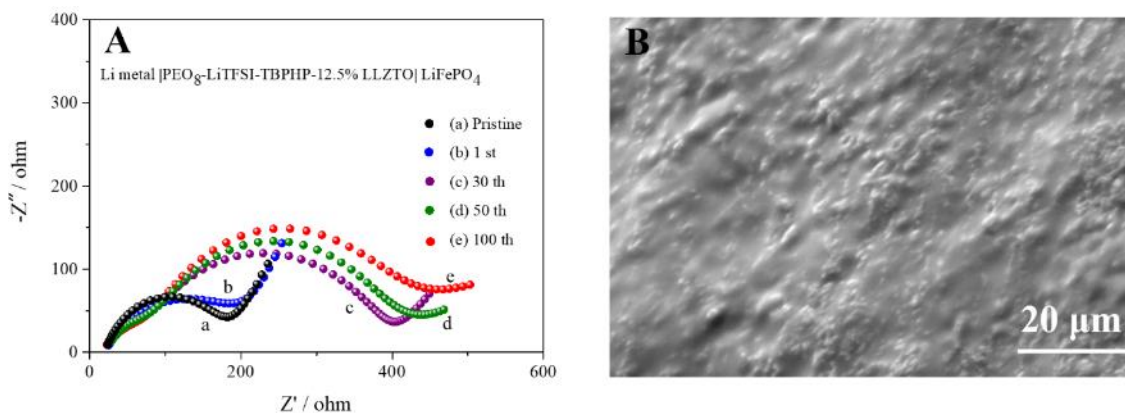


Fig. 3.10 (A) AC impedance changes of the quasi-solid state LiFePO₄ | PEO₈-LiTFSI-TBPHP-12.5% LLZTO | Li coin cell after different cycles at 0.2 C and 50 °C; (B) SEM image of surface

morphology for this SPE membrane after 100 cycles test.

AC impedance changes of the quasi-solid-state $\text{LiFePO}_4|\text{PEO}_8\text{-LiTFSI-TBPHP-12.5\% LLZTO}|$ Li coin cell after different cycles at 0.2 C and 50 °C are shown in **Fig. 3.10A**. The resistances of the above cell increased to 344, 369 and 405 Ω after 30, 50 and 100 cycles, respectively. The tiny resistance change indicated the excellent interfacial compatibility between the materials. Furthermore, the SEM image of $\text{PEO}_8\text{-LiTFSI-TBPHP-12.5\% LLZTO}$ SPE membrane surface after 100 cycles test is shown in **Fig. 3.10B**. One can see that no significant morphology change after 100 cycles was observed, which also supported its excellent stability. Besides, **Fig. 3.11** shows the surface morphologies of the Li metal anodes in the $\text{LiFePO}_4|\text{Li}$ cells with different electrolytes after 100 cycles test. Compared with **Figs. 3.11 C and D**, it is found that the lithium metal surface (**Fig. 3.11B**) with the $\text{PEO}_8\text{-LiTFSI-TBPHP-12.5\% LLZTO}$ SPE after the cycling test showed only some cracks during the lithium plating/stripping process owing to the volume expansion, indicating a more stable electrolyte/anode interface to decrease the formation of Li dendrites.

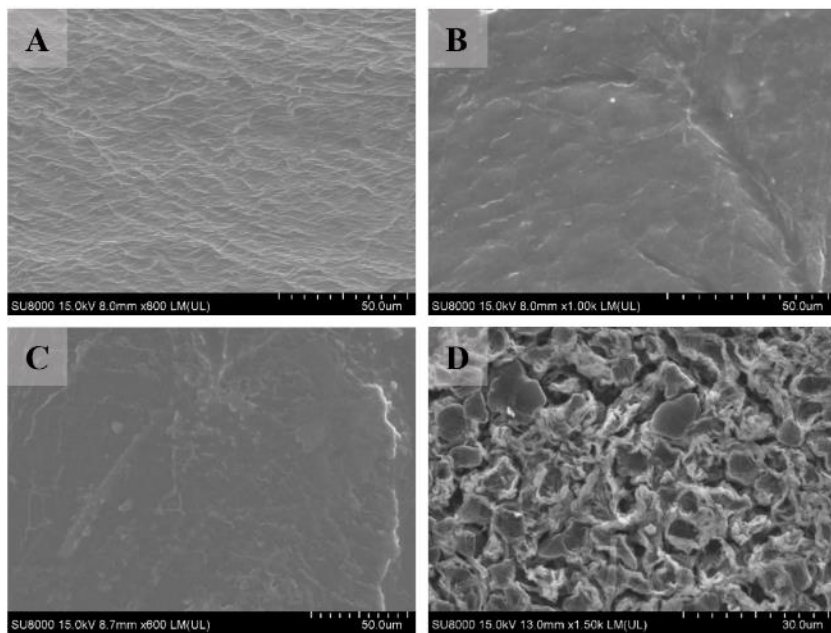


Fig. 3.11 SEM images of (A) the pristine Li metal electrode; and the Li anode surfaces obtained

from the $\text{LiFePO}_4|\text{Li}$ cell with **(B)** $\text{PEO}_8\text{-LiTFSI-TBPHP-12.5 \% LLZTO}$, **(C)** $\text{PEO}_8\text{-LiTFSI}$, and **(D)** routine $\text{LiTFSI}/(\text{DOL}+\text{DME}, 1: 1 \text{ in volume})$ after cycles at 0.2 C.

The long-term mechanical stability of $\text{PEO}_8\text{-LiTFSI-TBPHP-12.5\%LLZTO}$ SPE membrane against the Li dendrites was further evaluated by using a symmetrical $\text{Li}|\text{Li}$ cell, in which Li metal was plated and stripped time after time to mimic a practical cycling process. **Fig. 3.12** shows the voltage profiles of the cell cycled at the current densities of 0.1, 0.2 and 0.5 $\text{mA}\cdot\text{cm}^{-2}$, respectively. It is found that the symmetrical $\text{Li}|\text{Li}$ cell rendered outstanding cycling stability and low voltage polarization for more than 630 h without the short circuit, also implying that the $\text{PEO}_8\text{-LiTFSI-TBPHP-12.5\% LLZTO}$ SPE membrane effectively suppressed the lithium dendrites.

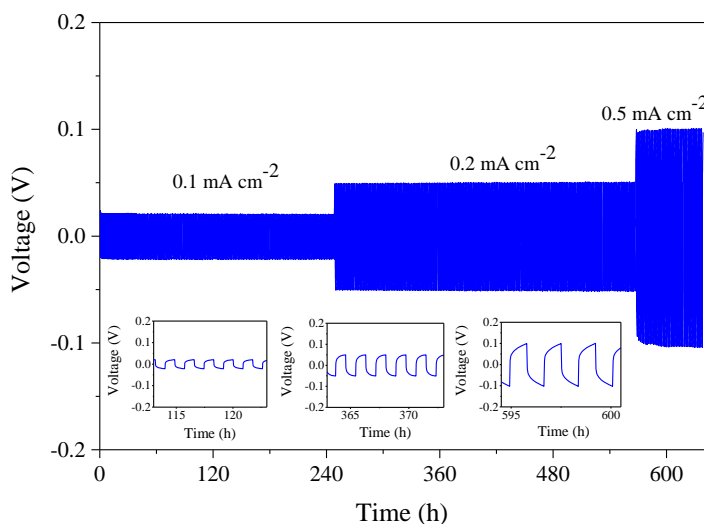


Fig. 3.12 Galvanostatic cycling curves of the $\text{Li}|\text{PEO}_8\text{-LiTFSI-TBPHP-12.5\% LLZTO}|\text{Li}$ symmetrical cells at different current densities at 50 °C. Insets show the enlarge view of cycling curves.

As shown in **Fig. 3.13**, a pouch cell with the $\text{PEO}_8\text{-LiTFSI-TBPHP-12.5\%LLZTO}$ SPE maintained the capability of lighting the LED device before and after several bending tests, indicating that it also satisfied the flexibility requirements. Moreover, no short circuit appeared

even after the pouch cell was cut, indicating good contact between the SPE membrane and electrodes. Therefore, the PEO₈-LiTFSI-TBPHP-12.5% LLZTO SPE not only stabilized the Li metal anode, suppressed Li dendrite growth, and enhanced the safety of LMBs, but also had great potential to be applied in the flexible and wearable electronics.

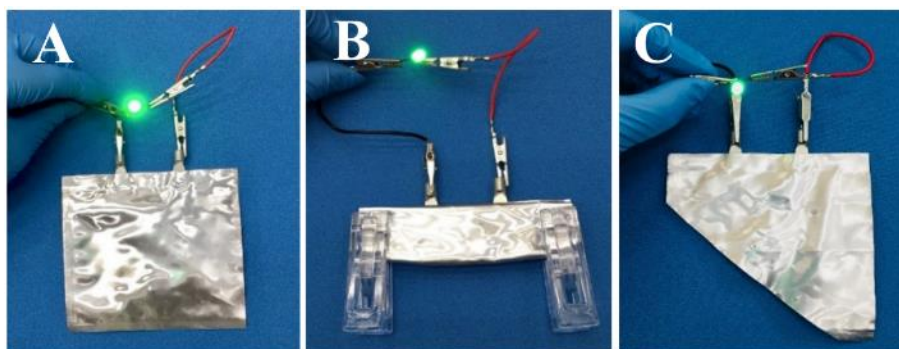


Fig. 3.13 Quasi-solid-state LiFePO₄ | PEO₈-LiTFSI-TBPHP-12.5%LLZTO | Li metal pouch cell assembled to light the LED at (A) flat states, and well-running under (B) folding and (C) a corner cutting at room temperature.

3.4 Conclusions

In summary, the PEO-lithium salt based flexible SPE membranes of PEO₈-LiTFSI-15% TBPHP and PEO₈-LiTFSI-TBPHP-12.5% LLZTO were successfully fabricated through a solvent-free procedure and applied in quasi-solid-state LMBs. Based on the experimental investigations and DFT calculations, the TBP⁺ cation and HP⁻ anion of TBPHP ionic liquid played significant roles in adjusting the crystallization of PEO and enhancing lithium-ion transference number of t_{Li^+} , respectively. Meanwhile, the addition of fast-ion conductor ceramic filler of the LLZTO further improved the performance of the battery in terms of ionic conductivity, rigid strength, thermal and electrochemical stability of SPEs. It is found that the crystallinity of PEO in SPE apparently reduced to guarantee the fast transport of Li⁺, improve the contact with the electrodes, reduce the interfacial resistance, and suppress the lithium dendrite growth for stabilizing the battery. As a

result, PEO₈-LiTFSI-TBPHP-12.5% LLZTO SPE revealed a satisfied ionic conductivity of $9.39 \times 10^{-4} \text{ S} \cdot \text{cm}^{-1}$, a wide electrochemical window of more than 5.0 V and a high t_{Li+} of 0.63 at 50 °C. Moreover, the quasi-solid-state LiFePO₄|Li battery assembled with the PEO₈-LiTFSI-TBPHP-12.5% LLZTO SPE exhibited excellent rate performance, coulombic efficiency and cycle stability with negligible discharge capacity decay in 100 cycles at 50 °C, indicating that it has a high potential to be applied in LMBs.

References

- [1] Z. Xue, D. He, X. Xie, Poly(ethylene oxide)-based electrolytes for lithium-ion batteries, *J. Mater. Chem. A* 3 (2015) 19218–19253.
- [2] Q. Yang, Z. Zhang, X.G. Sun, Y.S. Hu, H. Xing, S. Dai, Ionic liquids and derived materials for lithium and sodium batteries, *Chem. Soc. Rev.* 47 (2018) 2020–2064.
- [3] Z. Wu, Z. Xie, A. Yoshida, Z. Wang, X. Hao, A. Abudula, G. Guan, Utmost limits of various solid electrolytes in all-solid-state lithium batteries: A critical review, *Renewable Sustainable Energy Rev.* 109 (2019) 367–385.
- [4] Y. Seino, T. Ota, K. Takada, A. Hayashi, M. Tatsumisago, A sulphide lithium super ion conductor is superior to liquid ion conductors for use in rechargeable batteries *Energy Environ. Sci.* 7 (2014) 627–631.
- [5] T. Kobayashi, A. Yamada, R. Kanno, Interfacial reactions at electrode/electrolyte boundary in all solid-state lithium battery using inorganic solid electrolyte, thio-LISICON, *Electrochim. Acta* 53 (2008) 5045–5050.
- [6] N. Kamaya, K. Homma, Y. Yamakawa, M. Hirayama, R. Kanno, M. Yonemura, T. Kamiyama, Y. Kato, S. Hama, K. Kawamoto, A. Mitsui, A lithium superionic conductor, *Nat. Mater.* 10 (2011) 682–686.
- [7] Y. Shimonishi, T. Zhang, N. Imanishi, D. Im, D.J. Lee, A. Hirano, Y. Takeda, O. Yamamoto,

- N. Sammes, A study on lithium/air secondary batteries-Stability of the NASICON-type lithium ion conducting solid electrolyte in alkaline aqueous solutions, *J. Power Sources* 196 (2011) 5128–5132.
- [8] Q. Liu, Z. Geng, C. Han, Y. Fu, S. Li, Y. B. He, F. Kang, B. Li, Challenges and perspectives of garnet solid electrolytes for all solid-state lithium batteries, *J. Power Sources* 389 (2018) 120–134.
- [9] Z. Zhang, Y. Shao, B. Lotsch, Y.S. Hu, H. Li, J. Janek, L.F. Nazar, C.W. Nan, J. Maier, M. Armand, L. Chen, New horizons for inorganic solid state ion conductors, *Energy Environ. Sci.* 11 (2018) 1945–1976.
- [10] Q. Lu, J. Fang, J. Yang, G. Yan, S. Liu, J. Wang, A novel solid composite polymer electrolyte based on poly(ethylene oxide) segmented polysulfone copolymers for rechargeable lithium batteries, *J. Membr. Sci.* 425-426 (2013) 105-112.
- [11] O. Sheng, C. Jin, J. Luo, H. Yuan, H. Huang, Y. Gan, J. Zhang, Y. Xia, C. Liang, W. Zhang, X. Tao, $\text{Mg}_2\text{B}_2\text{O}_5$ nanowire enabled multifunctional solid-state electrolytes with high ionic conductivity, excellent mechanical properties, and flame-retardant performance, *Nano Lett.* 18 (2018) 3104–3112.
- [12] H. Li, M. Li, S.H. Siyal, M. Zhu, J.-L. Lan, G. Sui, Y. Yu, W. Zhong, X. Yang, A sandwich structure polymer/polymer-ceramics/polymer gel electrolytes for the safe, stable cycling of lithium metal batteries, *J. Membr. Sci.* 555 (2018) 169-176.
- [13] J. Zhang, J. Zhao, L. Yue, Q. Wang, J. Chai, Z. Liu, X. Zhou, H. Li, Y. Guo, G. Cui, L. Chen, Safety-reinforced poly(propylene carbonate)-based all-solid-state polymer electrolyte for ambient-temperature solid polymer lithium batteries, *Adv. Energy Mater.* 5 (2015) 1501082.
- [14] X.X. Zeng, Y.X. Yin, N.W. Li, W.C. Du, Y.G. Guo, L.J. Wan, Reshaping lithium plating/stripping behavior via bifunctional polymer electrolyte for room-temperature solid

- Li metal batteries, *J. Am. Chem. Soc.* 138 (2016) 15825–15828.
- [15] X. Zhang, T. Liu, S. Zhang, X. Huang, B. Xu, Y. Lin, B. Xu, L. Li, C.W. Nan, Y. Shen, Synergistic coupling between $\text{Li}_{6.75}\text{La}_3\text{Zr}_{1.75}\text{Ta}_{0.25}\text{O}_{12}$ and poly(vinylidene fluoride) induces high ionic conductivity, mechanical strength, and thermal stability of solid composite electrolytes, *J. Am. Chem. Soc.* 139 (2017) 13779–13785.
- [16] Q. Zhang, K. Liu, F. Ding, X. Liu, Recent advances in solid polymer electrolytes for lithium batteries, *Nano Res.* 10 (2017) 4139–4174.
- [17] J. Hu, W. Wang, B. Zhou, Y. Feng, X. Xie, Z. Xue, Poly (ethylene oxide)-based composite polymer electrolytes embedding with ionic bond modified nanoparticles for all-solid-state lithium-ion battery, *J. Membr. Sci.* 575 (2019) 200-208.
- [18] L. Yue, J. Ma, J. Zhang, J. Zhao, S. Dong, Z. Liu, G. Cui, L. Chen, All solid-state polymer electrolytes for high-performance lithium ion batteries, *Energy Storage Mater.* 5 (2016) 139–164.
- [19] J. Shi, Y. Yang, H. Shao, Co-polymerization and blending based PEO/PMMA/P (VDF-HFP) gel polymer electrolyte for rechargeable lithium metal batteries, *J. Membr. Sci.* 547 (2018) 1-10.
- [20] I. Osada, H. De Vries, B. Scrosati, S. Passerini, Ionic-liquid-based polymer electrolytes for battery applications, *Angew. Chem. Int. Ed.* 55 (2016) 500–513.
- [21] V.A. Kusuma, M.K. Macala, J. Liu, A.M. Marti, R.J. Hirsch, L.J. Hill, D. Hopkinson, Ionic liquid compatibility in polyethylene oxide/siloxane ion gel membranes, *J. Membr. Sci.* 545 (2018) 292-300.
- [22] Y. Kumar, S.A. Hashmi, G.P. Pandey, Lithium ion transport and ion-polymer interaction in PEO based polymer electrolyte plasticized with ionic liquid, *Solid State Ionics* 201 (2011) 73-80.

- [23] G. Annat, J. Adebahr, I.R. McKinnon, D.R. MacFarlane, M. Forsyth, Plastic crystal behaviour in tetraethylammonium dicyanamide, *Solid State Ionics* 178 (2007) 1065–1071.
- [24] N. Chen, Y. Xing, L. Wang, F. Liu, L. Li, R. Chen, F. Wu, S. Guo, “Tai Chi” philosophy driven rigid-flexible hybrid ionogel electrolyte for high-performance lithium battery, *Nano Energy* 47 (2018) 35–42.
- [25] M.L. Thomas, Y. Oda, R. Tatara, H.M. Kwon, K. Ueno, K. Dokko, M. Watanabe, Suppression of water absorption by molecular design of ionic liquid electrolyte for Li–air battery, *Adv. Energy Mater.* 7 (2017) 1601753.
- [26] K. Yoshida, M. Nakamura, Y. Kazue, N. Tachikawa, S. Tsuzuki, S. Seki, K. Dokko, M. Watanabe, Oxidative-stability enhancement and charge transport mechanism in glyme-lithium salt equimolar complexes, *J. Am. Chem. Soc.* 133 (2011) 13121–13129.
- [27] K. Shikinaka, N. Taki, K. Kaneda, Y. Tominaga, Quasi-solid electrolyte: a thixotropic gel of imogolite and an ionic liquid, *Chem. Commun.* 53 (2017) 613–616.
- [28] C. Reitz, B. Breitung, A. Schneider, D. Wang, M. Von Der Lehr, T. Leichtweiss, J. Janek, H. Hahn, T. Brezesinski, Hierarchical carbon with high nitrogen doping level: a versatile anode and cathode host material for long-life lithium-ion and lithium-sulfur batteries, *ACS Appl. Mater. Interfaces* 8 (2016) 10274–10282.
- [29] Z. Liu, A. Prowald, S. Zein El Abedin, F. Endres, Template-assisted electrodeposition of highly ordered macroporous zinc structures from an ionic liquid, *J. Solid State Electrochem.* 17 (2013) 1185–1188.
- [30] G. A. Elia, J. Hassoun, B. Scrosati, F. Mueller, D. Bresser, S. Passerini, P. Oberhumer, N. Tsiouvaras, J. Reiter, An advanced lithium–air battery exploiting an ionic liquid-based electrolyte, *Nano Lett.* 14 (2014) 6572–6577.
- [31] W.A. Henderson, F. McKenna, M.A. Khan, N.R. Brooks, V.G. Young, R. Frech, Glyme-

- lithium bis (trifluoromethanesulfonyl) imide and glyme-lithium Bis (perfluoroethanesulfonyl) imide phase behavior and solvate structures, *Chem. Mater.* 17 (2005) 2284–2289.
- [32] X. An, X. Du, D. Duan, L. Shi, X. Hao, H. Lu, G. Guan, C. Peng, An absorption mechanism and polarity-induced viscosity model for CO₂ capture using hydroxypyridine-based ionic liquids, *Phys. Chem. Chem. Phys.* 19 (2017) 1134–1142.
- [33] G.K. Kline, J.R. Weidman, Q. Zhang, R. Guo, Studies of the synergistic effects of crosslink density and crosslink inhomogeneity on crosslinked PEO membranes for CO₂-selective separations, *J. Membr. Sci.* 544 (2017) 25–34.
- [34] S.L. Liu, L. Shao, M.L. Chua, C.H. Lau, H. Wang, S. Quan, Recent progress in the design of advanced PEO-containing membranes for CO₂ removal, *Prog. Polym. Sci.* 38 (2013) 1089–1120.
- [35] L.T. Costa, M.C.C. Ribeiro, Molecular dynamics simulation of polymer electrolytes based on poly(ethylene oxide) and ionic liquids. I. Structural properties, *J. Chem. Phys.* 124 (2006) 184902.
- [36] L.F. Lepre, L. Pison, L.J.A. Siqueira, R.A. Ando, M.F.C. Gomes, Improvement of carbon dioxide absorption by mixing poly(ethylene glycol) dimethyl ether with ammonium-based ionic liquids, *Sep. Purif. Technol.*, 196 (2018) 10–19.
- [37] Y. Jin, K. Liu, J. Lang, D. Zhuo, Z. Huang, C. Wang, H. Wu, Y. Cui, An intermediate temperature garnet-type solid electrolyte-based molten lithium battery for grid energy storage, *Nat. Energy* 3 (2018) 732–738.
- [38] L. Chen, Y. Li, S.P. Li, L.Z. Fan, C.W. Nan, J.B. Goodenough, PEO/garnet composite electrolytes for solid-state lithium batteries: From “ceramic-in-polymer” to “polymer-in-ceramic”, *Nano Energy* 46 (2018) 176–184.

- [39] F. Capuano, F. Croce, B. Scrosati, Composite polymer electrolytes, *J. Electrochem. Soc.* 138 (1991) 1918-1922.
- [40] J. Zhang, N. Zhao, M. Zhang, Y. Li, P.K. Chu, X. Guo, Z. Di, X. Wang, H. Li, Flexible and ion-conducting membrane electrolytes for solid-state lithium batteries: dispersion of garnet nanoparticles in insulating polyethylene oxide, *Nano Energy* 28 (2016) 447–454.
- [41] C. Zhu, H. Cheng, and Y. Yang, Electrochemical characterization of two types of PEO-based polymer electrolytes with room-temperature ionic liquids, *J. Electrochem. Soc.* 155 (2008) A569-A575.
- [42] A.J. Seeber, M. Forsyth, C.M. Forsyth, S.A. Forsyth, G. Annat, D.R. MacFarlane, Conductivity, NMR and crystallographic study of N,N,N,N-tetramethylammonium dicyanamide plastic crystal phases: an archetypal ambient temperature plastic electrolyte material, *Phys. Chem. Chem. Phys.* 5 (2003) 2692–2698.
- [43] C.Z. Zhao, X.Q. Zhang, X.B. Cheng, R. Zhang, R. Xu, P.Y. Chen, H.J. Peng, J.Q. Huang, Q. Zhang, An anion-immobilized composite electrolyte for dendrite-free lithium metal anodes, *Proc. Natl. Acad. Sci.* 114(2017) 11069-11074.
- [44] Z. Lu, L. Yang, Y. Guo, Thermal behavior and decomposition kinetics of six electrolyte salts by thermal analysis, *J. Power Sources* 156 (2006) 555–559.
- [45] F Croce, L Persi, B Scrosati, F Serraino-Fiory, E Plichta, M.A Hendrickson, Role of the ceramic fillers in enhancing the transport properties of composite polymer electrolytes, *Electrochimica Acta* 46 (2001) 2457–2461.
- [46] H. Wang, N. Imanishi, A. Hirano, Y. Takeda, O. Yamamoto, Electrochemical properties of the polyethylene oxide-Li (CF₃SO₂)₂N and ionic liquid composite electrolyte, *J. Power Sources* 219 (2012) 22–28.
- [47] Y.C. Jung, S.M. Lee, J.H. Choi, S.S. Jang, D.W. Kim, All solid-state lithium batteries

- assembled with hybrid solid electrolytes, *J. Electrochem. Soc.* 162 (2015) A704–A710.
- [48] C. Fasciani, S. Panero, J. Hassoun, B. Scrosati, Novel configuration of poly(vinylidenedifluoride)-based gel polymer electrolyte for application in lithium-ion batteries, *J. Power Sources* 294 (2015) 180–186.
- [49] S.H.S. Cheng, K.Q. He, Y. Liu, J.W. Zha, M. Kamruzzaman, R.L.W. Ma, Z.M. Dang, R.K.Y. Li, C.Y. Chung, Electrochemical performance of all-solid-state lithium batteries using inorganic lithium garnets particulate reinforced PEO/LiClO₄ electrolyte, *Electrochim. Acta* 253 (2017) 430–438.
- [50] L.C. Yin, J. Liang, G.M. Zhou, F. Li, R. Saito, H.M. Cheng, Understanding the interactions between lithium polysulfides and N-doped graphene using density functional theory calculations, *Nano Energy* 25 (2016) 203–210.
- [51] L. Balo, Shalu, H. Gupta, V. Kumar Singh, R. Kumar Singh, Flexible gel polymer electrolyte based on ionic liquid EMIMTFSI for rechargeable battery application, *Electrochim. Acta* 230 (2017) 123–131.
- [52] D. Shang, J. Fu, Q. Lu, L. Chen, J. Yin, X. Dong, Y. Xu, R. Jia, S. Yuan, Y. Chen, W. Deng, A novel polyhedral oligomeric silsesquioxane based ionic liquids (POSS-ILs) polymer electrolytes for lithium ion batteries, *Solid State Ionics* 319 (2018) 247–255.
- [53] S. Xu, Y. Zhang, J. Cho, J. Lee, X. Huang, L. Jia, J.A. Fan, Y. Su, J. Su, H. Zhang, H. Cheng, B. Lu, C. Yu, C. Chuang, T. Il Kim, T. Song, K. Shigeta, S. Kang, C. Dagdeviren, I. Petrov, P. V. Braun, Y. Huang, U. Paik, J.A. Rogers, Stretchable batteries with self-similar serpentine interconnects and integrated wireless recharging systems, *Nat. Commun.* 4 (2013) 1543–1548.
- [54] B. Sun, J. Mindemark, K. Edström, D. Brandell, Realization of high performance polycarbonate-based Li polymer batteries, *Electrochem. Commun.* 52 (2015) 71–74.

- [55] Y.Y. Lu, K. Korf, Y. Kambe, Z.Y. Tu, L.A. Archer, Ionic-liquid-nanoparticle hybrid electrolytes: Applications in lithium metal batteries, *Angew. Chem. Int. Ed.* 53 (2014) 488–492.
- [56] M. D. Tikekar, L. A. Archer, D. L. Koch, Stability analysis of electrodeposition across a structured electrolyte with immobilized anions, *J. Electrochem. Soc.* 161 (2014) A847–A855.
- [57] H. Huo, N. Zhao, J. Sun, F. Du, Y. Li, X. Guo, Composite electrolytes of polyethylene oxides/garnets interfacially wetted by ionic liquid for room-temperature solid-state lithium battery, *J. Power Sources* 372 (2017) 1–7.
- [58] W. Zha, F. Chen, D. Yang, Q. Shen, L. Zhang, High-performance $\text{Li}_{6.4}\text{La}_3\text{Zr}_{1.4}\text{Ta}_{0.6}\text{O}_{12}$ /poly(ethylene oxide)/succinonitrile composite electrolyte for solid-state lithium batteries, *J. Power Sources* 397 (2018) 87–94.
- [59] F. Ma, Z.Q. Zhang, W. Yan, X. Ma, D. Sun, Y. Jin, X. Chen, K. He, Solid Polymer Electrolyte Based on Polymerized Ionic Liquid for High Performance All-Solid-State Lithium-Ion Batteries, *ACS Sustainable Chem. Eng.* 7 (2019) 4675–4683.
- [60] S. Wang, Q. Zeng, A. Wang, X. Liu, J. Chen, Z. Wang, L. Zhang, Constructing stable ordered ion channels for a solid electrolyte membrane with high ionic conductivity by combining the advantages of liquid crystal and ionic liquid, *J Mater. Chem. A* 7 (2019) 1069–1075.

Chapter 4 A sandwich-type composite solid-state electrolyte for lithium metal batteries with high areal capacity and cycling stability

4.1 Introduction

Nowadays, almost all applied lithium batteries use flammable liquid electrolytes with limited energy density, and poor thermal and chemical stability. Development of lithium metal batteries with high energy density as well as senior safety becomes more and more important with the broad applications of electric vehicles and various portable devices [1-2]. Recently, all-solid-state lithium metal batteries (ASSLMBs) based on solid-state electrolytes are being intensively pursued by many researchers [3-4]. Various solid-state electrolytes including sulfide-, oxides- and polymer-based electrolytes have been widely developed [5-10]. In particular, composite polymer electrolytes (CPEs) fabricated by addition of fillers with high lithium ion conductivity to the solid polymer electrolytes have been attracted the most extensive attention because of their excellent ionic conductivity, wide electrochemically stable window, facile synthesis, good flexibility, and excellent compatibility with electrodes [11-12]. It is found that the introduction of the ceramic electrolyte filler can effectively enhance not only ionic conductivity and mechanical property but also thermal stability of the whole CPEs [13-14]. Especially, $\text{Li}_{6.4}\text{La}_3\text{Zr}_{1.4}\text{Ta}_{0.6}\text{O}_{12}$ (LLZTO), a garnet-type fast-ion conducting ceramic electrolyte with high bulk conductivity (more than $10^{-3} \text{ S cm}^{-1}$ at ambient temperature), wide potential window range (above 6 V vs. Li/Li^+) and excellent chemical stability against Li metal, is one of the most promising candidates [15].

PEO-lithium salts (e.g., lithium bis(trifluoromethylsulfonyl)imide (LiTFSI), LiBF_4 , and LiClO_4) based polymer electrolytes are the most studied ones with high acceptable anodic stability, good membrane-forming capability, and relatively high ability to transfer Li^+ ions [16-17]. To date,

various fillers have been combined with them to further improve their performances. For instance, PEO-LiTFSI-Mg₂B₂O₅ [18], PEO-LiClO₄-Li_{0.33}La_{0.557}TiO₃ [19] and PEO₁₈-LiTFSI-Li₁₀GeP₂S₁₂ [20] have been developed for the CPEs. However, their performances are still far away from the practical requirements. Also, as the previous reported, the polymer electrolytes with PEO are slowly oxidized at voltages over 4.0 V [21], which restricts their applications in the cells with a high-voltage cathode. To solve this issue, Ma *et al.* fabricated a poly(ethyl cyanoacrylate) coating layer with a strong electron withdrawing group of -C≡N to suppress the oxidation of PEO electrolyte for matching the high voltage LiCoO₂ cathode [22]. To reduce the side reaction of the electrolyte with an electrode, Wan *et al.* reported a PEO-based electrolyte filled with Li₇La₃Zr₂O₁₂ nanowires, which possessed much higher voltage stability at 4.2 V [23]. Chen *et al.* proposed a high-voltage (3.0-4.95 V) flexible battery based on PVDF-HFP gel electrolyte doped with PEO via weak bond interactions, and the intermolecular hydrogen bonding effect between them enables the copolymer chains to form a three-dimensional (3D) porous polymer network, which helps to keep good electrochemical stability [24].

Poly(vinylidene fluoride-hexafluoropropylene) (PVDF-HFP) with relatively low crystallinity and some functional groups with strong electron withdrawing effect is another attractive polymer electrolyte host for the CPEs since it has long-term thermal and electrochemical stability and high ionic conductivity at ambient temperature [25]. Notably, the PVDF-HFP-based CPEs can match the high-voltage commercial cathodes such as LiCoO₂ (518 Wh kg⁻¹) and LiNi_{1/3}Mn_{1/3}Co_{1/3}O₂ (576 Wh kg⁻¹) to create high-energy density cells for meeting the 500 Wh kg⁻¹ level goal [26-27]. Also, the PVDF-HFP based CPEs have strong mechanical strength to suppress lithium dendrites. However, as they assembled with the electrodes, the large electrolyte-electrode interfacial resistance still appears. In this case, it is general to add routine liquid electrolyte to reduce the interface resistance [28-33], however, the additional flammable liquid electrolyte could result in

some safety issue and simultaneously decrease the energy density.

To overcome these problems, Goodenough *et al.* proposed a sandwich architecture design of CPE, in which the ceramic membrane electrolyte sandwiched by two polymer electrolyte skin layers [34]. Such a sandwich architecture CPE can not only prevent the reaction between electrolyte and lithium metal but also reduce the interface resistance and suppress the lithium dendrite growth. Inspired by this sandwich structure, in this work, the interface resistances between PVDF-HFP-based CPE and electrodes were also considered to be solved by sandwiching it with the polymer layer such as the popular PEO-LiTFSI electrolyte. Beyond that, the crystallinity of both PEO and PVDF-HFP could be reduced via the cross-linking between the polymer chains of them at the interfacial sections [24, 35], which is expected to result in faster Li^+ ions transportation in the whole sandwich-type CPEs. Meanwhile, it is worth noting that most researchers assembled their solid electrolytes with the cathodes having a low mass amount (around 2 mg cm^{-2} , 0.3 mAh cm^{-2}) to avoid the ion diffusion limitation [11, 19, 36-39]. However, such a low content of active materials in the cathode does in fact limit the practical applications in portable devices, in which at least 10 mg cm^{-2} of a mass amount is required [40]. Moreover, to achieve high-energy density in all-solid-state batteries, it is generally necessary to have high energy density cathode, large cathode mass loading, thin solid-state-electrolyte membrane, suitable the negative/positive electrode areal capacity ratio (N/P ratio), and limited amounts of Li metal [41-43]. Thus, development of advanced CPEs which can be assembled with high areal capacity cathodes and thin Li metal anode for the practical ASSLBs is more important.

In this study, a flexible and stable sandwich-type CPE film was fabricated by sandwiching the PVDF-HFP-LLZTO composite electrolyte with the PEO-LiTFSI polymer electrolyte layers (PEO₈-LiTFSI/PVDF-HFP-15%LLZTO/PEO₈-LiTFSI, referred to as sandwich-type CPE) for the ASSLMBs. As expected, the sandwich-type CPE film had higher ionic conductivity, wider thermal

and electrochemical stability window, and improved mechanical and interfacial properties. Moreover, all-solid-state LiFePO_4 (high areal capacity cathode: 1.5 mAh cm^{-2}) |Li-metal battery assembled with this sandwich-type CPE film exhibited excellent rate performance and cycle stability with a negligible discharge capacity decay up to $120.01 \text{ mAh g}^{-1}$ even after 300 cycles test at 40°C . Meanwhile, the all-solid-state LiCoO_2 (1.5 mAh cm^{-2}) |Li-metal as well as $\text{LiNi}_{1/3}\text{Mn}_{1/3}\text{Co}_{1/3}\text{O}_2$ (1.5 mAh cm^{-2}) |Li-metal batteries with sandwich-type CPE also showed satisfied high-voltage stability with good cycle performance. Furthermore, the fabricated flexible pouch cell also had excellent performance, indicating its feasibility for the flexible ASSLMBs.

4.2 Experimental

4.2.1 Preparation of electrolyte membrane

The composite polymer electrolyte (CPE) membrane was prepared by solution casting technique. Firstly, based on our preliminary experiments, PVDF-HFP pellets were dissolved in a mixed solvent of N, N-dimethylacetamide (DMAc) and acetone with a volume ratio of 1:2, resulting in a solution containing 20 wt.% of the PVDF-HFP. The solution was stirred at 50°C for 12 h and then, LLZTO powders were added and kept stirring for 12 h in ambient temperature, and a viscous solution with 15 wt.% of LLZTO powders was obtained, which is named as PVDF-HFP-15% LLZTO solution. Finally, this solution was spread on a clean glass plate by a film applicator, and the obtained membrane with a thickness of $100 \mu\text{m}$ was vacuum dried at 60°C for 12 h, the thickness of membrane can be adjusted by a film applicator. Thereafter, the uniform membrane was punched into circles with diameter of 12 mm and 16 mm, respectively, and then cold pressed for 3 min at 10 MPa for further measurements.

For fabrication of the sandwich-type CPE membrane, firstly, according to the pre-experimental designs, the $\text{PEO}_8\text{-LiTFSI}$ powder with a molar ratio of PEO to LiTFSI of 8 was chosen for preparation of the PEO-LiTFSI membranes at first since this material showed high ionic

conductivity and flexible. The PEO-LiTFSI membrane was prepared with the similar process as described above. In brief, PEO₈-LiTFSI powder was also dissolved in the mixed solvent of N, N-dimethylacetamide (DMAc) and acetone with a volume ratio of 1:2, which the concentration PEO powder was 10 wt.%, and stirred at 50 °C for 6 h. After that, the final solution was spread on a glass plate by a film applicator, and vacuum dried at 60 °C for 12 h. As such, a PEO-LiTFSI membrane with a thickness of 5-10 μm was obtained. Subsequently, the PVDF-HFP-15% LLZTO solution was spread on this PEO₈-LiTFSI film by a film applicator so that the final thickness of PVDF-HFP-15% LLZTO membrane was about 80 μm. Then, the obtained PEO₈-LiTFSI/PVDF-HFP-15% LLZTO double-layer membrane was dried at 40 °C for 1 h. Thereafter, the PEO₈-LiTFSI solution was spread on the PVDF-HFP-15% LLZTO layer so that the other PEO₈-LiTFSI layer with a thickness of 5-10 μm was formed on the other side of PVDF-HFP-15% LLZTO layer. Finally, the PEO₈-LiTFSI/PVDF-HFP-15% LLZTO/ PEO₈-LiTFSI sandwich membrane was vacuum dried at 60 °C for 24 h. This sandwich-type CPE (called as P/PL/P sandwich CPE) was also punched into circles with diameters of 12 mm and 16 mm respectively and then cold pressed for 3 min at 10 MPa for further measurements.

4.2.2 Characterizations and electrochemical measurement

Morphology and elemental distributions of the obtained CPE membranes were investigated via SEM, AFM, and EDS analysis systems, respectively. The crystal structure of CPE membrane was determined by XRD technology using a Cu-Kα ($\lambda=1.5405 \text{ \AA}$) radiation source in the 2θ range of 10-60°. Thermogravimetric analysis (TGA) curves of the samples were obtained by a DTG-60H analysis instrument with a heating rate of 10 °C min⁻¹ from 25 °C to 800 °C under N₂ atmosphere. Differential scanning calorimetry (DSC) measurements were carried out on the EXSTAR 6000 instrument with a heating rate of 10 °C min⁻¹ from 25 to 200 °C under an Ar atmosphere.

For electrochemical measurements, the ionic conductivity σ (23-100 °C), lithium-ion

transference (t_{Li+}) number, and electrochemical stability window (2.0-6.5 V) of prepared CPE membranes were calculated by the same procedure as described in section 3.2.2 *Characterizations and electrochemical measurement*.

4.2.3 Cell assembly

For the anode, on the one hand, the commercial thick Li foil (diameter: 12 mm, thickness: 100 μ m) was used directly with a Cu foil current collector. On the other hand, the Li metal granular was adopted for preparing the thin Li foil by cold pressing (less than 20 μ m) as following: a certain amount of Li metal granular was placed on the surface of Cu foil, and then cold pressed for 30 min at 387 MPa. Particularly, with wetted by trace DMC (dimethyl carbonate), the Li foil was easily separated from the mold.

For cells assembly, the obtained CPE membrane (diameter: 16 mm) was sandwiched between different cathode foil (diameter: 12 mm) and Li foil (diameter: 12 mm), and placed into CR2025-type coin cell case, and then pressed at 750 psi for further measurements. CR2025-type $LiFePO_4$, $LiCoO_2$ or $LiNi_{1/3}Mn_{1/3}Co_{1/3}O_2$ |Li metal coin cell with the prepared CPE membrane was measured with an SD8data testing system (Hokuto Denko Corporation Co., Ltd. Japan). Meanwhile, a simplified pouch $LiFePO_4$ |Li metal cell (The area of electrodes: 3 cm * 3 cm) with the sandwich-type CPE membrane was also assembled and charged to test the capability of lighting the LED device before and after bending. In this study, all the solid-state electrolyte batteries were assembled without using a separator or additional liquid electrolyte in an Ar-filled glove box with water and oxygen contents of below 0.01 ppm.

4.3 Results and discussion

4.3.1 Physicochemical properties of the sandwich-type CPE membrane

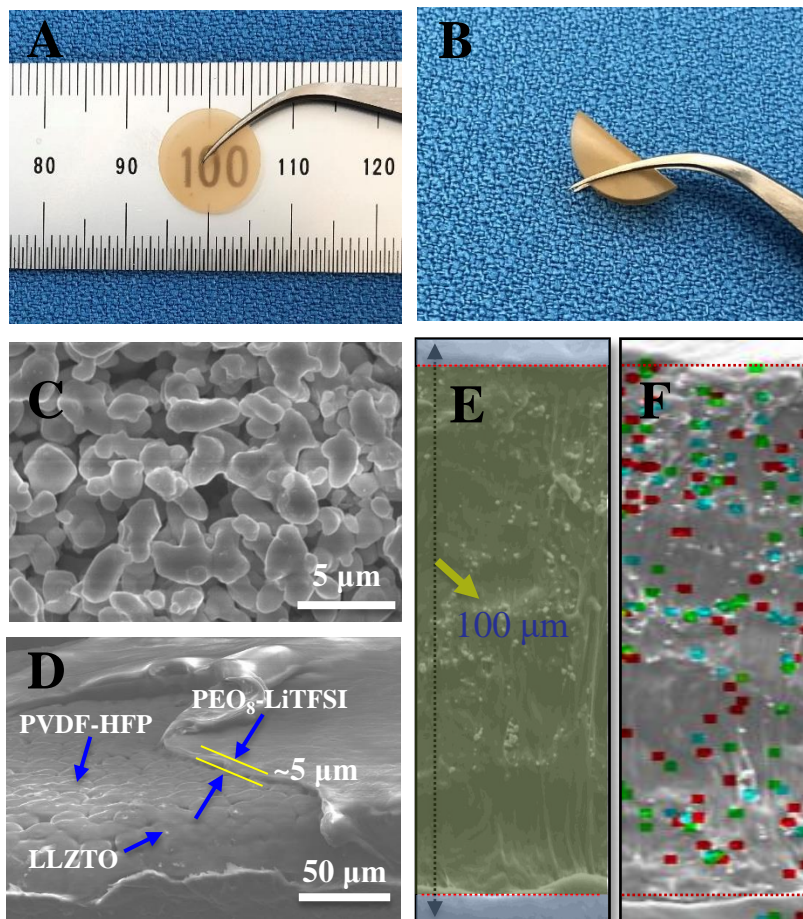


Fig. 4.1 Photographs of the prepared $\text{PEO}_8\text{-LiTFSI/PVDF-HFP-15\%LLZTO/PEO}_8\text{-LiTFSI}$ sandwich-type CPE film at (A) flat and (B) bend states; The typical surface morphologies of (C) LLZTO powders and (D) sandwich-type CPE film; Cross-sectional (E) SEM image and (F) EDX mapping of sandwich-type CPE film where green, blue and red dots indicate the location of La, Zr, and Ta elements, respectively.

Figs. 4.1 A and **4.1B** show the photos of the obtained sandwich-type CPE film before and after bending. One can see that the film was freestanding with excellent mechanical flexibility, indicating that it could be used for fabricating wearable ASSLBs. **Fig. 4.1C** shows the typical SEM image LLZTO powders with an average particle size of 5.5 μm , which were homogeneously

distributed in the PVDF-HFP-LLZTO film (**Fig. 4.1D**). As the two sides of PVDF-HFP-LLZTO film are coated with the flexible PEO₈-LiTFSI films, the obtained sandwich film has a smooth surface (**Fig. 4.1D**) due to the high flexibility of PEO-Li salt layer, and from the cross-section SEM image of the sandwich-type CPE film, one can see that the thickness of each PEO₈-LiTFSI film was around 5 μm and that of the total sandwich film was about 100 μm , where the PVDF-HFP polymer and ceramic LLZTO particles were fully intermingled (**Fig. 4.1E**). **Fig. 4.1F** shows the EDX mapping of La, Zr and Ta elements in LLZTO. One can see that LLZTO particles mainly existed in the middle layer.

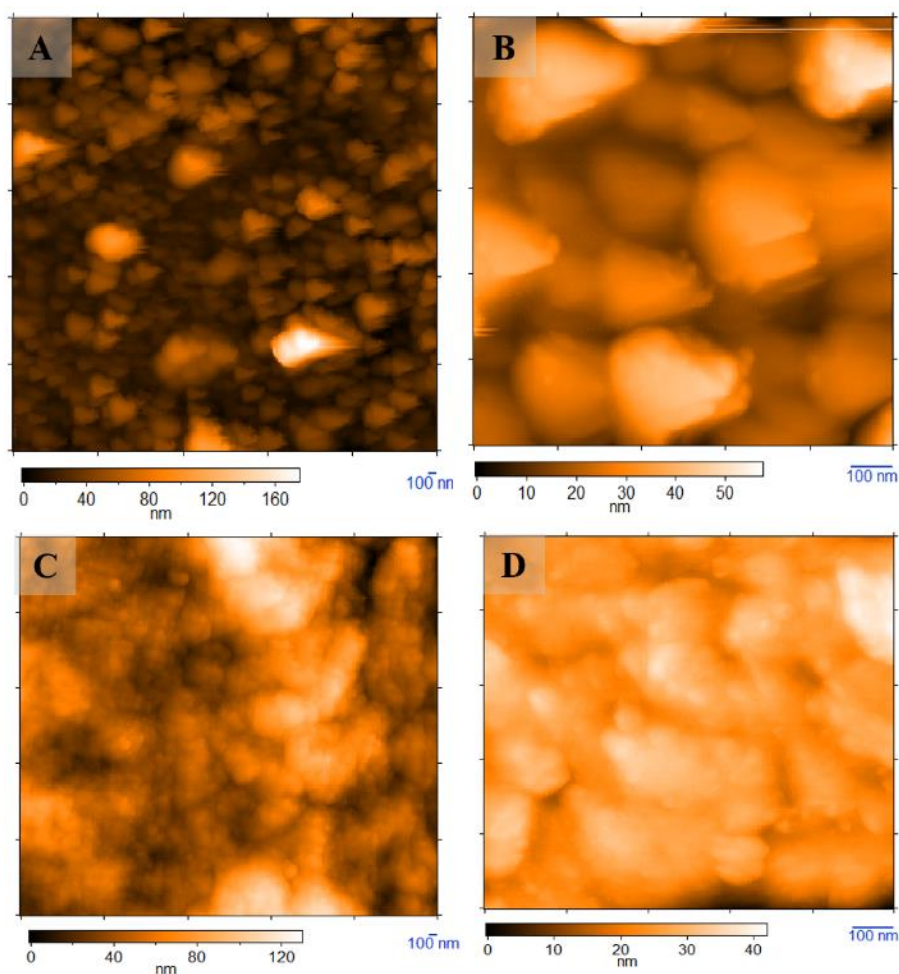


Fig. 4.2. AFM images of (A, B) PVDF-HFP-15% LLZTO CPE membrane and (C, D) sandwich-type CPE membrane.

The AFM images in **Fig. 4.2** revealed a smoother surface of sandwich-type CPE compared to the PVDF-HFP-15% LLZTO CPE. It indicated that the more flexible PEO-Li salt layer increased the continuity of electrolyte surface, decreasing the contact loss with the electrode, leading to a reduced interfacial resistance [44].

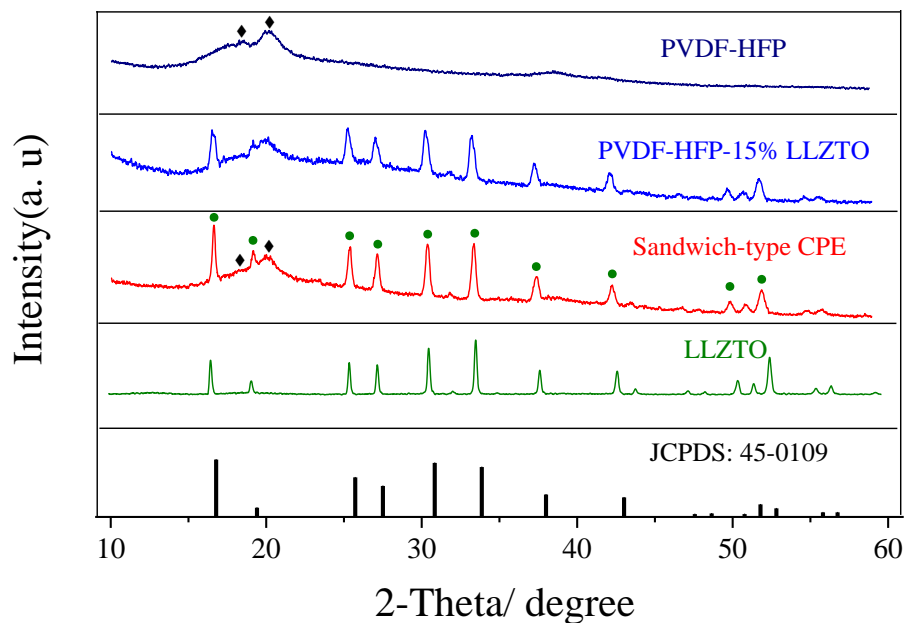


Fig. 4.3 XRD patterns of pure PVDF-HFP, CPE samples, LLZTO ceramic powder and the diffraction pattern of cubic garnet $\text{Li}_5\text{La}_3\text{Nb}_2\text{O}_{12}$ (space group: $Ia-3d$ (230), JCPDS: 45-0109) as the reference.

As shown in **Fig. 4.3**, two intense peaks ($2\theta = 18.2^\circ$ and 20°) indicated the presence of a crystalline phase of PVDF-HFP. After incorporated with ceramic filler LLZTO (PVDF-HFP-15%LLZTO), these two diffraction peaks became broader with much lower intensity, indicating a significant crystallinity decrease of PVDF-HFP polymer. Furthermore, in the sandwich-type CPE film, the crystalline peaks of PVDF-HFP became more weaken and simultaneously all diffraction peaks of LLZTO powder appeared more clearly and matched well with the standard pattern of the cubic-garnet structure $\text{Li}_5\text{La}_3\text{Nb}_2\text{O}_{12}$ (JCPDS: 45-0109). Herein, the decrease of the crystallinity of the polymers should be resulted from the intermolecular bonding between PVDF-HFP and PEO

during the sandwich film fabrication [24].

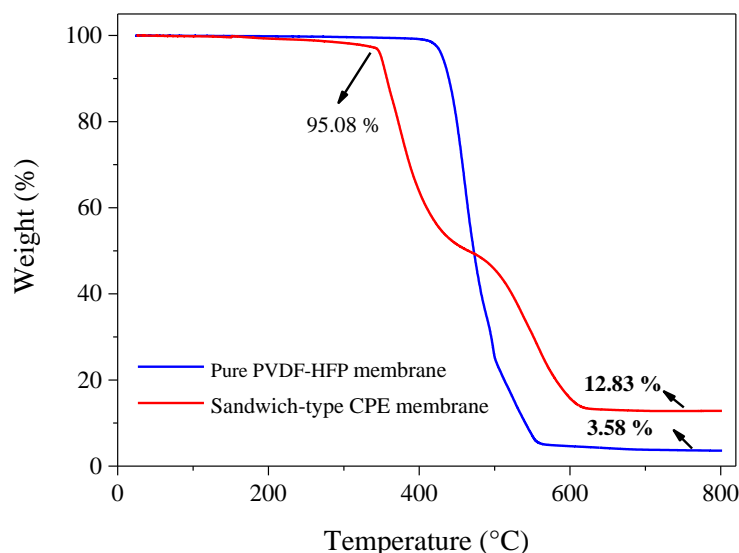


Fig. 4.4 TGA curves of the CPEs.

The thermal behavior was evaluated by the thermogravimetric analysis (TGA). As shown in **Fig. 4.4**, all the prepared films maintain stability at a temperature more than 300 °C. With the further increase of heat, the pure PVDF–HFP polymer began to decompose at 400 °C and was almost completely decomposed at 520 °C with a total weight loss of 96 wt.%. In contrast, for the sandwich-type CPE film, although the weight loss occurred at a lower temperature because of the weaker thermal stability of PEO and lithium salt, the weight loss rate was much slower than the pure PVDF-HFP polymer since the LLZTO has the ultrahigh melting point of 1000 °C [9, 15]. Also, due to the extraordinary thermal stability of the remaining LLZTO filler, 12.83 wt.% weight of the sandwich-type CPE was remained until 800 °C. Herein, addition of more LLZTO filler electrolytes could provide stronger barrier to avoid short circuiting even in the extreme conditions [45], which is matched well with the result in the previous report [33].

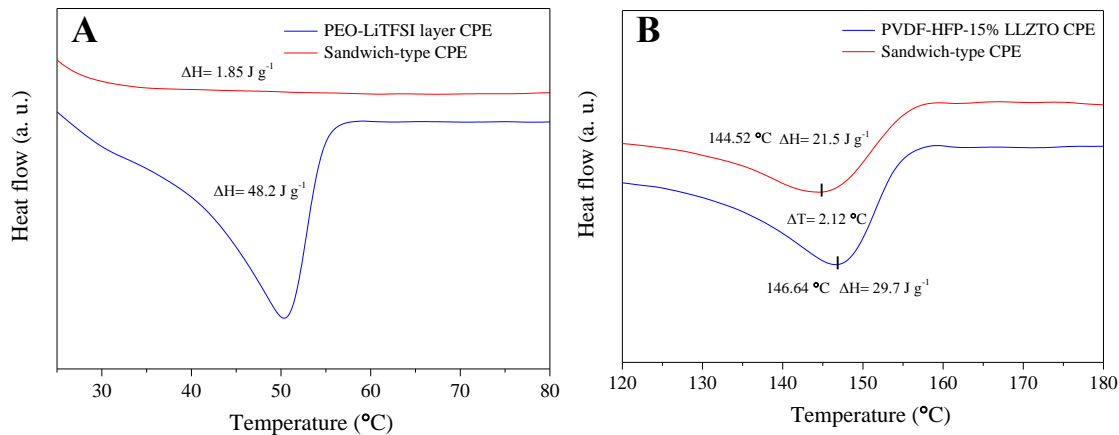


Fig. 4.5 DSC test results of the prepared electrolyte membranes.

The differential scanning calorimetry (DSC) measurements were carried out to explore the phase transition behavior of the prepared CPE membrane. As shown in **Fig. 4.5A**, compared to PEO₈-LiTFSI electrolyte, the crystalline peaks of PEO in the sandwich-type CPE almost disappeared, and the ΔH (melting enthalpy of electrolyte) of PEO for the neat PEO₈-LiTFSI and sandwich-type CPE were 1.85 and 48.2 J g⁻¹, respectively. These results indicated that the crystallinity of PEO was effectively suppressed in the sandwich-type CPE. From **Fig. 4.5B**, one can see that the melting peak of PVDF-HFP-LLZTO matrix shifted to the left slightly with the PEO-LiTFSI layer addition from 146.64 °C for the PVDF-HFP to 144.52 °C for the sandwich-type CPE. Besides, the ΔH value was also reduced from 29.2 J g⁻¹ for the PVDF-HFP to 21.5 J g⁻¹ for the sandwich-type CPE. The above results indicated that the crystallinity of both PEO and PVDF-HFP polymer matrix was significantly reduced in the sandwich-type membrane, and the low crystallinity of polymer could promote the segmental motion of polymer chains, resulting in higher ion transportation ability [24].

4.3.2 Electrochemical stability window and ionic conductivity

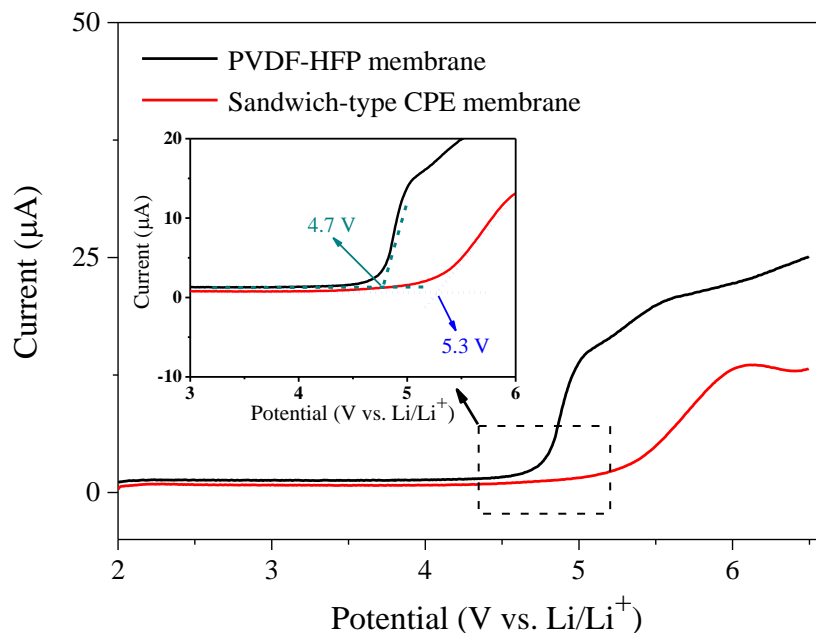


Fig. 4.6 Linear sweep voltammetry (LSV) curves of the prepared CPEs in the range of 2.0-6.5 V at 40 °C with a scan rate of 1 mV s⁻¹. Inset shows the enlarge view of LSV curves.

The electrochemical stability window is a crucial parameter to confirm whether the obtained electrolyte could achieve high-energy density in the high-voltage ASSLMs or not. As shown in **Fig. 4.6**, comparing to the pure PVDF-HFP membrane, the sandwich-type CPE membrane exhibited a stable current density up to 5 V, where only a tiny current was detected (2.91 μA vs. 17.89 μA of PVDF-HFP membrane at 5.3 V), indicating that the obtained sandwich-type CPE membrane had more excellent tolerance to the polarization and much better electrochemical stability against the Li metal. The superior electrochemical stability of the sandwich-type CPE over the PVDF-HFP one should be attributed to the excellent oxidative stability of LLZTO and its surface passivation layer [45]. Meanwhile, as described above, the smoother surface of sandwich-type CPE could decrease the potential of high local current density. Namely, the discontinuity in electrolyte surface could cause local current density amplification and enhance the polarization

process [46]. As such, the obtained sandwich-type CPE could work well with the high-voltage cathode in the Li-ion batteries with high energy density.

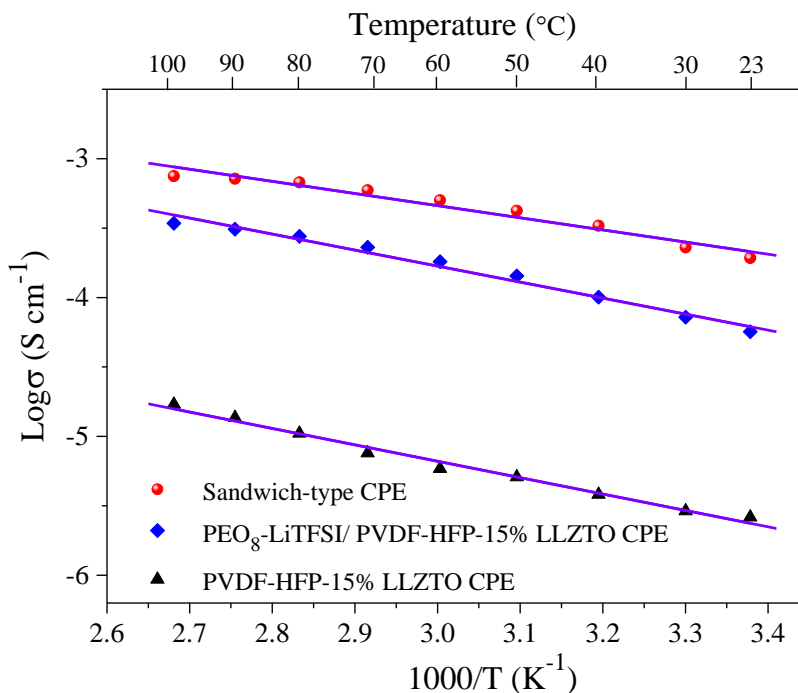


Fig. 4.7 Ionic conductivities of CPEs vs. temperature in the range of 23-100 °C.

Ionic conductivity is another key factor to evaluate the performance of the electrolyte, which is mainly featured by either cation or vacancy conduction [45]. **Fig. 4.7** shows the ionic conductivities of the as-prepared PVDF-HFP-15%LLZTO, PEO₈-LiTFSI/PVDF-HFP-15%LLZTO and sandwich-type CPE at a temperature range of 23-100 °C. In this study, the PEO₈-LiTFSI/PVDF-HFP-15%LLZTO two-layer CPE membrane exhibited a superior ionic conductivity of $7.21 \times 10^{-5} \text{ S} \cdot \text{cm}^{-1}$ at 30 °C, which is approximately 25 times higher than that of PVDF-HFP-15%LLZTO CPE ($2.90 \times 10^{-6} \text{ S} \cdot \text{cm}^{-1}$). As indicated above (2.1 section), the coating of the PEO₈-LiTFSI layer increased the continuity in electrolyte surface, reduced the contact loss with electrode, and decreased the interfacial resistance greatly. Furthermore, as the PEO₈-LiTFSI layer was coated on the other side of the PVDF-HFP-15%LLZTO membrane to form the

sandwich-type CPE membrane, the ionic conductivity was further enhanced to as high as $2.29 \times 10^{-4} \text{ S} \cdot \text{cm}^{-1}$ at 30°C , which almost meets the requirement of a practical battery. Herein, the two $\text{PEO}_8\text{-LiTFSI}$ coated layers worked like that after addition of routine liquid electrolytes ($1.1 \times 10^{-4} \text{ S} \cdot \text{cm}^{-1}$ at 25°C) [33], resulting in the reducing of the interfacial resistance. Moreover, in the sandwich-type CPE membrane, PVDF-HFP-PEO copolymer was formed at the interfacial sections during the drying and pressing treatment processes, and in this case, the PVDF-HFP-PEO copolymer always exhibits higher ionic conductivity than the pure PVDF-HFP one [24]. Also, as shown in **Figs. 4.3** and **4.5**, and as discussed in section 4.3.1, the crystallization of polymers in the sandwich-type CPE membrane was also reduced greatly, which could ameliorate the contact with the electrodes, reduce the interfacial resistance and guarantee the fast transport of Li^+ .

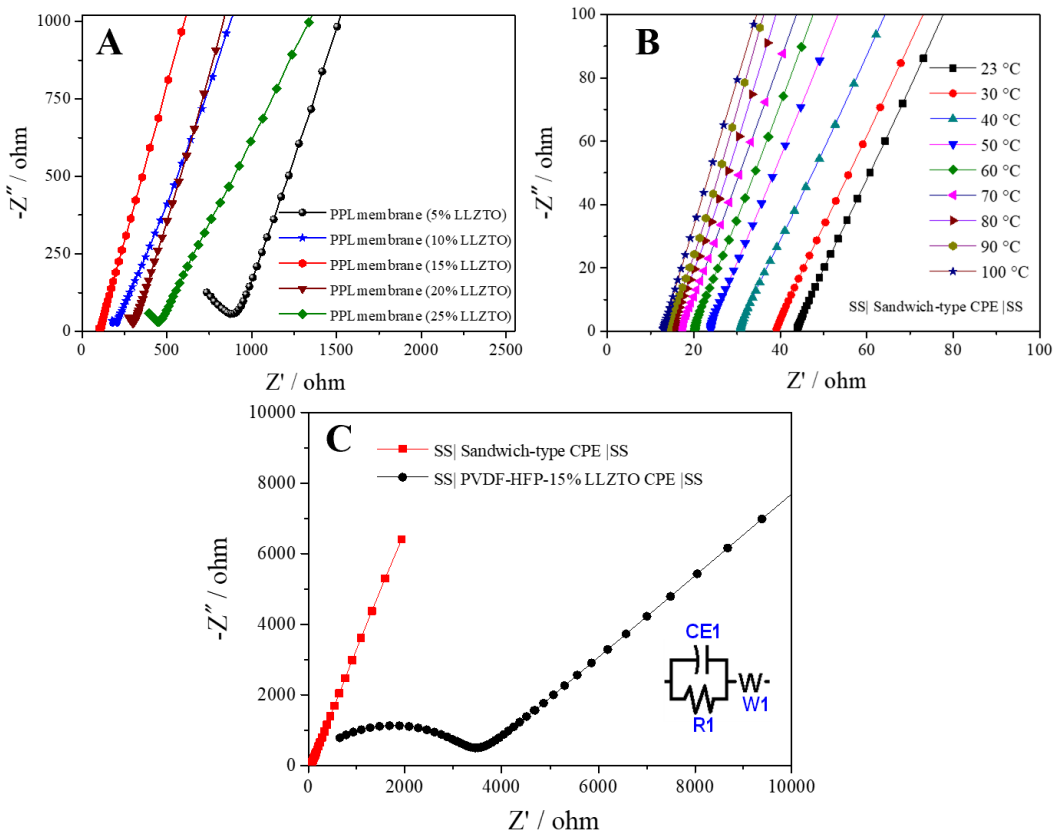


Fig. 4.8 Impedance spectra of (A) the $\text{PEO}_8\text{-LiTFSI/PVDF-HFP-LLZTO}$ (PPL) two-layer CPE membrane as a function of the weight percentage of ceramics filler LLZTO at 40°C and (B) the

sandwich-type CPE membranes working at a temperature ranged from 23 to 100 °C; (C) The compared EIS spectra of PVDF-HFP-15%LLZTO CPE and the sandwich-type CPE membranes at ambient temperature. The inset shows the equivalent circuit.

Fig. 4.8A shows the electrochemical impedance spectroscopy (EIS) of the PEO₈-LiTFSI/PVDF-HFP-LLZTO two-layer CPE membrane as a function of the weight percentage of ceramics filler LLZTO at 40 °C. One can see that the impedance decreased with the increase in the addition amount of LLZTO at first; however, as the addition amount was over 15 wt.%, the impedance increased again. It is possible that the extra addition of ceramics filler could make the film rougher and harder, increasing the interface impedance in the CPEs [19, 47]. Hence, the optimum amount of LLZTO was chosen as 15 wt.% in this study. **Fig. 4.8B** shows EIS of the sandwich-type CPE membrane working in the temperature ranged from 23 to 100 °C. One can see that the impedance decreased with the increase in the working temperature. This result in agreement with other solid electrolytes [33]. **Fig. 4.8C** compares EIS of the PVDF-HFP-15%LLZTO CPE and sandwich-type CPE membranes measured at room temperature. It is obvious that the sandwich-type CPE membrane had a much lower impedance.

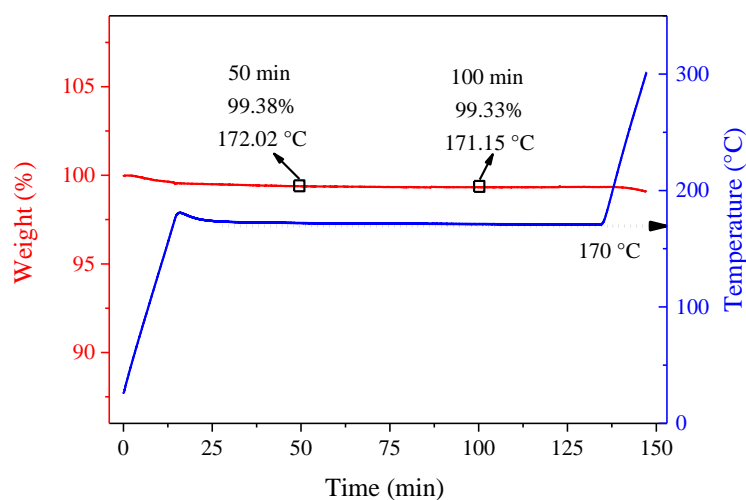


Fig. 4.9 TGA curve of the sandwich-type CPE.

For the ion conduction of the solid-state-electrolyte, it is critical to verify that there is no organic solvent or liquid electrolyte vapor that have been absorbed into the electrolyte. The TGA measurements were carried out to verify that the solvent in the sandwich-type membrane was removed after vacuum drying at 60 °C for 24 h. Firstly, as shown in **Fig. 4.9**, the TGA curve was obtained with a heating rate of 10 °C min⁻¹ from ambient temperature to 180 °C, and then kept at about 170 °C for 120 min, after that, increased to 300 °C with the same rate under N₂ atmosphere. One can see that the weight of the sandwich-type CPE maintained almost unchanged. This result indicated that the solvents present in the sandwich-type CPE can be removed by a vacuum drying at 60 °C for 24 h. In addition, as shown in **Fig. 4.10**, one can see that the ionic conductivity of sandwich-type CPE got some improved when exposed to liquid electrolyte vapor. Thus, it is necessary to minimize the vapor exposure and enforce the rigorous drying procedure to obtain high reliability and reproducibility during the preparation of the electrolyte membrane [48]. In this study, taking the ionic conductivity and discharged capacity into account, 40 °C was chosen as the optimum operating temperature of ASSLMBs.

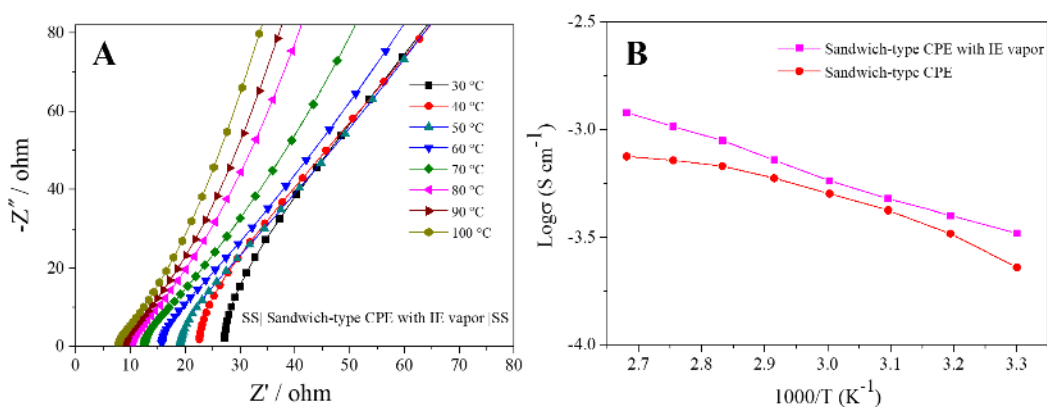


Fig. 4.10 (A) Impedance spectra and (B) ionic conductivities of the sandwich-type CPE membrane with liquid electrolyte vapor from 30 to 100 °C.

4.3.3 Lithium ion transference number

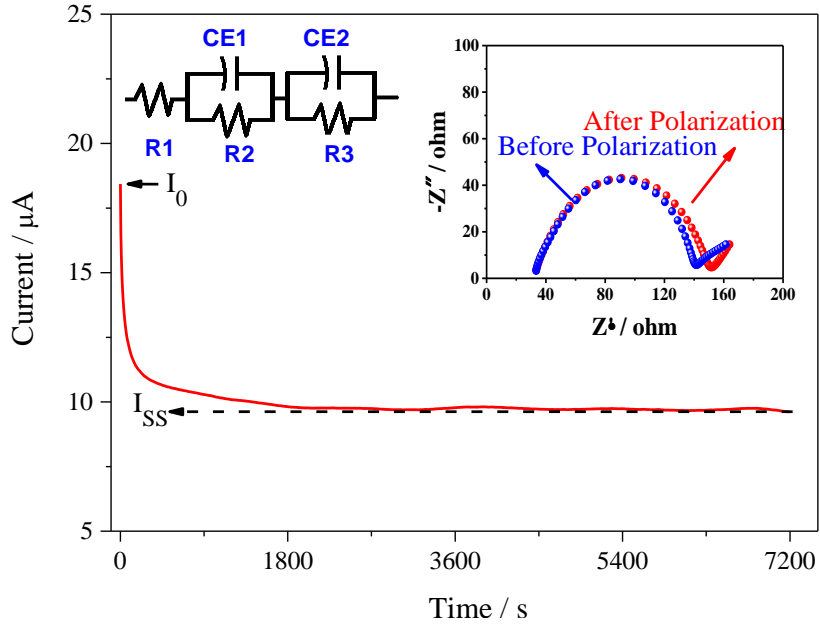


Fig. 4.11 DC polarization curve for Li|sandwich-type CPE|Li cell under a polarization voltage of 10 mV. The insets show the equivalent circuit and EIS before and after the polarization, respectively.

Lithium-ion transference number (t_{Li^+}) is also an essential parameter to evaluate the performance of the prepared CPEs. In this study, the t_{Li^+} was investigated by a combined AC/DC technique as described in the experimental section and the value of t_{Li^+} was calculated by equation S2. **Fig. 4.11** shows the variation of current with time in the polarization process. The insets are the simulating equivalent circuit and impedance spectra, respectively, where R_1 stands for the electrolyte resistance, R_2 and R_3 the resistances of two electrolyte-electrode interfaces in Li|sandwich-type CPE|Li, and $CE1$ and $CE2$ stand for the constant phase elements. The simulated impedance responses were calculated directly using ZView software [45]. As shown in Fig. 7, one can see that the current reached a steady value of 0.01 mA from the initial state of 0.018 mA before the polarization, and the interfacial resistance increased from 91.4 to 100.8 Ω through the polarization. As such, the calculated t_{Li^+} of the sandwich-type CPE membrane was approximately

0.52, which was even higher than those of commercial liquid electrolytes ($t_{Li^+}=0.2-0.5$), and entirely suitable for the practical ASSLMs [36]. High t_{Li^+} of the sandwich-type CPE membrane should be attributed to the following factors: (i) a high t_{Li^+} ($t \approx 1$) of the LLZTO particles, which could improve the whole t_{Li^+} of the sandwich-type CPE membrane through ion hopping between the ceramic particles along the cross sectional direction; (ii) the HFP group of PVDF-HFP including F atoms with strong electronegativity in the amorphous region, which could attract the Li^+ ions to migrate within the disorder part [30]; (iii) the significantly reduced crystallinity of PVDF-HFP polymer matrix with the PEO-Li salt layer coating (DSC test results), which could promote the segmental motion of polymer chains, resulting in a higher ion transference ability; and (iv) the barrier effect of the PVDF-HFP-LLZTO to the anion, which could ensure the Li^+ transference in the sandwich-type CPE, reducing the double-layer electric field at the Li/polymer interface, like some single ion conducting polymer electrolytes [34]. Nevertheless, the whole t_{Li^+} of the sandwich-type CPE membrane was still less than the single-ion conductor ($t_{Li^+} \approx 1$) since the PEO-LiTFSI layers had the low t_{Li^+} (about 0.21) [9, 45]. Herein, it is expected that the high t_{Li^+} of sandwich-type CPE could also prevent the creation of a large electric field within the space-charge region by immobilizing LLZTO [49]. Moreover, the high t_{Li^+} could help Li^+ ions uniformly distributed on the anode surface and render dendrite-free Li deposition [45]. According to the results mentioned above, an ionic transport mechanism can be proposed as follows: for the skin layers, the lithium ion transport occurs by the local relaxation and segmental motion of polymer chains in the PEO-LiTFSI based electrolyte [17]. As for the PVDF-HFP-LLZTO layer, the existence of the interaction of the polarity fluorine atoms in the PVDF-HFP with Li ions can increase the number of ion carriers, and meanwhile, the functional groups of PVDF-HFP with a strong electron withdrawing effect could suppress the mobility of charge, thereby reducing the

magnitude of the electric field across the interface and facilitating the stabilization of the polymer electrolyte [34]. As such, with the assistance of the garnet-type fast-ion conducting ceramic electrolyte of LLZTO, ionic hopping in the available sites could be further enhanced [11]. Meanwhile, at the interfaces between the PVDF-HFP-LLZTO and PEO-LiTFSI layers, the PVDF-HFP could enhance the dissociation of LiTFSI since it has a higher dielectric constant which is benefit for the ionization of lithium salt [44]. In addition, owing to the cross-linking occurred at the interfacial sections, the crystallinities of PEO as well as PVDF-HFP polymer matrix are decreased, which are favorable for not only Li^+ transportation, but also fast TFSI-intercalation/deintercalation kinetics [24, 34].

4.3.4 Rate performance and cycle stability of LMBs

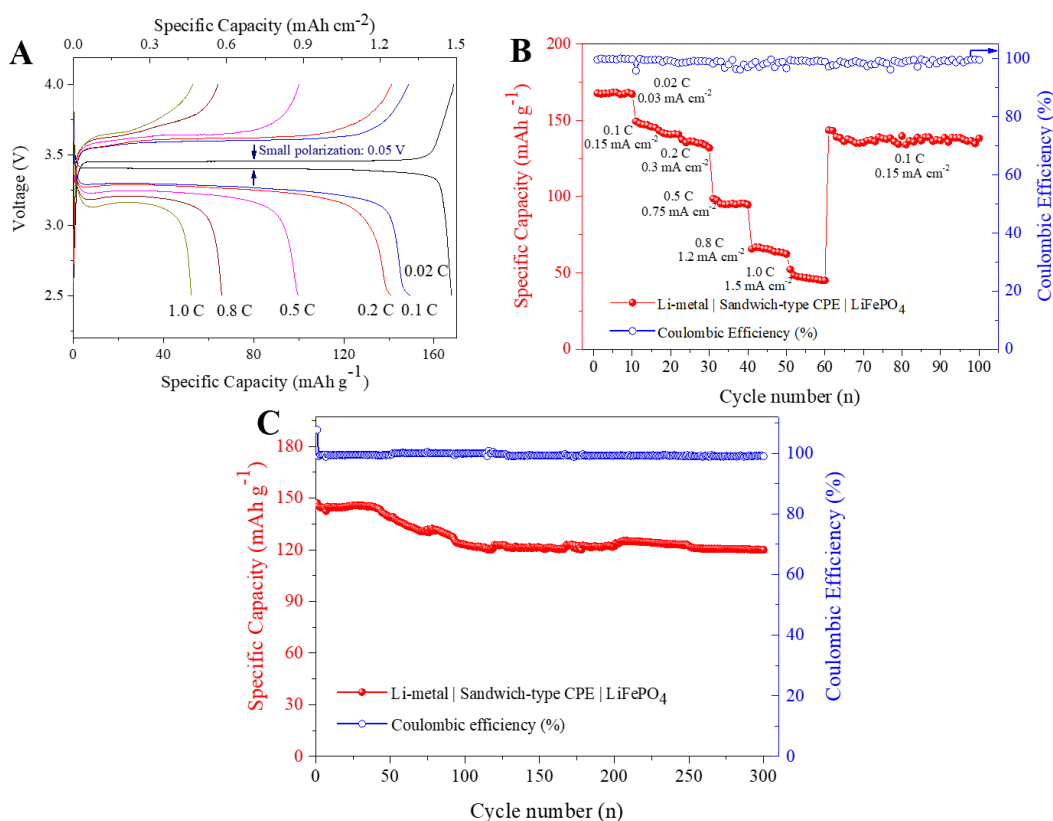


Fig. 4.12 (A) Initial charge-discharge profiles at different rates and (B) rate performance of the

LiFePO₄| sandwich-type CPE |Li-metal battery; (C) cycling stability of all-solid-state LiFePO₄|Li cells with the sandwich-type CPE at 0.2 C and 40 °C.

To verify the applicability of the PEO₈-LiTFSI/PVDF-HFP-15%LLZTO/PEO₈-LiTFSI sandwich-type CPE membrane in the ASSLMs, all-solid-state Li metal batteries based on the sandwich-type CPE membrane with high mass loading amounts of commercial LiFePO₄ cathode material were assembled. The initial charge-discharge profiles of the LiFePO₄|sandwich-type CPE|Li-metal battery at 40 °C with different rates are shown in **Fig. 4.12A**. The cell exhibited a clear potential plateau in a voltage range of 2.5-4.0 V, indicating an excellent reversible cycling property. Moreover, the battery delivered a high discharge capacity of 167.8 mAh g⁻¹ at 0.02 C (0.03 mA cm⁻²), which reached 98.7 % of the theoretical value, and the polarization during the cycling process was limited at a low value of 0.05 V. In addition, the battery offered high discharge capacities of 149.4, 141.0, 99.7, 65.8 and 52.2 mAh g⁻¹ at rates of 0.1, 0.2, 0.5, 0.8 and 1 C, respectively. As shown in **Fig. 4.12B**, after the cycling at 1 C, the discharge capacity was recovered to 143.6 mAh g⁻¹ as the rate returned to 0.1 C, reaching 96.11% of the initial discharge capacity. These observed rate performances indicated the stability of the sandwich-type CPE film, especially in the large current density.

Cycle performances were also evaluated with a rate of 0.2 C at 40 °C. As shown in **Fig. 4.12C**, the discharge capacity of the battery in the voltage range of 2.5-4.0 V exhibited a negligible decay from 147.17 to 144.38 mAh g⁻¹ within the first 40 cycles, indicating a high capacity retention of 98.10%. In contrast, the cell exhibited a fast decay from 144.38 to 123.05 mAh g⁻¹ in the following cycles until 100 cycles. From the previous reports [21], it should be attributed to that the PEO polymer can gradually diffuse across the porous SEI layer and lead to a little loss of lithium from the cathode [34]. Moreover, the discharge capacity of battery exhibited a slow decay in the first 40

cycles, and in this case, some intermolecular bonds between PVDF-HFP and PEO could be changed at a high current density (0.3 mA cm^{-2}), resulting in a larger interfacial resistance and higher crystallinity of polymer matrix. Meanwhile, a structural reorganization of the electrolyte could lead the formation of new electrolyte/electrode interfaces in this process. In general, the electrolyte species could infiltrate into the electrode structure in the initial few cycles, which may also result in the low discharge capacity [50-51]. As a result, the battery exhibited a fast decay from 40 to 100 cycles. After that, the battery showed a good cycling stability due to the formation of a more stable interface, which was identified by the following SEM image of the sandwich-type CPE after the cycling test. Thus, from 100 to 300 cycles, the battery maintained the cycling stability with a discharge capacity of $120.01 \text{ mAh g}^{-1}$ and a coulombic efficiency of near 100 % even after 300 cycles. As discussed above, this superior rate performance and cycling stability should be attributed to the existing of stable CPE/Li metal interface, high t_{Li^+} , low crystallinity of polymer matrix and low interfacial impedance with interlayer modification by PEO-LiTFSI. In addition, the corresponding lithium ion apparent diffusion coefficient for the delithiation process of $\text{LiFePO}_4|\text{Li}$ metal cell with the proposed sandwich-type CPE was calculated to be $5.278 \times 10^{-11} \text{ cm}^2 \text{ S}^{-1}$. An all-solid-state Li metal battery with LiFePO_4 cathode, thin electrolyte membrane ($50 \mu\text{m}$) and a limited excess amount of Li (3.5 mAh) (**Fig. 4.13**) was also assembled and tested. The specific energy and energy density of the thin Li metal|sandwich-type CPE| LiFePO_4 ASSLBs were calculated to be 146.8 Wh kg^{-1} and 301 Wh L^{-1} with the optimized parameters (**Table 4.1**), higher than those data in the previous report [52], demonstrating its potential in practical applications. This result can provide a reference for ASSLBs with limited amount of Li anode.

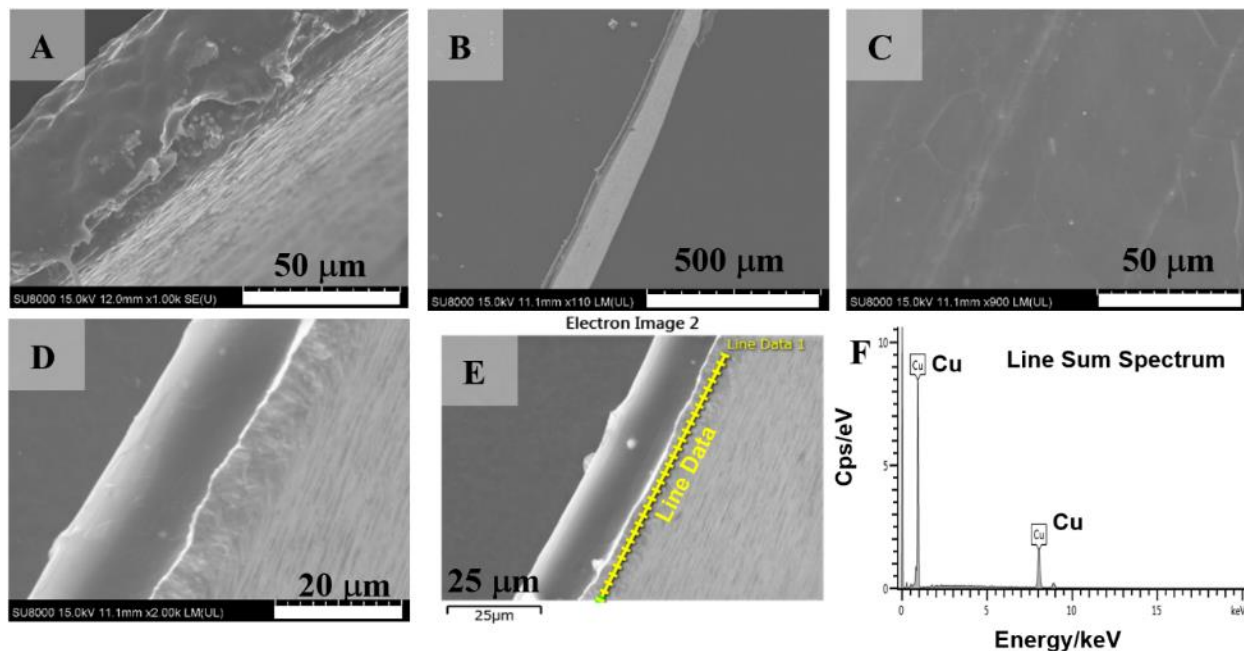


Fig. 4.13 (A) Cross-sectional SEM image of the obtained thin sandwich-type CPE membrane (50 μm); (B) The typical surface morphology; (C) Cross-sectional SEM image of the obtained thin Li metal with Cu current collector; (D) is the enlarged image of (C); (E, F) EDX mapping and analysis of the obtained thin Li metal with Cu current collector where yellow line indicates the Cu elements.

Table 4.1 Technological Parameters of LiFePO₄| sandwich-type CPE |Li-metal ASSLBs.

Component of Cell	Parameter
Al foil	Diameter: 12 mm; Thickness: 15 μm.
Cathode	Material: LiFePO ₄ ; Capacity: 1.69 mAh; Active material ratio: 91%; Thickness: 66.1 μm; Mass (with Al foil): 15.2 mg; Diameter: 12 mm.
Sandwich-type CPE	Diameter: 16 mm; Thickness: 50 μm; Mass: 9.3 mg.
Lithium anode	Diameter: 12 mm; Thickness: 15 μm; Mass: 0.9 mg; Capacity: 3.5 mAh.
Cu foil	Diameter: 12 mm; Thickness: 8 μm; Mass: 10 mg; Porosity: 27%.
Coin Cell	Mass: 35.4 mg; Power (mAh): 5.2 mWh; N/P ratio: 2.07; Gravimetric energy density: 146.9 Wh/kg; Volumetric energy density: 301 Wh/L.

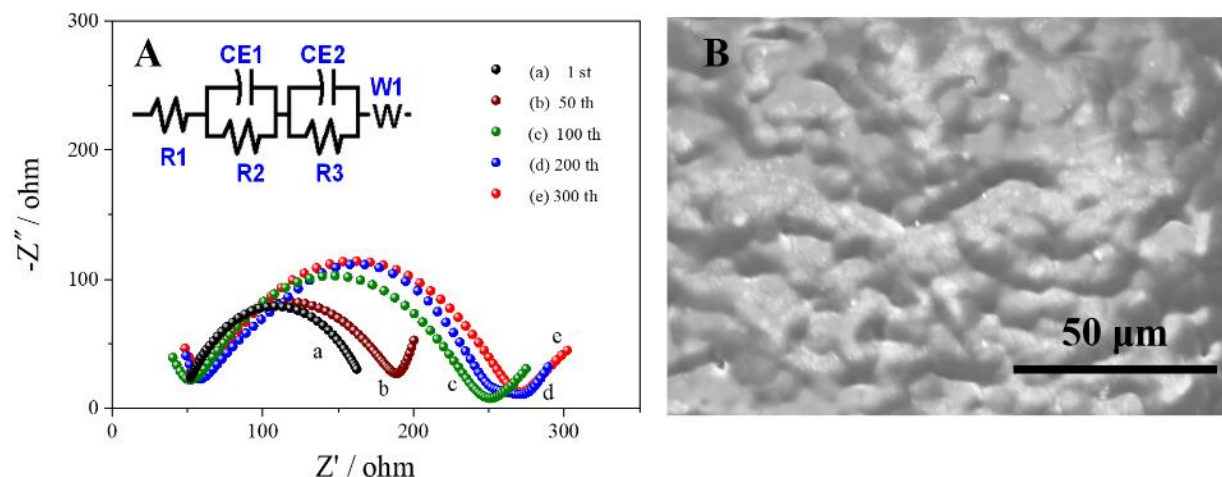


Fig. 4.14 (A) AC impedance changes of the all-solid-state LiFePO_4 |sandwich-type CPE|Li-metal cell after different cycles at 0.2 C and 40 °C, the inset is the equivalent circuit; (B) SEM image of surface morphology for the sandwich-type CPE membrane against Li metal after 300 cycles test.

AC impedance changes of the all-solid-state the LiFePO_4 |sandwich-type CPE|Li-metal battery after different cycles at 0.2 C and 40 °C are shown in **Fig. 4.14A**. As indicated above, the resistances increased to 194, 205 and 213 Ω after 100, 200 and 300 cycles, respectively. This tiny resistance change indicated the excellent interfacial compatibility of this CPE with the electrodes. **Fig. 4.14B** shows the SEM image of the sandwich-type CPE membrane surface after the 300-cycle test. It is difficult to differentiate the interface between $\text{PEO}_8\text{-LiTFSI}$ and $\text{PVDF-HFP-15\%LLZTO}$ due to the structural reorganization, and no other significant morphology change after the cycles was observed.

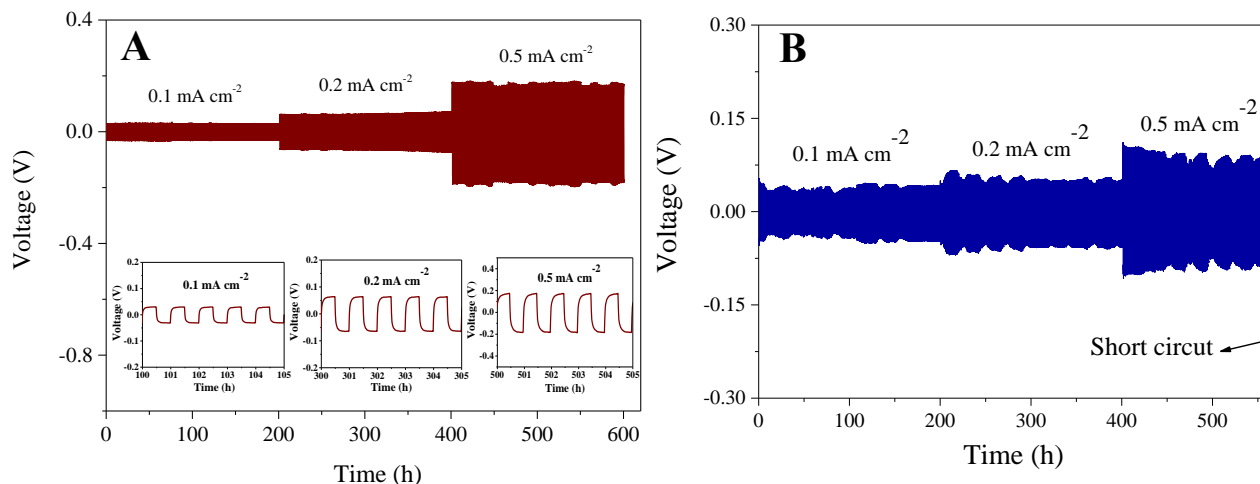


Fig. 4.15 Galvanostatic cycling curves of the (A) Li| sandwich-type CPE |Li and (B) the Li| 1M LiPF₆ in EC: DEC |Li symmetrical cells at different current densities.

In addition, the long-term mechanical stability of sandwich-type CPE membrane against the Li dendrites was further evaluated by using a Li| sandwich-type CPE |Li symmetrical cell, in which Li metal was plated and stripped time after time to mimic a practical cycling process. **Fig. 4.15A** shows the voltage profiles of the cell cycling at current densities of 0.1, 0.2, and 0.5 mA·cm⁻², respectively. The symmetrical cell rendered outstanding cycling stability and low voltage polarization for more than 600 h without a short circuit and rendered a stable loop for more than 5000 min (84 h) even at a current density of around 2 mA cm⁻². In contrast, as shown in **Fig. 4.15B**, the interface was unstable in a routine liquid electrolyte at room temperature, and short circuiting occurred at about 550 h, implying that the sandwich-type CPE effectively suppressed the lithium dendrites.

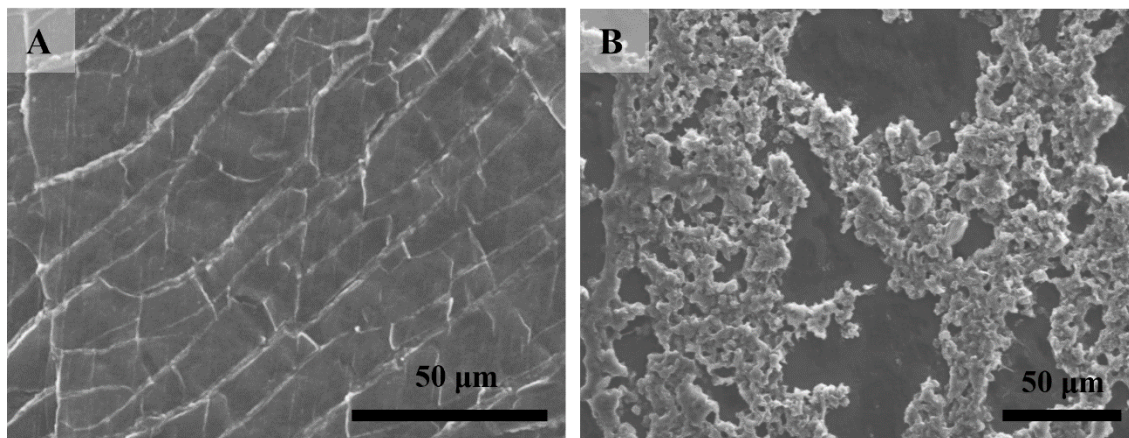


Fig. 4.16 SEM images of surface morphologies for the Li anodes obtained from the $\text{LiFePO}_4|\text{Li}$ cell with (A) $\text{PEO}_8\text{-LiTFSI/PVDF-HFP-15\%LLZTO/PEO}_8\text{-LiTFSI}$ sandwich-type CPE and (B) 1 M $\text{LiPF}_6/(\text{EC: DEC, 1: 1 in volume})$ after 100 cycles at 0.2 C.

Besides, **Fig. 4.16A** shows the surface morphology of the Li metal anode in the $\text{LiFePO}_4|\text{Li}$ cells with the sandwich-type CPE after 100 cycles test. The lithium metal surface with the sandwich-type CPE showed only some cracks during the lithium plating/stripping process owing to the volume expansion, indicating that the sandwich-type CPE effectively hindered the formation of Li dendrites. It is mainly attributed to the intimate contact between the CPE membrane and the electrode and the facilitating effect of the rigid LLZTO particles on the uniform deposition of Li metal during the charging process [53]. In contrast, the surface morphology of the Li metal anode in the $\text{LiFePO}_4|\text{Li}$ cell with the conventional liquid electrolyte of 1 M $\text{LiPF}_6/(\text{EC: DEC, 1: 1 in volume})$ is shown in **Fig. 4.16B**. It is observed that massive Li dendrites grew and accumulated in this case, indicating that the poor quality of this solid electrolyte interphase (SEI) layer did not shield the bulk Li against the electrolyte attacking [54]. As such, once the dendrites maintained growing and reached the cathode, the short-circuiting occurred.

The initial charge-discharge profiles of other two all-solid-state $\text{LiCoO}_2|\text{Li-metal}$ and $\text{LiNi}_{1/3}\text{Co}_{1/3}\text{Mn}_{1/3}\text{O}_2|\text{Li-metal}$ batteries assembled with the sandwich-type CPE membrane at 0.1 C and 40 °C with different cycles are shown in **Fig. 4.17** Both cells also showed the high-voltage stability, delivering capacities of 135.08 and 130.49 mAh g⁻¹ after 60 and 80 cycles respectively with coulombic efficiencies around 97%. The lower coulombic efficiencies of high-voltage cathodes cycled with the sandwich-type CPE membrane can be attributed to the following factors: firstly, as shown in Table S1, the electrode density of LiCoO_2 (2.89 g cm⁻³) and $\text{LiNi}_{1/3}\text{Mn}_{1/3}\text{Co}_{1/3}\text{O}_2$ (2.75 g cm⁻³) were higher than that of LiFePO_4 (1.66 g cm⁻³), and the ion diffusion limitation generally increases with the increase in the electrode density, causing a little lower discharge capacity and coulombic efficiency. Moreover, the PEO polymer skin layers of sandwich-type CPE could be slowly oxidized at 4.2 V and diffused across the porous SEI layer, leading to a little loss of lithium from the cathode [22, 34]. To solve this issue, the polymer skin layer with higher stability and wettability is required. Meanwhile, it should be noted that the capacity retentions of both cells remained more than 94% with different cycles. As mentioned above, these excellent performances could be resulted from the copolymer chains between PVDF-HFP and PEO, which enabled to form a stable CPE/electrodes interface. Herein, as indicated by Chen et al.[24], the intermolecular hydrogen bonding effect between PVDF-HFP and PEO could enable polymer chains to be more disordered in the copolymer, which helped to form a 3D porous polymer network and as a result, all the PVDF-HFP-PEO copolymers with different PEO contents exhibited higher ionic conductivity than the pure PVDF-HFP. Thus, in this study, it is considered that the PVDF-HFP-PEO copolymer should be also formed at the interfaces during the same drying and pressing treatment processes. Meanwhile, some functional groups of PVDF-HFP with a strong electron withdrawing effect could suppress the decomposition of the PEO electrolyte by

oxidation. As seen in **Fig. 4.17B, D**, lower discharge capacities also apparently appeared in the first few cycles as the LiFePO_4 |sandwich-type CPE |Li-metal battery.

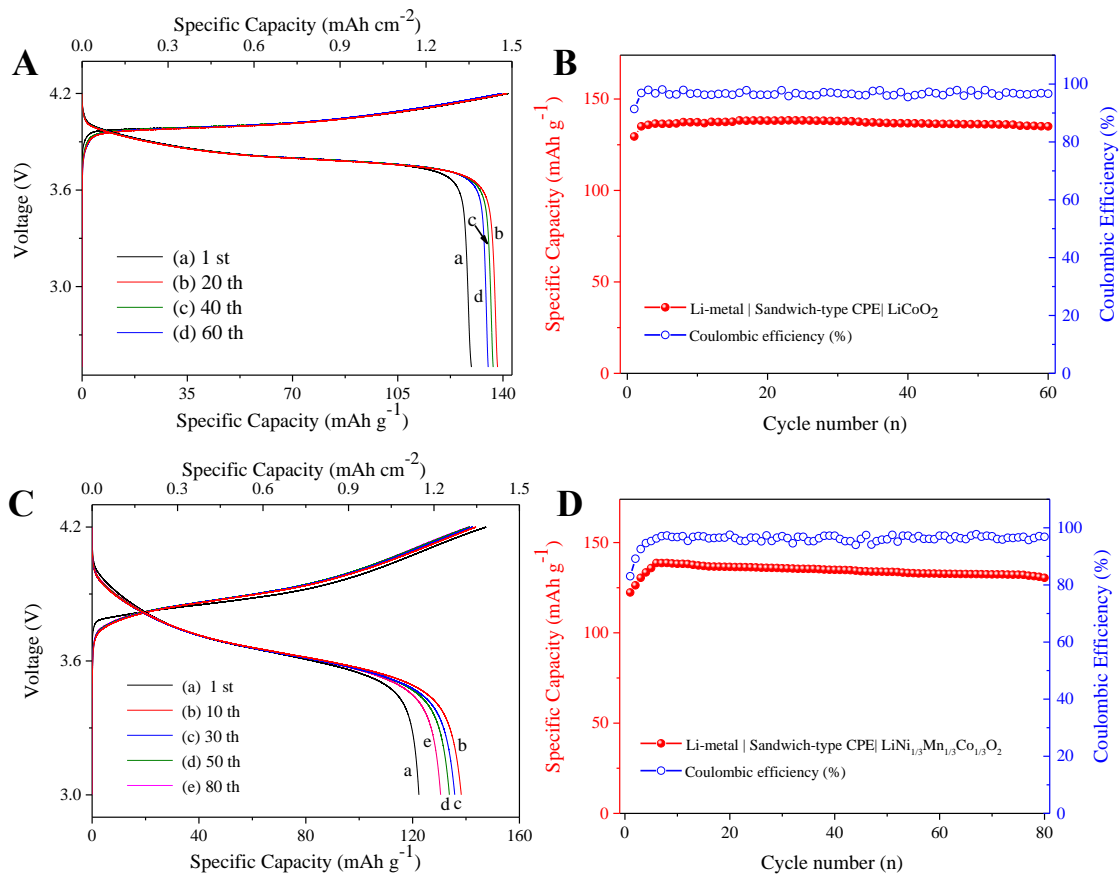


Fig. 4.17 Typical charge-discharge curves and cycling stability of all-solid-state (**A, B**) LiCoO_2 |Li-metal and (**C, D**) $\text{LiNi}_{1/3}\text{Mn}_{1/3}\text{Co}_{1/3}\text{O}_2$ |Li-metal cells with the sandwich-type CPE at 0.1 C and 40 °C.

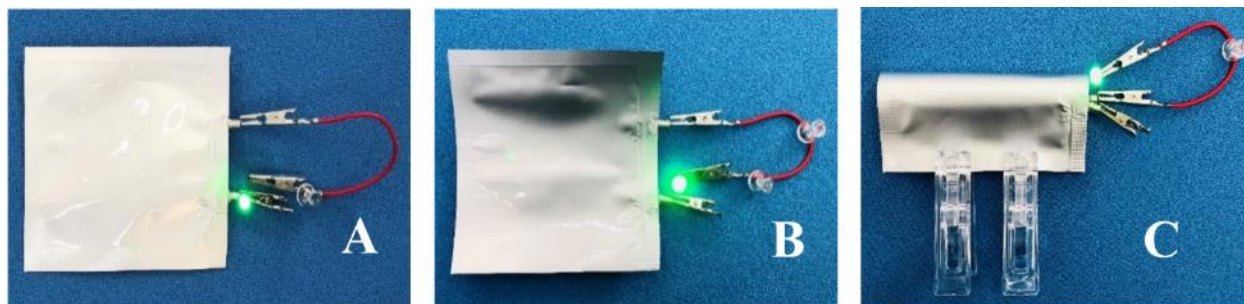


Fig. 4.18 All-solid-state pouch $\text{LiFePO}_4|\text{Li}$ metal cell assembled with sandwich-type CPE to light the LED at (A) flat state, (B) bending, and (C) folding states at room temperature.

As shown in **Fig. 4.18**, a pouch $\text{LiFePO}_4|\text{Li}$ metal cell with the sandwich-type CPE membrane also maintained the capability of lighting the LED device before and after several bending tests, indicating that it was also suitable for the flexibility requirements owing to the intimate contact between the CPE membrane and electrodes. All in all, this sandwich-type CPE not only stabilized the Li metal anode, suppressed Li dendrite growth to enhance the safety of ASSLMBs, but also had high potential to the flexible and wearable electronics.

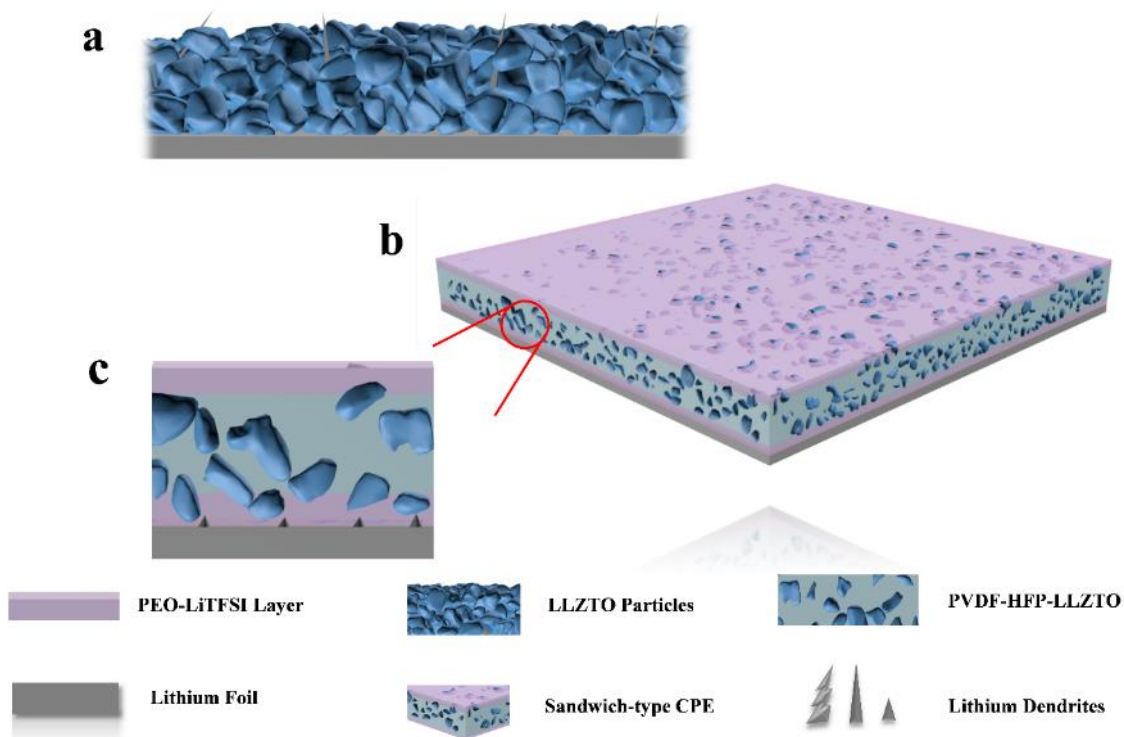


Fig. 4.19 A schematic diagram of (a) the garnet LLZTO electrolyte with massive Li dendrites growth, (b) structure of the sandwich-type CPE with a flat Li anode surface and (c) the contact behavior of sandwich-type CPE with Li metal.

According to above study, the interface engineering strategy for the batteries with such a sandwich SPE is shown in **Fig. 4.19**. In general, with an individual LLZTO electrolyte membrane, during the charging process, the Li^+ ions are plated preferentially on the ceramic grain boundaries and the interconnected pores of ceramic electrolyte where the Li-ion flux is locally enhanced under an electric field. The Li/Li symmetric cell using such a ceramic as the electrolyte identified that the Li lithium dendrites always grow through the electrolyte layer, resulting in short circuited in only 20 h [34, 55]. Meanwhile, the strong mechanical strength and discontinuity on the electrolyte surface of PVDF-HFP-LLZTO CPE may not only cause the contact loss with electrodes and local current density amplification, but also give an inhomogeneous Li^+ flux across the interface with the Li dendrite formation. In this case, as the PEO-LiTFSI polymer layers are coated on the both sides of PVDF-HFP-LLZTO CPE, the contacts between the sandwich-type CPE and the electrodes could be improved, accompanying with the significant decrease of the interfacial resistance and the increase of the mechanical strength of the CPE, which will be beneficial for suppressing the Li dendrite growth in the ASSLMs. As a result, **Table 4.2** compares the results obtained in this study with those reported PVDF-HFP-based electrolytes with LiFePO_4 cathode in the Li metal batteries. One can see that this sandwich-type CPE had good performance and stability even when worked with a much high areal capacity cathode. Thus, benefited from the sandwiched polymer/ceramic/polymer electrolyte structure design [34], as discussed above, it has the advantages such as enhanced ionic conductivity, lowered interfacial impedance, improved electrolyte/electrode compatibility, suppressed Li dendrites growth, and satisfied high-voltage stability, resulting in excellent cell performance.

Table 4.2 Comparison of PVDF-HFP-based electrolyte for Li metal batteries.

Electrolyte	Electrolyte state	Areal Capacity (mAh cm ⁻²)	Discharge Capacity (mAh g ⁻¹)	Cycles (n)	Ref
PVDF-HFP-SLCE ^a	Gel	NG ^f	144.1 (0.1 C)	100	[56]
PVDF-HFP-TiO ₂ - LiTFSI-Py13TFSI ^b	Gel	0.7	140 (0.1 C)	600	[57]
PVDF-HFP-Li ₇ La ₃ Zr ₂ O ₁₂ + LE ^c	Solid-Liquid	0.31	136.6 (0.2 C)	200	[28]
PVDF-HFP-MEP + LE ^d	Solid-Liquid	NG	71 (0.2 C)	200	[29]
PVDF-HFP-Li ₇ La ₃ Zr ₂ O ₁₂ + LE ^e	Solid-Liquid	0.4	111 (0.5 C)	200	[33]
PVDF-HFP-Li _{6.5} La ₃ Zr _{1.5} Ta _{0.5} O ₁₂ + LE ^f	Solid-Liquid	0.255	110.9 (0.5 C)	500	[58]
Sandwich-type CPE	Solid	1.5	120.01 (0.2 C)	300	This work

^a: poly (1-[(2-methacryloyloxy) propyl]-3-butylimidazolium bromide)-LiTFSI-1-ethyl-3-methylimidazolium bis (trifluoromethylsulfonyl)imide (SLCE); ^b: N-methyl-N-propylpyrrolidinium bis(trifluoromethanesulfonyl)imide (Py13TFSI); ^c: 1.0 M LiPF₆ in EC/ DEC (LE); ^d: Poly(etheramine)- glycidylxypropyl)trimethoxysilane-polyetherdiamine-poly(ethyleneglycol)diglycidylether (MEP), 1.0 M LiPF₆ in EC/ DEC (LE); ^e: 1 M LiTFSI in Tetraethylene glycol dimethyl ether (LE); ^f: Not Given (NG). ^f: LiPF₆, EC/DEC/DMC=1:1:1 (LE).

4.4 Conclusions

In summary, a novel sandwich-type CPE membrane, PEO₈-LiTFSI/PVDF-HFP-15%LLZTO/PEO₈-LiTFSI membrane, is successfully fabricated and applied in the ASSLMBs. It is found that the PEO-LiTFSI layers in two sides of the PVDF-HFP-LLZTO membrane ameliorated the ion conductivity, improved the intimate contact with the electrodes and suppressed the lithium dendrite growth for stabilizing the battery. Meanwhile, the crystallinity of PEO and PVDF-HFP polymer matrix also reduced greatly owing to the cross-linking between each other at the interfacial sections. With the synergistic effects of ceramics electrolyte filler and the low-

crystallinity polymer matrix, the faster Li^+ ions transportation ability of the CPE was obtained. As a result, the sandwich-type CPE membrane revealed a satisfied ionic conductivity of $3.3 \times 10^{-4} \text{ S} \cdot \text{cm}^{-1}$, a wide electrochemical window of over 5.0 V and a high t_{Li^+} of 0.52 at 40 °C. Moreover, the all-solid-state LiFePO_4 |sandwich-type CPE|Li-metal battery with a high areal capacity cathode (1.5 mAh cm^{-2}) exhibited excellent rate performance, high coulombic efficiency and long-term cycle stability with negligible discharge capacity decay from 100 to 300 cycles at 40 °C. Furthermore, the fabricated flexible pouch cell also had excellent performance. Meanwhile, the all-solid-state LiCoO_2 (1.5 mAh cm^{-2})|Li-metal and $\text{LiNi}_{1/3}\text{Mn}_{1/3}\text{Co}_{1/3}\text{O}_2$ (1.5 mAh cm^{-2})|Li-metal battery assembled with this sandwich-type CPE membrane also exhibited high-voltage stability along with a satisfied energy density, indicating that this sandwich-type CPE membrane had a high potential to be applied in the next generation ASSLMs.

References

- [1] Q. Yang, Z. Zhang, X.G. Sun, Y.S. Hu, H. Xing, S. Dai, Ionic liquids and derived materials for lithium and sodium batteries, *Chem. Soc. Rev.* 47 (2018) 2020–2064.
- [2] Y.B. Kim, I.T. Kim, M.J. Song, M.W. Shin, Synthesis of a polyacrylonitrile/tetrachloro-1, 4-benzoquinone gel polymer electrolyte for high-performance Li-air batteries, *J. Membr. Sci.* 563 (2018) 835-842.
- [3] Z. Zhang, Y. Shao, B. Lotsch, Y. Hu, L.F. Nazar, C. Nan, J. Maier, M. Armand, L. Chen, New horizons for inorganic solid state ion conductors, *Energy Environ. Sci.* 11 (2018) 1945–1976.
- [4] X.B. Cheng, R. Zhang, C.Z. Zhao, F. Wei, J.G. Zhang, Q. Zhang, A review of solid electrolyte interphases on lithium metal anode, *Adv. Sci.* 3 (2016) 1500213.
- [5] N. Kamaya, K. Homma, Y. Yamakawa, M. Hirayama, R. Kanno, M. Yonemura, T. Kamiyama, Y. Kato, S. Hama, K. Kawamoto, A. Mitsui, A lithium superionic conductor,

- Nat. Mater. 10 (2011) 682–686.
- [6] Q. Liu, Z. Geng, C. Han, Y. Fu, S. Li, Y. B. He, F. Kang, B. Li, Challenges and perspectives of garnet solid electrolytes for all solid-state lithium batteries, *J. Power Sources* 389 (2018) 120–134.
 - [7] P. Lun, P. Liu, H. Lin, Z. Dai, Z. Zhang, D. Chen, Ionic conductivity promotion of polymer membranes with oxygen-ion conducting nanowires for rechargeable lithium batteries, *J. Membr. Sci.* 580 (2019) 92–100.
 - [8] J. Hu, W. Wang, B. Zhou, Y. Feng, X. Xie, Z. Xue, Poly (ethylene oxide)-based composite polymer electrolytes embedding with ionic bond modified nanoparticles for all-solid-state lithium-ion battery, *J. Membr. Sci.* 575 (2019) 200–208.
 - [9] Z. Xie, Z. Wu, X. An, A. Yoshida, Z. Wang, X. Hao, A. Abudula, G. Guan, Bifunctional ionic liquid and conducting ceramic co-assisted solid polymer electrolyte membrane for quasi solid-state lithium metal batteries, *J. Membr. Sci.* 586 (2019) 122–129.
 - [10] Z. Wu, Z. Xie, A. Yoshida, Z. Wang, X. Hao, A. Abudula, G. Guan, Utmost limits of various solid electrolytes in all-solid-state lithium batteries: A critical review, *Renewable Sustainable Energy Rev.* 109 (2019) 367–385.
 - [11] X. Zhang, T. Liu, S. Zhang, X. Huang, B. Xu, Y. Lin, B. Xu, L. Li, C.W. Nan, Y. Shen, Synergistic coupling between $\text{Li}_{6.75}\text{La}_3\text{Zr}_{1.75}\text{Ta}_{0.25}\text{O}_{12}$ and poly(vinylidene fluoride) induces high ionic conductivity, mechanical strength, and thermal stability of solid composite electrolytes, *J. Am. Chem. Soc.* 139 (2017) 13779–13785.
 - [12] W. Chen, T. Lei, C. Wu, M. Deng, C. Gong, K. Hu, Y. Ma, L. Dai, W. Lv, W. He, X. Liu, J. Xiong, C. Yan, Designing safe electrolyte systems for a high-stability lithium-sulfur battery, *Adv. Energy Mater.* 8 (2018) 1702348.
 - [13] J. Zhang, N. Zhao, M. Zhang, Y. Li, P.K. Chu, X. Guo, Z. Di, X. Wang, H. Li, Flexible and

- ion-conducting membrane electrolytes for solid-state lithium batteries: dispersion of garnet nanoparticles in insulating polyethylene oxide, *Nano Energy* 28 (2016) 447–454.
- [14] R.J. Chen, Y.B. Zhang, T. Liu, B.Q. Xu, Y.H. Lin, C.W. Nan, Y. Shen, Addressing the interface issues in all-solid-state bulk-type lithium ion battery via an all-composite approach, *ACS Appl. Mater. Inter.* 9 (2017) 9654–9661.
- [15] Y. Jin, K. Liu, J. Lang, D. Zhuo, Z. Huang, C.Wang, H. Wu, Y. Cui, An intermediate temperature garnet-type solid electrolyte-based molten lithium battery for grid energy storage, *Nat. Energy* 3 (2018) 732–738.
- [16] J. Shi, Y. Yang, H. Shao, Co-polymerization and blending based PEO/PMMA/P(VDF-HFP) gel polymer electrolyte for rechargeable lithium metal batteries, *J. Membr. Sci.* 547 (2018) 1–10.
- [17] J. Mindemark, M. J. Lacey, T. Bowden, D. Brandell, Beyond PEO—alternative host materials for Li⁺-conducting solid polymer electrolytes, *Prog. Polym. Sci.* 81 (2018) 114–143.
- [18] O. Sheng, C. Jin, J. Luo, H. Yuan, H. Huang, Y. Gan, J. Zhang, Y. Xia, C. Liang, W. Zhang, X. Tao, Mg₂B₂O₅ nanowire enabled multifunctional solid-state electrolytes with high ionic conductivity, excellent mechanical properties, and flame-retardant performance, *Nano Lett.* 18 (2018) 3104–3112.
- [19] H. Li, M. Li, S.H. Siyal, M. Zhu, J.-L. Lan, G. Sui, Y. Yu, W. Zhong, X. Yang, A sandwich structure polymer/polymer-ceramics/polymer gel electrolytes for the safe, stable cycling of lithium metal batteries, *J. Membr. Sci.* 555 (2018) 169–176.
- [20] Y. Zhao, C. Wu, G. Peng, X. Chen, X. Yao, Y. Bai, F. Wu, S. Chen, X. Xu, A new solid polymer electrolyte incorporating Li₁₀GeP₂S₁₂ into a polyethylene oxide matrix for all-solid-state lithium batteries, *J. Power Sources* 301 (2016) 47–53.

- [21] W. Zhou, Z. Wang, Y. Pu, Y. Li, S. Xin, X. Li, J. Chen, J. B. Goodenough, Double-layer polymer electrolyte for high-voltage all-solid-state rechargeable batteries, *Adv. Mater.* 31 (2018) 1805574.
- [22] J. Ma, Z. Liu, B. Chen, L. Wang, L. Yue, H. Liu, J. Zhang, Z. Liu, G. Cui, A strategy to make high voltage LiCoO₂ compatible with polyethylene oxide electrolyte in all-solid-state lithium ion batteries, *J. Electrochem. Soc.* 164 (2017) A3454-A3461.
- [23] Z. P. Wan, D. N. Lei, W. Yang, C. Liu, K. Shi, X. G. Hao, L. Shen, W. Lv, B. H. Li, Q. H. Yang, F. Y. Kang, Y. B. He, Low resistance-integrated all-solid-state battery achieved by Li₇La₃Zr₂O₁₂ nanowire upgrading polyethylene oxide (PEO) composite electrolyte and PEO cathode binder, *Adv. Funct. Mater.* 29 (2019) 1805301.
- [24] G. H. Chen, F. Zhang, Z. M. Zhou, J. R. Li, Y. B. Tang, A flexible dual-ion battery based on PVDF-HFP-modified gel polymer electrolyte with excellent cycling performance and superior rate capability, *Adv. Energy Mater.* 8 (2018) 1801219.
- [25] H.T.T. Le, D.T. Ngo, R.S. Kalubarme, G. Cao, C.N. Park, C.J. Park, Composite gel polymer electrolyte based on poly (vinylidene fluoride-hexafluoropropylene) (PVDF-HFP) with modified aluminum-doped lithium lanthanum titanate (A-LLTO) for high-performance lithium rechargeable batteries, *ACS Appl. Mater. Inter.* 8 (2016) 20710–20719.
- [26] H. Jia, H. Onishi, N. Von Aspern, U. Rodehorst, K. Rudolf, B. Billmann, R. Wagner, M. Winter, I. Cekic-laskovic, A propylene carbonate based gel polymer electrolyte for extended cycle life and improved safety performance of lithium ion batteries, *J. Power Sources* 397 (2018) 343–351.
- [27] M. Park, S. Hyun, S. Nam, S. Back, Performance evaluation of printed LiCoO₂ cathodes with PVDF-HFP gel electrolyte for lithium ion microbatteries, *Electrochim. Acta* 53 (2008) 5523–5527.

- [28] Y.F. Liang, S.J. Deng, Y. Xia, X.L. Wang, X.H. Xia, J.B. Wu, C.D. Gu, J.P. Tu, A superior composite gel polymer electrolyte of $\text{Li}_7\text{La}_3\text{Zr}_2\text{O}_{12}$ -poly (vinylidene fluoride-hexafluoropropylene) (PVDF-HFP) for rechargeable solid-state lithium ion batteries, *Mater. Res. Bull.* 102 (2018) 412–417.
- [29] D. Saikia, S. Ho, Y. Chang, J. Fang, L. Tsai, Blending of hard and soft organic–inorganic hybrids for use as an effective electrolyte membrane in lithium-ion batteries, *J. Membr. Sci.* 503 (2016) 59–68.
- [30] Y. Xia, X. Wang, X. Xia, R. Xu, S. Zhang, J. Wu, Y. Liang, C. Gu, J. Tu, A newly designed composite gel polymer electrolyte based on poly(vinylidene fluoride-hexafluoropropylene) (PVDF-HFP) for enhanced solid-state lithium-sulfur batteries, *Chem. Eur. J.* 23 (2017) 15203–15209.
- [31] Y. Xia, Y.F. Liang, D. Xie, X.L. Wang, S.Z. Zhang, X.H. Xia, C.D. Gu, J.P. Tu, A poly (vinylidene fluoride-hexafluoropropylene) based three-dimensional network gel polymer electrolyte for solid-state lithium-sulfur batteries, *Chem. Eng. J.* 358 (2019) 1047–1053.
- [32] N. Yadav, K. Mishra, S.A. Hashmia, Optimization of porous polymer electrolyte for quasi-solid-state electrical double layer supercapacitor, *Electrochim. Acta* 235 (2017) 570–582.
- [33] W. Zhang, J. Nie, F. Li, Z. L. Wang, C. Sun, A durable and safe solid-state lithium battery with a hybrid electrolyte membrane, *Nano Energy* 45 (2018) 413–419.
- [34] W. Zhou, S. Wang, Y. Li, S. Xin, A. Manthiram, J.B. Goodenough, Plating a dendrite-free lithium anode with a polymer/ceramic/polymer sandwich electrolyte, *J. Am. Chem. Soc.* 138 (2016) 9385–9388.
- [35] J. Xi, X. Qiu, J. Li, X. Tang, W. Zhu, L. Chen, PVDF–PEO blends based microporous polymer electrolyte: Effect of PEO on pore configurations and ionic conductivity, *J. Power Sources* 157 (2006) 501–506.

- [36] X.X. Zeng, Y.X. Yin, N.W. Li, W.C. Du, Y.G. Guo, L.J. Wan, Reshaping lithium plating/stripping behavior via bifunctional polymer electrolyte for room-temperature solid Li metal batteries, *J. Am. Chem. Soc.* 138 (2016) 15825–15828.
- [37] N. W. Li, Y. X. Yin, C. P. Yang, Y. G. Guo, An artificial solid electrolyte interphase layer for stable lithium metal anodes, *Adv. Mater.* 28 (2016) 1853-1858.
- [38] Z. Tu, Y. Kambe, Y. Lu, L. A. Archer, Nanoporous polymer-ceramic composite electrolytes for lithium metal batteries, *Adv. Energy Mater.* 4 (2014) 1300654.
- [39] Y. Chen, Y. Tian, Z. Li, N. Zhang, D. Zeng, G. Xu, Y. Zhang, Y. Sun, H. Ke, H. Cheng, An AB alternating diblock single ion conducting polymer electrolyte membrane for all-solid-state lithium metal secondary batteries, *J. Membr. Sci.* 566 (2018) 181-189.
- [40] L. Pan, H. Huang, M. Zhong, M. Niederberger, Hydrogel-derived foams of nitrogen-doped carbon loaded with Sn nanodots for high-mass-loading Na-ion storage, *Energy Storage Mater.* 16 (2019) 519–526.
- [41] P. Albertus, S. Babinec, S. Litzelman, A. Newman, Status and challenges in enabling the lithium metal electrode for high-energy and low-cost rechargeable batteries, *Nat. Energy* 3 (2018) 16–21.
- [42] J. Liu, Z. Bao, Y. Cui, E.J. Dufek, J.B. Goodenough, P. Khalifah, Q. Li, B.Y. Liaw, P. Liu, A. Manthiram, Y.S. Meng, V.R. Subramanian, M.F. Toney, V. V Viswanathan, M.S. Whittingham, J. Xiao, W. Xu, J. Yang, X. Q. Yang, J.G. Zhang, Pathways for practical high-energy long-cycling lithium metal batteries, *Nat. Energy* 4 (2019) 180–186.
- [43] H. Li, Practical evaluation of Li-ion batteries, *Joule* 3 (2019) 908-919.
- [44] P. Prabakaran, R.P. Manimuthu, Enhancement of the electrochemical properties with the effect of alkali metal systems on PEO/PVdF-HFP complex polymer electrolytes, *Ionics* 22 (2016) 827-839.

- [45] C.Z. Zhao, X.Q. Zhang, X.B. Cheng, R. Zhang, R. Xu, P.Y. Chen, H.J. Peng, J.Q. Huang, Q. Zhang, An anion-immobilized composite electrolyte for dendrite-free lithium metal anodes, *Proc. Natl. Acad. Sci.* 114(2017) 11069-11074.
- [46] T. Krauskopf, H. Hartmann, W.G. Zeier, J. Janek, Krauskopf, Toward a fundamental understanding of the lithium metal anode in solid state batteries-an electrochemo-mechanical study on the garnet-type solid Electrolyte $\text{Li}_{6.25}\text{Al}_{0.25}\text{La}_3\text{Zr}_2\text{O}_{12}$, *ACS Appl. Mater. Inter.* 11 (2019) 14463–14477.
- [47] Y.C. Jung, S.M. Lee, J.H. Choi, S.S. Jang, D.W. Kim, All solid-state lithium batteries assembled with hybrid solid electrolytes, *J. Electrochem. Soc.* 162 (2015) A704–A710.
- [48] A. Samuthira, X.C. Chen, J. Chen, B.S. Lokitz, R.E. Ruther, G. Yang, K. Lou, J. Nanda, F.M. Delnick, N.J. Dudney, Facile and scalable fabrication of polymer-ceramic composite electrolyte with high ceramic loadings, *J. Power Sources* 390 (2018) 153–164.
- [49] X. Zhang, B.Q. Xu, Y.H. Lin, Y. Shen, L. Li, C.W. Nan, Effects of $\text{Li}_{6.75}\text{La}_3\text{Zr}_{1.75}\text{Ta}_{0.25}\text{O}_{12}$ on chemical and electrochemical properties of polyacrylonitrile-based solid electrolytes, *Solid State Ionics* 327 (2018) 32–38.
- [50] B. Sun, J. Mindemark, K. Edström, D. Brandell, Realization of high performance polycarbonate-based Li polymer batteries, *Electrochem. Commun.* 52 (2015) 71–74.
- [51] L. Balo, Shalu, H. Gupta, V. Kumar Singh, R. Kumar Singh, Flexible gel polymer electrolyte based on ionic liquid EMIMTFSI for rechargeable battery application, *Electrochim. Acta* 230 (2017) 123–131.
- [52] L. Han, Z. Wang, D. Kong, L. Yang, K. Yang, Z. Wang, F. Pan, An ordered mesoporous silica framework based electrolyte with nanowetted interfaces for solid-state lithium batteries, *J. Mater. Chem. A* 6 (2018) 21280–21286.
- [53] M. Keller, G.B. Appetecchi, G.T. Kim, V. Sharova, M. Schneider, J. Schuhmacher, A.

- Roters, S. Passerini, Electrochemical performance of a solvent-free hybrid ceramic-polymer electrolyte based on $\text{Li}_7\text{La}_3\text{Zr}_2\text{O}_{12}$ in P (EO)₁₅LiTFSI, *J. Power Sources* 353 (2017) 287–297.
- [54] J. Zheng, M.H. Engelhard, D. Mei, S. Jiao, B.J. Polzin, J. -G. Zhang, W. Xu, Electrolyte additive enabled fast charging and stable cycling lithium metal batteries, *Nat. Energy* 2 (2017) 17012.
- [55] Y. Ren, Y. Shen, Y. Lin, C. W. Nan, Direct observation of lithium dendrites inside garnet-type lithium-ion solid electrolyte, *Electrochem. Commun.* 57 (2015) 27–30.
- [56] M. Que, Y. Tong, G. Wei, K.Y uan, J. Wei, Y. Jiang, H. Zhu, Y. Chen, Safe and flexible ion gel based composite electrolyte for lithium batteries, *J. Mater. Chem. A* 4 (2016) 14132–14140.
- [57] N. Chen, Y. Xing, L. Wang, F. Liu, L.Li, R. Chen, F. Wu, S. Guo, “Tai Chi” philosophy driven rigid-flexible hybrid ionogel electrolyte for high-performance lithium battery, *Nano Energy* 47 (2018) 35–42.
- [58] J. Lu, Y. Liu, P. Yao, Z. Ding, Q. Tang, J. Wu, Z. Ye, K. Huang, X. Liu, Hybridizing poly (vinylidene fluoride-co-hexafluoropropylene) with $\text{Li}_{6.5}\text{La}_3\text{Zr}_{1.5}\text{Ta}_{0.5}\text{O}_{12}$ as a lithium-ion electrolyte for solid state lithium metal batteries, *Chem. Eng. J.* 367 (2019) 230–238.

Chapter 5 Novel electrolyte additive assisted commercial electrolyte for long cycle life lithium metal batteries

5.1 Introduction

The Nobel Prize in Chemistry 2019 rewarded the development of the lithium-ion battery. This rechargeable battery is now widely used from the mobile phone to the laptop and electric vehicle. It can also store energy from renewable energy such as solar and wind powers, making a fossil fuel-free society possible. However, its energy storage ability, long-term stability and safety are still needed to be improved [1]. Lithium (Li) metal is always considered as the ideal anode material to improve the energy storage ability since it is a very light metal (0.534 g cm^{-3}) with an ultrahigh specific capacity (3860 mAh g^{-1}) as well as a ultralow standard negative electrochemical potential (-3.040 V) [2]. Unfortunately, Li metal has high reactivity, usually resulting in the dendritic Li growth during the charging/discharging process. Thus, the widespread deployment of high-energy density lithium metal batteries (LMBs) is still seriously impeded [3].

Recently, tremendous efforts have been devoted to the protection and utilization of Li metal, including the applications of solid-state electrolytes [4-6], concentrated electrolytes and ionic liquids [7-8], electrolyte additives [9], protective layers [10], special structure design [11], host matrix [12], and so on. Considering its low cost and easy processing, the electrolyte additive should be the most promising way for the facile improvement of the LMB performance [9, 13-14]. As the electrolyte additive, it should have the ability for not only decreasing the Li nucleation and deposition overpotential but also inducing the generation of a robust and dense solid electrolyte interphase (SEI) layer to effectively suppress the parasitic reactions between Li metal and electrolyte and enhance the transport of Li^+ ions so that the cycling performance of LMBs can be greatly improved. Various electrolyte additives have been applied to improve the performance of

Li metal anode. For instance, carbonate-based additives like fluoroethylene carbonate (FEC) and vinylene carbonate (VC) [15, 16], alkali metal salt-based additives like LiPF_6 and lithium difluoro(oxalate)borate (LiDFOB) [14, 17], ionic liquids like 1-dodecyl-1-methylpyrrolidinium bis(fluorosulfonyl)imide (Pyr1(12)FSI) [18], nitrates-based compounds like $\text{La}(\text{NO}_3)_3$ [19], trace amount of water [20], sulphides and related additives like Li_2S_8 [21], multifunctional additives like tris (2, 2, 2-trifluoroethyl) phosphite [22], and so on.

In our previous study [6], it was confirmed that the pyridine ring-containing compound played a significant role in adjusting the Li^+ ion distribution and enhancing Li^+ ion transference number. Hou *et al.* also proposed that the pyridinic nitrogen with lone-pair electrons can act as Lewis base sites to adsorb Lewis acidic Li ions strongly in electrolytes through acid-base interactions, guiding the metallic Li nuclei to uniformly distribute on the anode surface [23]. Meanwhile, based on our preliminary density functional theory (DFT) calculations, the fluorine atoms on the pyridine ring (fluoropyridine) are easily detached to participate the formation of the SEI during the charging/discharging cycle, demonstrating the same reaction mechanism as the commercial electrolyte additive of fluoroethylene carbonate (FEC) [24]. Therefore, in this study, 2-fluoropyridine (2-FP) was selected as the additive for the modification of routine liquid electrolytes.

Meanwhile, most researchers assembled Li metal anode with the cathode using a low mass amount (less than 1 mAh cm^{-2}) to avoid the ion diffusion limitation in the LMBs [2, 13]. Although such a low content of active materials in the cathode always leads to a very slight Li stripping/plating in the cell for extending the cycle life, the energy density of LMBs was too low, limiting the practical application in a portable device. As for higher cathode areal capacity, more utilization of Li metal in each deposition/stripping process is always required. However, the high cathode areal capacity could generate deep parasitic side reactions, resulting in fast capacity fading. To solve this problem, more rigorous electrolyte stability with such a cathode is necessary.

Furthermore, in the case of a high charge current density, a quick corrosion of Li metal will occur, also result in a faster capacity fading of LMBs. Meanwhile, a high voltage of cathode also needs the more stable electrolyte with the anode [25]. In addition, the electrolyte amount can greatly affect the cycling performance of LMBs. For instance, the optimum amount of electrolyte used in a practical pouch cell with a specific energy of more than 300 Wh kg⁻¹ was suggested to be about 3 g Ah⁻¹ [3]. However, in most lab-scale experiments, the electrolyte amount of a coin-cell LMB with a long lifetime was always in an overflow state [26], which cannot satisfy a practical pouch cell. Therefore, an ideal LMB should have a high energy density cathode with a large cathode mass loading amount, a reduced amount of electrolyte, a suitable negative/positive electrode areal capacity ratio (N/P ratio), and a limited excess amount of Li metal [2, 27].

In the present study, to obtain the improved interfacial compatibility, lower nucleation overpotential, more robust SEI layer, and more uniform dendrite-free Li deposition for achieving the safe and stable LMBs, 2-Fluoropyridine (2-FP) containing the pyridine ring, which has never been used as the electrolyte additive, was selected to modify the commercial carbonate-based and ether-based electrolytes, and its performance was evaluated in the LMB cells assembled with the high-voltage cathode having a large mass loading amount and the lean electrolyte working at a high current density. In addition, DFT calculations were also used to understand the stabilization effect by introduction of this additive at the extreme condition.

5.2 Experimental

5.2.1 Cell assembly and measurement

Based on preliminary experiments, for different commercial liquid electrolytes, the 2-FP electrolyte additive-to-lithium salt (1 M) molar ratio of 2: 100, entitled as 2% of 2-FP electrolyte additive, was selected. All the charge/discharge performances were measured using CR2032-type coin cells with a Celgard 2400 polypropylene (PP) separator containing 30 μ L electrolyte on a

Wuhan LAND batteries testing system CT2001A. The Li|Cu cells were tested at a current density of 0.5 mA cm^{-2} for 2 h. In each cycle, the metallic Li (equal to 1.0 mAh cm^{-2}) was deposited onto the Cu substrate during discharging process, then the cells were charged to the cut-off voltage of 0.5 V (vs. Li^+/Li) at the same current, and all the cells were cycled at a current density of 0.15 mA cm^{-2} for first formation cycle. The Li|Li symmetric cells were galvanostatically tested at a current density of 1 mA cm^{-2} with time-controlled charge/discharge cycles. In each cycle, 1 mA h cm^{-2} metallic Li was deposited and striped on the electrodes. The $\text{LiNi}_{1/3}\text{Mn}_{1/3}\text{Co}_{1/3}\text{O}_2$ |Li metal cells and the Li| LiFePO_4 cells were also galvanostatically tested at room temperature over the voltage range of 2.7-4.3 V and 2.5-4.0 V, respectively. The $\text{LiNi}_{1/3}\text{Mn}_{1/3}\text{Co}_{1/3}\text{O}_2$ |Li metal cells were firstly cycled at 0.1 C (1 C = 1.5 mA cm^{-2} , based on $\text{LiNi}_{1/3}\text{Mn}_{1/3}\text{Co}_{1/3}\text{O}_2$ materials) for three formation cycles and the cycled at 0.5 C in the cycling performance test. The LiFePO_4 |Li metal cells were firstly cycled at 0.5 C (1 C = 1.5 mA cm^{-2} , based on LiFePO_4 materials) for 5 cycles and then the cycled at 1 C in the cycling performance test. Electrochemical impedance spectroscopy (EIS) measurement of cells were obtained from the AC impedance measurement with the frequency between 1 MHz and 0.01 Hz with an amplitude of 5 mV on a Princeton electrochemical station VersaSTAT 4.

5.2.2 Cell characterizations and analysis

The cycled $\text{LiNi}_{1/3}\text{Mn}_{1/3}\text{Co}_{1/3}\text{O}_2$ |Li metal and LiFePO_4 |Li metal cells with different electrolytes were disassembled in the argon-filled glove box at first. Prior to any characterizations, the Li metal anodes with the liquid electrolyte were rinsed using dimethyl carbonate to remove the residual electrolyte and lithium salt and then dried in the glove box at ambient temperature. The morphologies of Li metal electrodes were observed via a SEM (Hitachi SU8010) system. The compositions of surface film including the SEI layer on the Li anode were measured by XPS technology, and the contents of different species in the SEI layers were obtained by fitting the

whole XPS spectra using CasaXPS software. During the transfer process, all the samples were protected with Ar to avoid contact with air. Contact angle measurement was carried out by using a contact angle meter (DMe-201, Kyowa Interface Science).

5.2.3 Computational details

The energy levels of the highest occupied molecule orbital (HOMO) and lowest unoccupied molecular orbital (LUMO) of the organic solvents of EC, DEC, DOL, DME, Pyridine, and 2-FP were calculated with the DMOL3 module included in the Accelrys Material Studio software package. Simultaneously, the binding energy (E_b) between the organic solvent and lithium ion was also calculated using the COSMO continuum solvation model of DMOL3 module in Material Studio. The binding energy (E_b) was defined as following: $E_b = E_{\text{combine}} - E_{\text{solvents}} - E_{\text{Li ion}}$, where E_{combine} , E_{solvents} , and $E_{\text{Li ion}}$ are the total energies of the solvents-Li ion complex, the solvents, and Li ion, respectively. The dielectric constant parameters of EC/DEC (1:1 vol.%) and DOL/DME (1:1 vol.%) solvents were 35 and 7.6, respectively.

5.3 Results and discussion

5.3.1 DFT calculations and wettability analysis

It is well known that the reduction potential of electrolyte additive is one of the key factors to determine whether it can be used to tailor the properties of the passivation layer on the surface of anode[17]. Based on the frontier molecular orbital theory, the electrochemical oxidation/reduction potential of organic molecule is closely related to its highest occupied molecule orbital (HOMO)/lowest unoccupied molecularorbital (LUMO) energy. Generally, the greater the HOMO energy of the molecule, the more easily it is oxidized; meanwhile, the lower the LUMO energy of the molecule, the more easily it is reduced [28, 29].

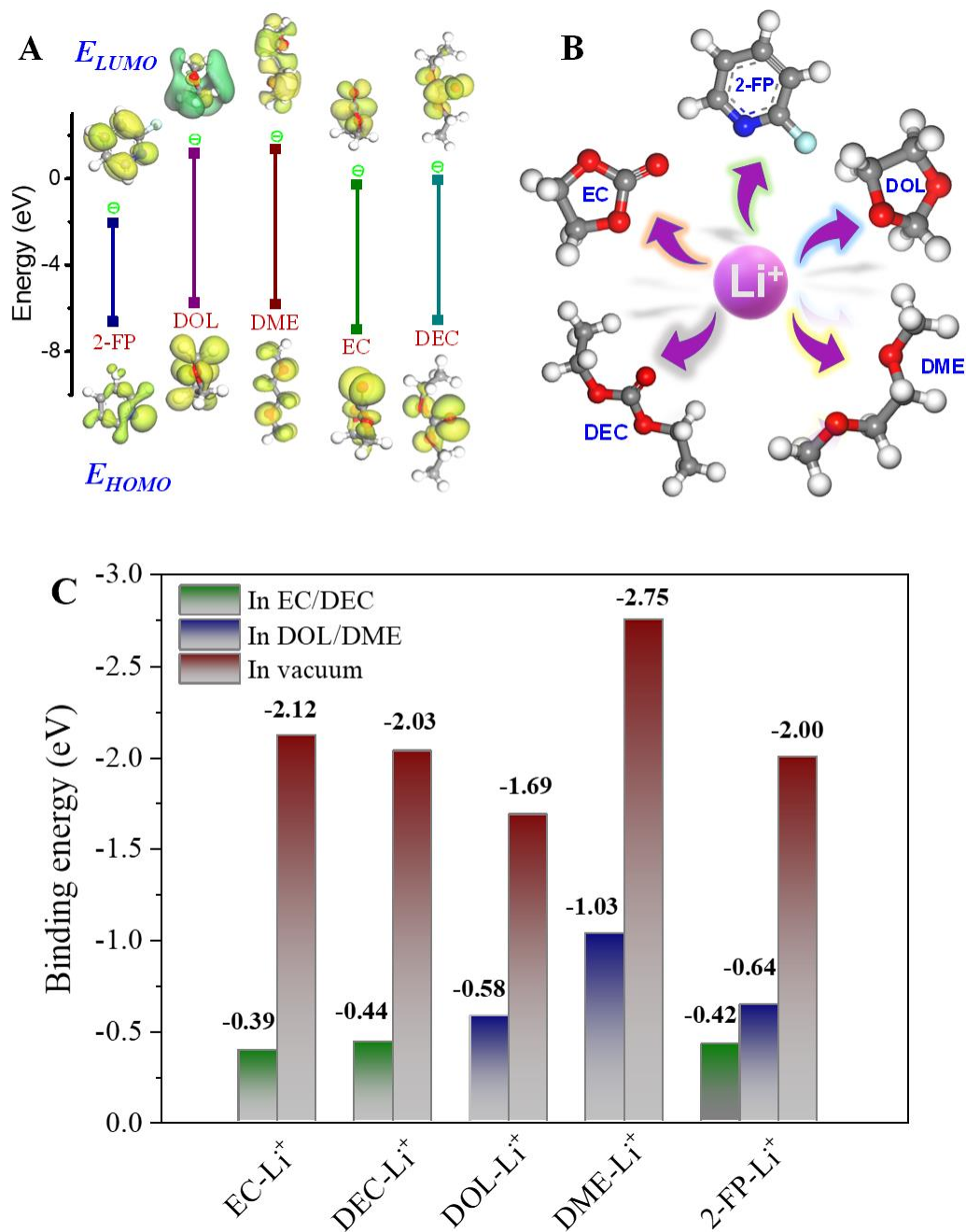


Fig. 5.1 (A) The molecular orbitals and energies for the HOMO and LUMO of the 2-FP and other solvents; (B) Schematic of solvation effect between Li^+ and solvents. The grey, white, red, blue, green, and purple spheres represent atoms of carbon, hydrogen, oxygen, nitrogen, fluorine, and lithium, respectively; (C) Summary of the binding energy between solvents and lithium ions in different electrolyte solutions and vacuum.

Fig. 5.1A shows the calculated molecular orbital energies with the HOMO and the LUMO energies of the 2-FP and the related ether- and carbonate-based electrolyte solvents of 1,3-dioxolane (DOL)/1,2-Dimethoxyethane (DME) and ethylene carbonate (EC)/diethyl carbonate (DEC). One can see that the LUMO energy of 2-FP (-2.0300 eV) is lower than those of solvent molecules, i.e., DOL (1.1756 eV), DME (1.3606 eV), EC (-0.2721 eV), and DEC (-0.0517 eV), indicating that 2-FP can be more easily reduced than all the solvent molecules to form the interface film [30]. Correspondingly, comparing with the HOMO energies of DOL (-5.7417 eV) and DME (-5.8057 eV) solvent molecules, the 2-FP has a relatively lower HOMO energy (-6.6125 eV), suggesting that these solvent molecules will be preferentially oxidized in the base LiTFSI in DOL: DME electrolyte. In the LiPF₆ in EC: DEC electrolyte system, although the HOMO energy of linear carbonate DEC (-6.5309 eV) is higher than that of cyclic carbonate EC (-6.9663 eV), the EC with stronger polarity is always more easily to be oxidized than DEC, forming a cathode electrolyte interface (CEI) layer on the electrode surface [31]. Hence, originating from the stronger polarity as well as the higher HOMO energy (-6.6125 eV versus EC), the pyridine ring-contained 2-FP molecule should be more easily oxidized on the electrodes to form the CEI layer in the EC: DEC electrolyte.

In nonaqueous electrolytes, the solvation structure of Li ions directly dictates the formation of SEI and CEI layers [32]. In this case, the interactions of Li ions and solvents molecules, as displayed in **Fig. 5.1B**, were deeply investigated through DFT calculations. The binding energies of different Li ions-solvent complexes are presented in **Fig. 5.1C**. Since the solvation effects are induced by dielectric constant of solvents, all the binding energies of complexes are greatly reduced in the actual electrolyte solvent in comparison with that in vacuum condition. As a result, the binding energies of Li⁺-EC, Li⁺-DEC, Li⁺-DOL, Li⁺-DME, Li⁺-2-FP (EC/DEC system) and Li⁺-2-FP (DOL/DME system) are reduced to -0.39, -0.44, -0.58, -1.03, -0.42 and -0.64 eV,

respectively. These results, coupling with the above molecular orbital energies, indicated that Li ions are also easily solvated by 2-FP to form the F-components contained solvation sheath, thus, rendering a LiF-rich and reliable electrode–electrolyte interfaces [33]. Moreover, it is worth noting that 2-FP has good compatibility with these four solvents. Thus, it can be served as an effective additive or a promising co-solvent in different electrolytes.

Besides, **Fig. 5.2** shows the structure changes of the 2-FP after the reduction by quantitative calculation. Herein, as the electrons are combined with the 2-FP molecule, the length of the C-F bond increases significantly. The length of C-F bond can be increased to 1.410 Å from the initial value of 1.358 Å (normally in a range of 1.35-1.36 Å) even with the introduction of one electron, however, other bonds can remain almost unchanged even under the introduction of three electrons [34]. These DFT calculations show that the reduction of the 2-FP is inclined to cleave the C–F bond so that the F atom is easily detached from the 2-FP molecule to form a stable SEI consisting of LiF during its preferential reduction process, which is also consistent with the previous reports [13, 24].

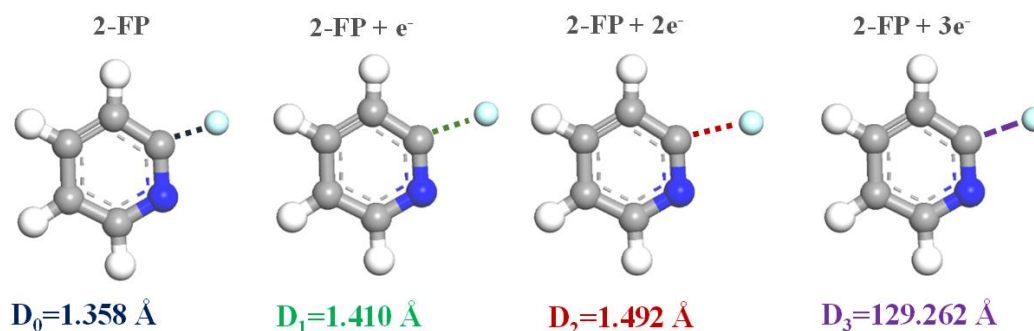


Fig. 5.2 The length changes of C-F bonds during the reduction of 2-FP molecule via the DFT theoretical calculations, where green and blue dots represent the locations of F and N atoms, respectively.

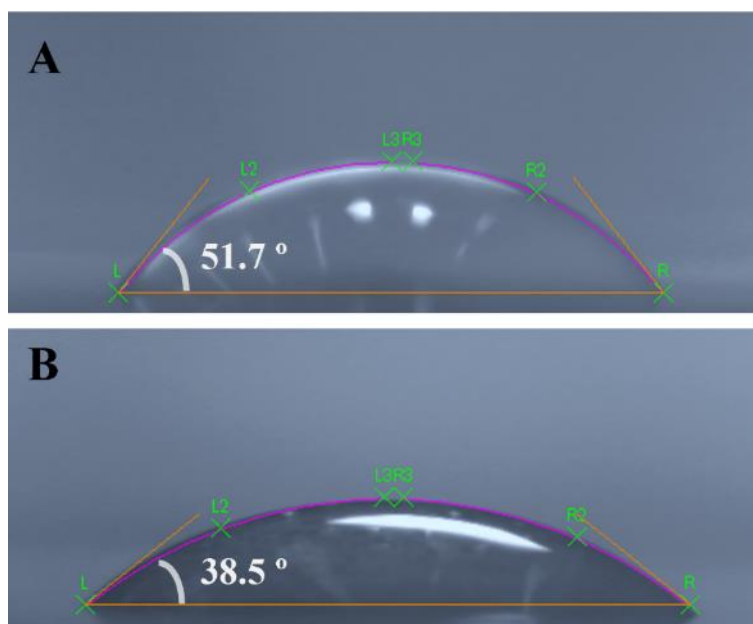


Fig. 5.3 Contact angles of the LiPF_6 electrolyte (A) and LiPF_6 with 2% of 2-FP electrolyte additive (B) drops on the Celgard 2400 PP separator.

The good wettability of electrolyte on the separator is conducive to decrease the contact resistance and facilitate the Li^+ ion transference, which could significantly affect the performance of lithium battery. **Fig. 5.3** shows the contact angles of the LiPF_6 electrolyte drops on the Celgard 2400 PP separator. One can see that the contact angle significantly decreased to 38.5° from 51.7° after the introduction of 2-FP electrolyte additive, indicating that the wettability of electrolyte on the surface of the PP separator is effectively improved due to the existence of the polar bond of the pyridine ring in the 2-FP molecule, which is expected to promote the electrochemical performance of the LMBs consequently [35]. Furthermore, comparing with the separator modified by inorganic nanoparticles or others, the addition of 2-FP electrolyte additive can obviously simplify the lyophilicity treatment process.

5.3.2 Electrochemical stability of the electrolyte

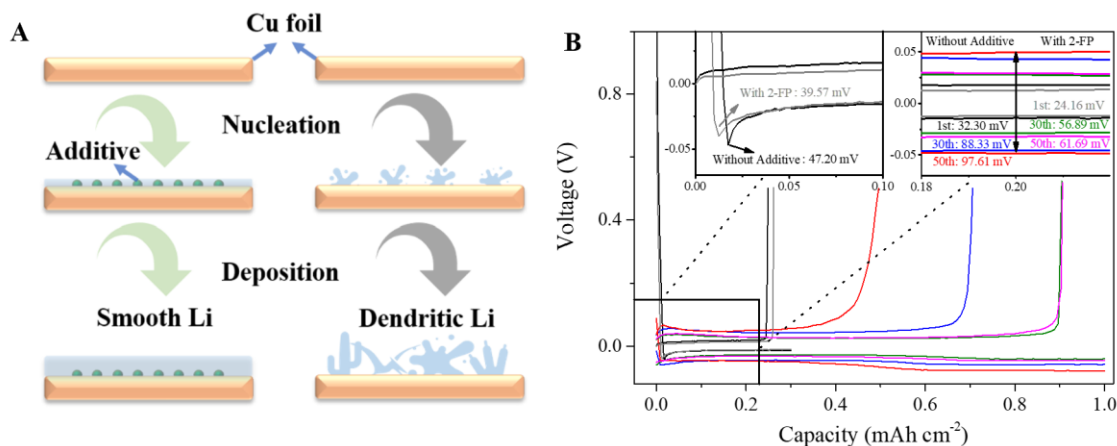


Fig. 5.4 (A) Illustration of Li nucleation and deposition on the Cu foil electrode with and without electrolyte additive; **(B)** Voltage profiles of Li|Cu cells with the LiPF₆ electrolytes in the absence and presence of 2% of 2-FP electrolyte additive. Insets show two enlarged views of voltage profiles.

The initial nucleating behavior generally decides the later Li dendrite formation in the LMBs. **Fig. 5.4A** illustrates the Li nucleation and deposition on the Cu foil electrode with and without electrolyte additive. Li⁺ ions reach the surface of Cu foil current collector under driving forces of the electrical field as well as the concentration gradient and start of nucleation after acquiring electrons [23]. Once the nuclei are formed on the Cu surface, since the overpotential for the metallic Li plating on the Li nuclei is much lower than that on the Cu surface [36], the Li⁺ ions are more likely to deposit on the existed Li nuclei continuously, resulting in the formation of Li dendrites, which will grow along the direction of separator with the assistance of electrical field, and eventually result in shorting [37]. In the presence of electrolyte additive, the 2-FP molecules will be evenly distributed on the surfaces of either Cu foil cathode or Li metal electrode. As such, since the Cu foil surface is decorated with the lithiophilic function groups of pyridine nitrogen [23], the lithium nucleation sites can be uniformly formed on the surface with much lower nucleation overpotential [36], which will make the metallic Li deposition uniformly and smoothly. The voltage profiles of Li|Cu cells with and without 2-FP electrolyte additive are displayed in **Fig.**

5.4B, in which the magnitude of the voltage spike at the onset of Li deposition corresponds to the Li nucleation overpotential, and the following plateau overpotential presents the deposition stage with the continuous Li growth [38]. One can see that the nucleation and plateau overpotentials in the presence of 2-FP electrolyte additive were 39.57 and 11.51 mV, lower than those (47.20 and 14.26 mV) without 2-FP. Meanwhile, from the changes in the plateau overpotential of Li stripping/plating process during the cycling process, one can see that the plateau overpotential in the case without 2-FP increased from 88.33 mV at the 30th cycle to 97.61 mV at the 50th cycle, and in contrast, that in the case with 2-FP only increased to 61.69 mV from 56.89 mV at the same cycles, which indicated that the stable and uniform lithium deposition process was induced by the addition of 2-FP electrolyte additive.

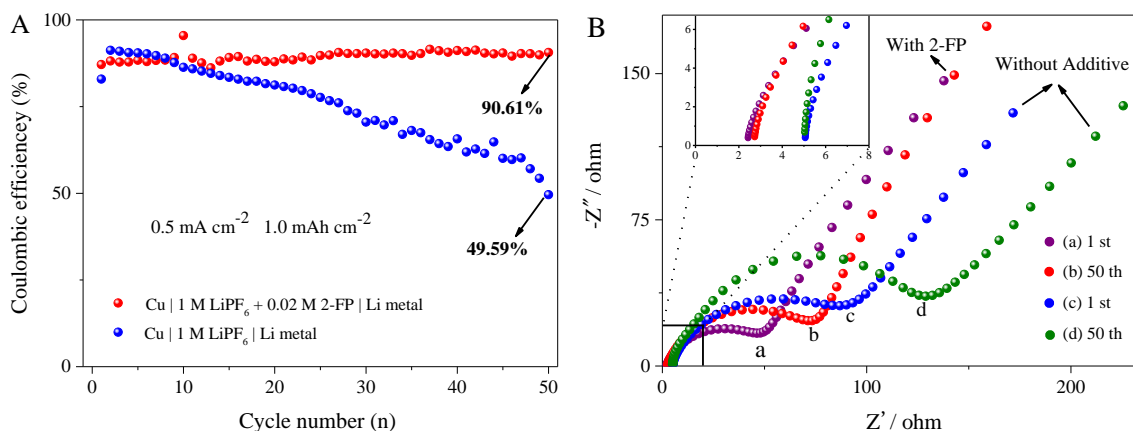


Fig. 5.5 (A) Coulombic efficiencies of Li|Cu cells with the LiPF₆ electrolytes in the absence and presence of 2% of 2-FP electrolyte additive at a current density of 0.5 mA cm⁻² and (B) EIS of Li|Cu cells after two different cycles. Inset shows the enlarged view of EIS spectra.

The coulombic efficiency (CE) is generally defined as the stripping/charging capacity over plating/discharging capacity, which can directly reflect the degree of parasitic side reactions related to the electrolyte. Herein, it can be applied to assess the reversibility and cyclability of electrochemical Li deposition and ionization on the Cu current collector. As can be seen in **Fig.**

5.5A, under the condition of 0.5 mA cm^{-2} and 1.0 mAh cm^{-2} , the CE of the cell without the 2-FP electrolyte additive after 50-cycle test decreased to 49.59%, which should be resulted from the increase of SEI resistance due to the growth of Li dendrites as those reported in the previous studies [13, 18]. In contrast, with the addition of 2-FP in the electrolyte, the CE maintained almost unchanged after the same 50-cycle test with a value of 90.61%, indicating that the 2-FP electrolyte additive stabilized the SEI layer, inhibiting the decomposition of electrolyte and the growth of Li dendrites. Moreover, to achieve high-energy density LMBs, it is generally necessary to adopt a limited amounts of Li metal or even Li metal-free (only current collector) anode [3, 39], thus, the high CE of Li|Cu cell with the 2-FP electrolyte additive is very important for the fabrication of the high-energy density LMBs.

Fig. 5.5B shows electrochemical impedance spectroscopy (EIS) changes of the Li|Cu cell with and without the 2-FP electrolyte additive after the 50-cycle test. Herein, the equivalent circuit for simulations is consistent with previous reports, and the simulated impedance responses were calculated directly using the ZView software [40]. Firstly, the electrolyte resistance values of LiPF_6 electrolytes with and without 2% of 2-FP electrolyte additive were 2.73 and 5.05 Ω , respectively, indicating that the addition of 2-FP can decrease the electrolyte resistance, which is benefit for the Li^+ ion transfer. As indicated above, this decrease should be attributed to the improved wettability of the electrolyte on the separator in the presence of 2-FP. Moreover, the Li|Cu cell with the 2-FP-containing electrolyte had a smaller SEI resistance of about 42.1 Ω than that without 2-FP (83.7 Ω) after the first cycle, suggesting a more uniform lithium nucleation site distribution with a smooth deposition layer in the presence of 2-FP. After 50-cycle test, the cell without the 2-FP electrolyte additive obviously exhibited an increased SEI resistance of 125.9 Ω whereas that with the 2-FP maintained a more stable SEI resistance of 75.8 Ω . It is well known that the base LiPF_6 electrolyte neither prevent the reaction with lithium metal, nor does it inhibit the growth of lithium

dendrites. Thus, in the absence of 2-FP electrolyte additive, the inevitable growth of the Li dendrites should be the main reason for the continuous increasing of the plateau overpotential as well as the SEI resistance. In contrast, by the addition of 2-FP electrolyte additive, a unique SEI layer should be more easily formed between the electrolyte and the electrode, which had the lower resistance for the Li ion migration due to the excellent interfacial compatibility of the SEI layer with the electrode during the cycling process. These EIS results are also consistent well with the voltage profiles, further confirming the effectiveness of 2-FP electrolyte additive to stabilize the Li metal anode and result in the uniform and dendrite-free Li deposition.

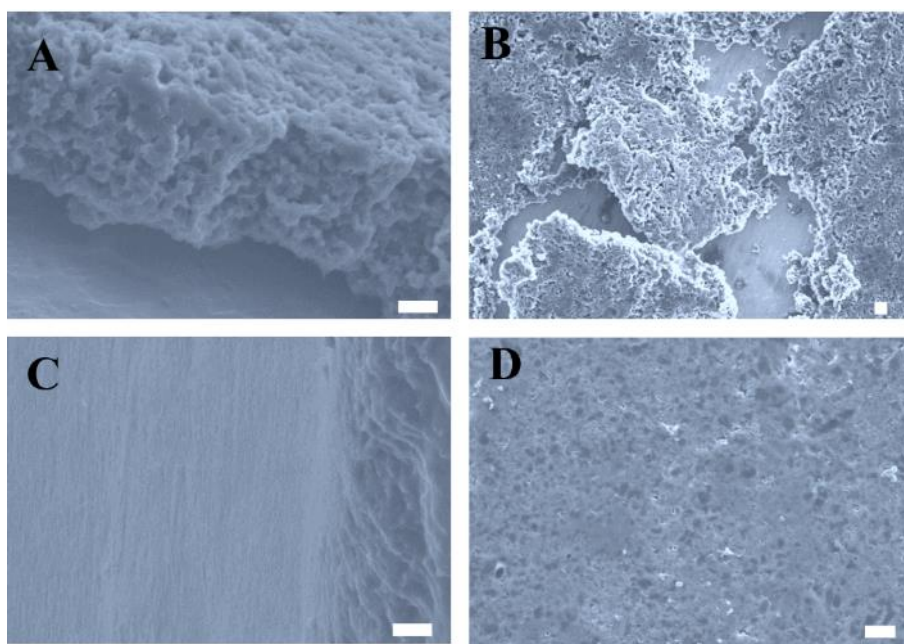


Fig. 5.6 SEM images of the deposited Li on the Cu substrate in Li|Cu cells: cross-section views and top views using LiPF_6 electrolyte without (**A**, **B**) and with (**C**, **D**) 2% of 2-FP electrolyte additive after the 50-cycle test. Scale bar: 10 μm .

Fig. 5.6 shows the morphologies of the deposited Li on the Cu foil surface after the 50-cycle test. In the absence of 2-FP, as can be seen from **Fig. 5.6A**, a loose Li deposition layer with a microporous structure and an uneven surface was obtained, which could not prevent the further

reaction between the electrolyte and the lithium metal, thereby enabling the electrolyte depleted in early stage, which could affect the Li ion transportation and finally terminate the normal operation of cell. This phenomenon was also observed in the previous study [3], and agreement with the CE and EIS test results (**Fig. 5.4**). Moreover, as indicated in **Fig. 5.6B**, it is obvious that the SEI layer was broken and the loose Li dendrites with sharp edges appeared on the electrode after the cycle test, which could penetrate the polymer separator and result in short-circuit. In comparison, as shown in **Figs. 5.6C and 5.6D**, in the presence of 2-FP electrolyte additive, significantly different morphologies in either cross-section or top views were observed. The plated Li metal layer was dense with a smooth structure. The surface images clearly exhibited that the Li dendrites were suppressed well. Especially, the induced Li deposition with rounded edges could decrease the possibility of puncturing the separator and the risk of short-circuit, thus enhancing the lifespan of LMBs [18].

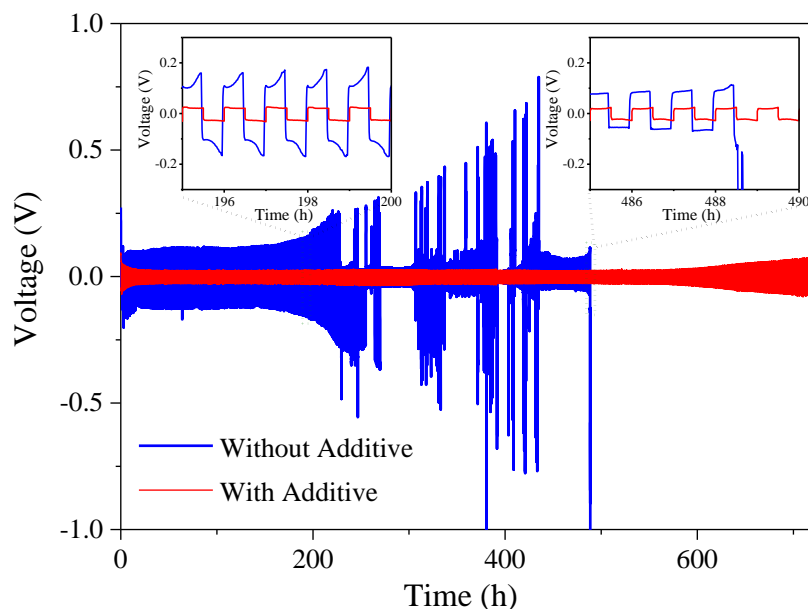


Fig. 5.7 Cycling performances of the Li|Li symmetrical cells with LiPF₆ electrolyte in the absence and presence of 2% of 2-FP electrolyte additive at a current density of 1 mA cm⁻².

The effect of the 2-FP electrolyte additive was also evaluated in a polarization test with a Li|Li

symmetrical cell, in which Li metal was plated and stripped time after time to mimic a practical cycling process. **Fig. 5.7** displays the voltage profiles as a function of time for the cells with and without 2-FP at a current density of 1 mA cm^{-2} . Generally, at the initial nucleation, a structural reorganization of the electrolyte/electrode could lead to the formation of a SEI layer, and thereafter, the polarization during Li plating and stripping process was greatly suppressed, which indicates a typical Li deposition behavior in the presence of Li metal electrode [14]. Herein, with the limited amount of electrolyte (30 μL), the Li|Li cell with the base LiPF_6 electrolyte displayed a relatively higher overpotential of 119.7 mV and short-circuiting occurred after about 230 h test, implying that this electrolyte cannot suppress the lithium dendrites effectively, in contrast, the cell with the 2-FP-containing electrolyte displayed a faint polarization overpotential of 26.4 mV, and excellent stability over 700 h testing without short-circuit. Moreover, the voltage shape and polarization overpotential displayed a significant difference from the case using the electrolyte without 2-FP, which indicated the stability of SEI layer. In addition, owing to the formation of SEI on the fresh Li deposition layer, the nucleation and growth polarization potentials were slowly increasing after the 600 h testing in the Li|Li cell with the 2-FP electrolyte additive [41]. The significantly enhanced Li metal stability after the addition of 2-FP should be resulted from not only the enhanced SEI layer and suppressed Li dendrites growth but also the improved interfacial compatibility. As a result, the symmetric Li|Li cell with the 2-FP electrolyte additive exhibited longer lifetime with safety even when the reduced amount of electrolyte (30 μL) was used.

5.3.3 Performance of LMBs

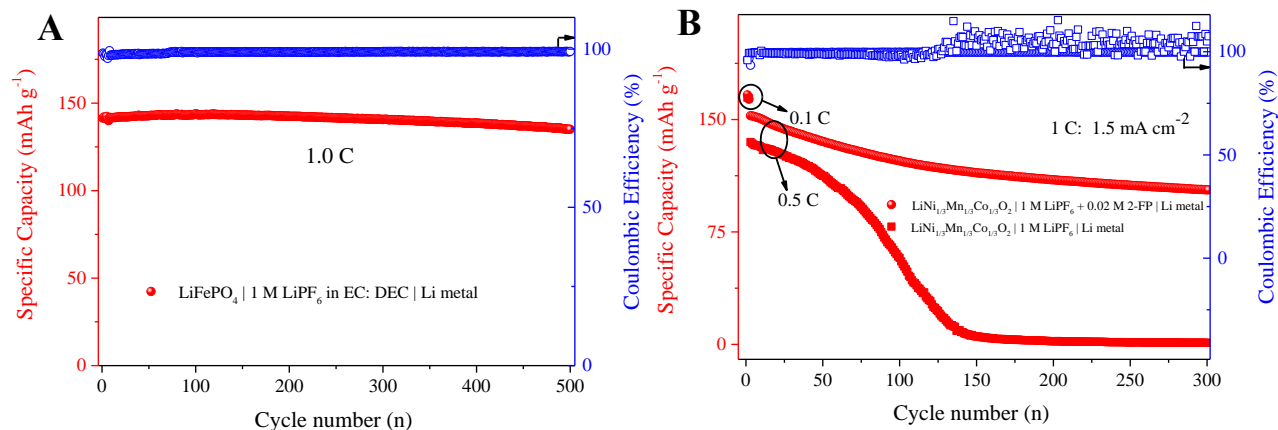


Fig. 5.8 (A) Cycling performance of LiFePO₄|Li metal batteries using the carbonate-based LiPF₆ electrolyte (60 μ L) at 1 C and 30 $^{\circ}$ C; **(B)** Cycling performances of NMC111|Li metal batteries using the LiPF₆ electrolytes without and with 2% of 2-FP electrolyte additive under 30 $^{\circ}$ C.

The effect and applicability of 2-FP electrolyte additive in the LMB cells were further evaluated. Herein, two full cells were constructed using the conventional carbonate-based and ether-based electrolytes as well as the commercial LiNi_{1/3}Mn_{1/3}Co_{1/3}O₂ (NMC111) and LiFePO₄ cathodes with a relatively high cathode areal capacity of 1.5 mAh cm⁻², respectively. In general, the two key parameters, i.e., cathode surface loading mass and charging current density, could affect the capacity fading of LMBs. That is, a higher cathode areal capacity always needs more utilization of Li in each deposition/stripping process, it will result in deeper parasitic side reactions and faster capacity fading, thus it requires more rigorous electrolyte stability. Meanwhile, a higher charge current density could lead to a quicker corrosion of Li metal, and therefore resulting in faster capacity fading of LMBs. In addition, a higher voltage cathode also requires a higher anodic stability of electrolyte [25]. As such, a low content of active materials and small charging current density are always used in order to lead to a very slight Li stripping/plating in the cell and finally extend the cycle life of LMBs. As such, **Fig. 5.8A** shows the excellent cycle stability of the

LiFePO₄|Li metal cell with areal capacity of about 0.3 mAh cm⁻², and the cell exhibited a high discharge capacity of 135.2 mAh g⁻¹ and coulombic efficiency of 99.25% even after 500 cycles. Although the cell rendered a capacity retention of 95.54% within the 500 cycles, such a low content of active material in the cathode will be not suitable for a practical high energy density LMB designs. In this study, to evaluate the electrolyte impact on the charging capability of LMBs reliably, a large amount of Li (equal to 1.5 mAh cm⁻², based on the cathode areal capacity) was considered to deposit and strip in each cycle. **Fig. 5.8B** shows the electrochemical properties of high-voltage NMC111|Li metal cells with LiPF₆ electrolyte in the presence and absence of 2-FP electrolyte additive.

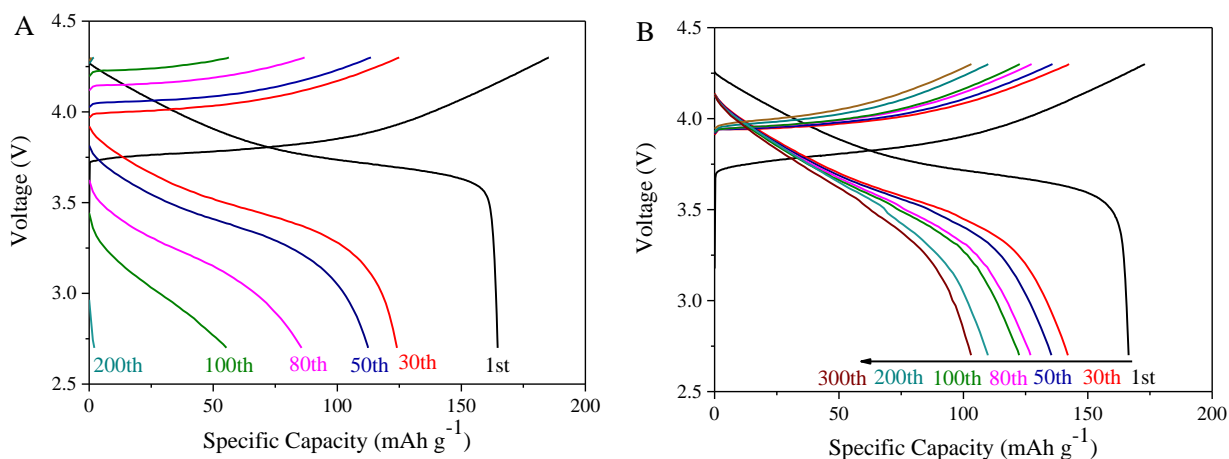


Fig. 5.9 Voltage curves as a function of cycle number of NMC111|Li batteries using (A) LiPF₆ electrolyte, (B) LiPF₆ with 2% of 2-FP electrolyte additive at 0.5 C and 30 °C.

As shown in **Fig. 5.9**, all the NMC111|Li metal cells exhibited almost the same lithiation/delithiation profiles and delivered the similar specific capacity of about 165 mAh g⁻¹ during the formation cycles at the low current density of 0.15 mA cm⁻². Nevertheless, in the subsequent cycles with a higher current density of 0.75 mA cm⁻², the cell without the 2-FP exhibited messy CEs with only a capacity retention of 15.5% at the 200th cycle and a rapid capacity decay from 135.1 to 28.9 mAh g⁻¹ within 120 cycles due to the easy Li dendrites growth and the

electrolyte depletion. Correspondingly, as shown in **Fig. 5.9A**, the continuous consumption of electrolyte caused a dramatic increase of electrode overpotential and a rapid cell impedance, leading to the battery failure at an early stage. In contrast, the NMC111|Li metal cells using the LiPF₆ electrolyte with 2% of 2-FP electrolyte additive possessed a much more stable capacity retention of 67.6% even after 300 cycles with a capacity of 103.1 mAh g⁻¹ and a CE of 99.89 %. Especially, the high CE indicated much lower consumptions of active Li as well as electrolyte. In addition, as shown in **Fig. 5.9B**, the presence of 2-FP also stabilized the cell overpotential during the cycling.

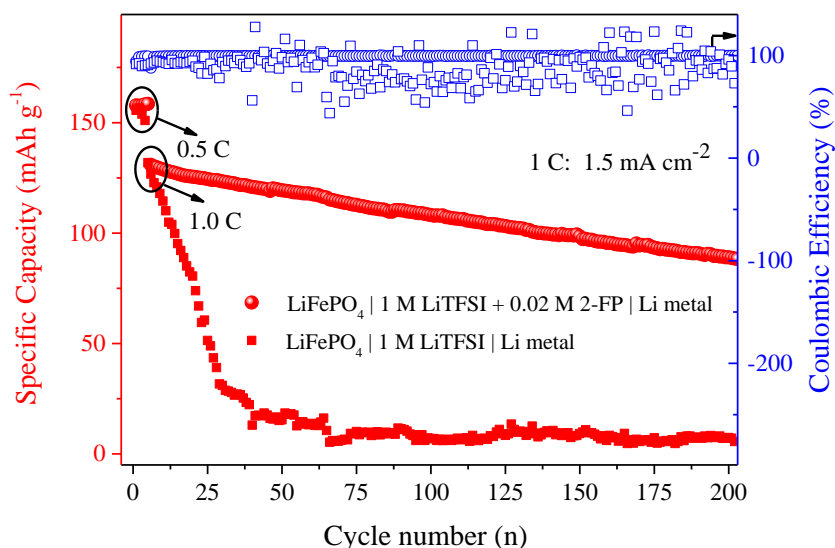


Fig. 5.10 Cycling performance of LiFePO₄|Li metal batteries using the LiTFSI electrolytes without and with 2% of 2-FP electrolyte additive at 1.5 mA cm⁻² and 30 °C.

Cycling stability of the LiFePO₄|Li metal cells with the ether-based LiTFSI electrolyte in the presence of 2-FP electrolyte additive was also evaluated using a higher current density of 1.5 mA cm⁻² at 30 °C. Herein, the reason why the LiFePO₄ cathode rather than the sulfur based cathode was chosen is its excellent cycle stability. Similarly, as shown in **Fig. 5.10**, the LiFePO₄|Li metal cell with the pure ether-based LiTFSI electrolyte exhibited a sharp capacity fading at around the

25th cycle, and a low CE of 88.47% as well as a low capacity retention of 5.78% within 200 cycles whereas the cell with the 2-FP electrolyte additive retained a capacity of 89 mAh g⁻¹ with a CE of 99.76 % after 200 cycles and a capacity retention of 68.04%, which was about 12 times higher than that of the cells without 2-FP electrolyte additive. In addition to the cycling stability, the LiFePO₄|Li metal cell with the ether-based LiTFSI electrolyte containing the 2-FP electrolyte additive also exhibited a promising rate capability at a 0.5 C rate, and delivered a reversible capacity of 158.5 mAh g⁻¹, which was still higher than that without 2-FP with a value of 151.0 mAh g⁻¹. These results from the full batteries reconfirmed the effectiveness of 2-FP in the formation of the robust SEI layers in the cell, which effectively protected the Li metal against the electrolyte attack, suppressing the Li dendrite growth. In contrast, taking the above observations into account, the rapid degradation of LMBs in the early stage was observed even with LiNO₃ containing routine electrolyte. It should be resulted not only from Li dendrite formation but also from the near complete consumption of lean electrolyte as well as rapid increase in internal resistance of cell since a poor-quality of SEI layer was generated in the initial formation cycles at 0.75 mA cm⁻² [3]. Besides, it is expected that the addition of 2-FP electrolyte additive is also benefit for the fast charging of LMBs since at least a current density of 0.7 mA cm⁻² was required for the fast charging[14].

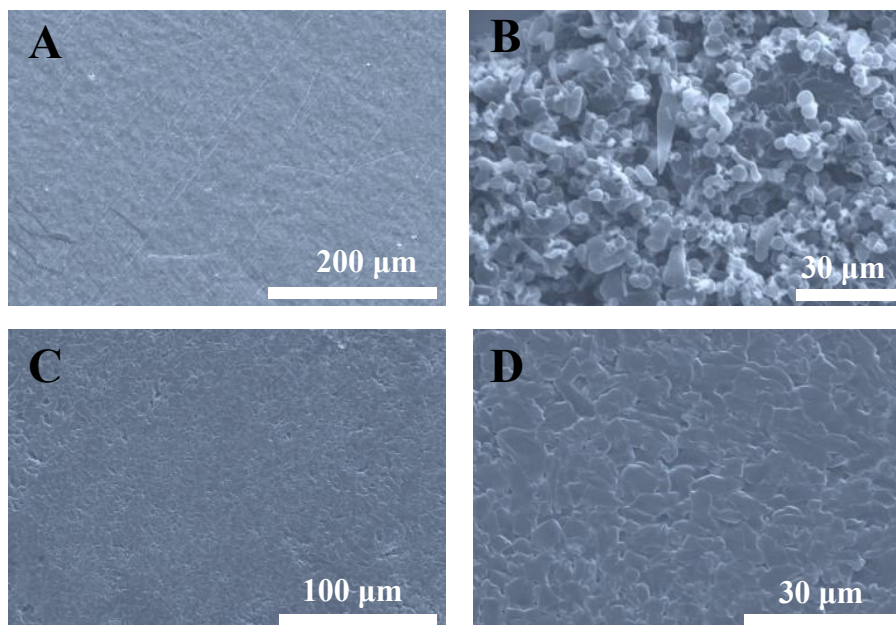


Fig. 5. 11 SEM images of the Li anode surfaces before (A) and after cycling test of LiFePO₄|Li metal batteries with LiTFSI electrolyte in the absence (B) and presence (C, D) of 2% of 2-FP electrolyte additive.

Fig. 5.11 shows the SEM images of the Li anode surfaces before (**Fig. 5.11A**) and after cycling test of LiFePO₄|Li metal batteries with LiTFSI electrolyte in the absence (**Fig. 5.11B**) and presence (**Fig. 5.11C and 11D**) of 2% of 2-FP electrolyte additive. Comparing to the pristine Li metal anode with a flat surface (**Fig. 5.11A**), it is obvious that short needle-like Li dendrites were formed on the whole Li anode surface with a very disarrayed and porous structure (**Fig. 5.11B**) when the base LiTFSI electrolyte was used. Such a Li metal anode structure indicated that the electrolyte and Li metal could be depleted during the charging/discharging processes, leading to the pulverization of Li, formation of dead li, and even cell swelling, and finally resulting in the fast failure of the cells and safety problem, as evidenced by the low CE and poor cycling lifetime. In contrast, as the 2-FP was added in LiTFSI electrolyte, a significantly uniform and robust surface was obtained (**Figs. 5.11C and 11D**), where the deposited Li had a dense shield-like structure, which could

effectively suppress Li dendrites growth. It should be derived from the possible formed LiF-rich protective SEI layer with the assistance of 2-FP electrolyte additive. Especially, the negative charges on the surface from the nitride ions of 2-FP electrolyte additive could enhance the surface Li^+ diffusion, resulting in a smooth lithium deposit. Such a dense Li deposition is benefit to improve the battery safety since the shield-like Li structure has excellent compatibility with the polymer separator and low ability to pierce the separator [18]. Besides, it should be noted that the change of surface morphology in the case using the LiTFSI electrolyte was apparently different from that using the LiPF_6 electrolyte due to the different operation current densities and operation voltage ranges although both LiPF_6 and LiTFSI electrolytes mainly led to the deposition of short needle-like Li in the absence of 2-FP electrolyte additive.

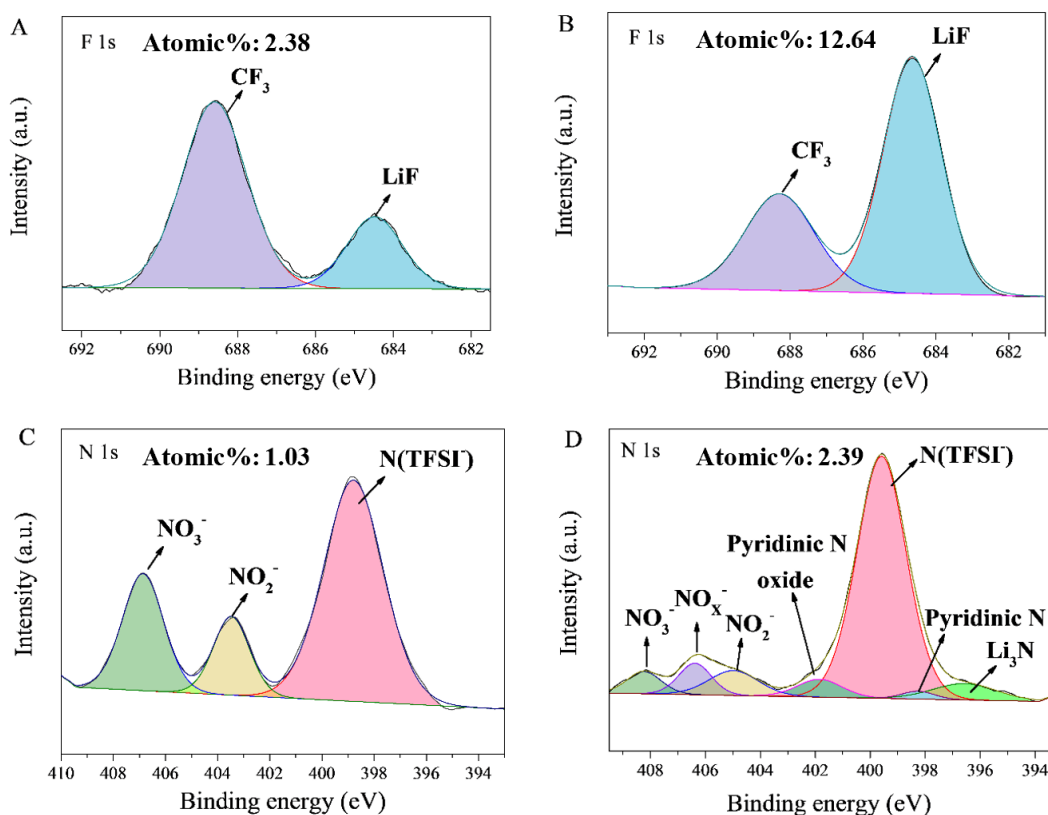


Fig. 5.12 XPS spectra of F 1s and N 1s for Li metal retrieved from $\text{LiFePO}_4|\text{Li}$ metal batteries with the LiTFSI electrolyte in the absence (A, C) and presence (B, D) of 2% of 2-FP electrolyte additive.

X-ray photoelectron spectroscopy (XPS) was further employed to investigate the components of SEI layer generated on the Li metal after the cycling test. **Fig. 5.12** compares the F 1s and N 1s spectra of SEI layer forming on the anode of the LiFePO₄|Li metal cell without and with 2-FP electrolyte additive. As displayed in **Figs. 5.12A** and **12B**, the peaks at about 684.5 and 688.6 eV are ascribed to Li-F and CF₃ bonds, originating from the decomposition of TFSI⁻ group [42]. It was found that the significantly higher F content in the SEI layer in the presence of the 2-FP electrolyte additive, that is, the F atomic ration was increased to 12.64% with 2-FP from 2.38% in the case without 2-FP, indicating that the addition of 2-FP effectively helped the formation of LiF species. This result is consistent with the above DFT calculation results. Here, it is reported that the LiF in the SEI layer generally has a strong electronic insulation effect to prevent electrons from crossing the SEI layer during the Li plating process. Moreover, a conformal and dense SEI layer enriched with LiF on the Li anode surface could not only effectively suppress the parasitic reactions between Li metal and electrolyte, protecting the Li metal against the electrolyte attack, but also prompt the transport of Li⁺ ions and afford sustainable use of LMBs [13-14]. By contrast, the N 1s spectra displayed more conspicuous difference in two cases. In **Figs. 5.12C** and **12D**, for the SEI film formed in the case without 2-FP electrolyte additive, three peaks at about 398.5, 403.4, and 407.2 eV, corresponding to the characteristic peaks of TFSI⁻, LiNO₂, and LiNO₃ [43], respectively, should be resulted from the decomposition of the 1% LiNO₃-containing electrolyte. For comparison, in the case with the 2-FP, four extra peaks at 406.5, 401.8, 398.4, and 396.6 eV, corresponding to NO_x⁻, pyridinic N and its derivatives, and Li₃N (the binding energies of N 1s in metallic nitrides are located in the range between 396 and 397 eV) [18, 44-45], respectively, were observed, and the N element concentration in the SEI layer reached to 2.39%, affirming that the 2-FP electrolyte additive involved in the formation of SEI layer on the surface of Li metal anode. In particular, it has been widely reported that Li₃N played a crucially important role in the property

of the robust and stable SEI layer and Li dendrite growth [41, 43], and meanwhile, the existence of Li_3N and pyridinic N could enhance the ionic conductivity and improve the formation of the uniform lithium nucleation sites for the uniform and rapid deposition of Li. As such, the LiF-rich SEI layer achieved by the assistance of 2-FP combined with the high Li ion diffusion property of the Li_3N -containing SEI layer should be beneficial for the enhancement of the stability SEI layer and the formation of the uniform dendrite-free Li deposition.

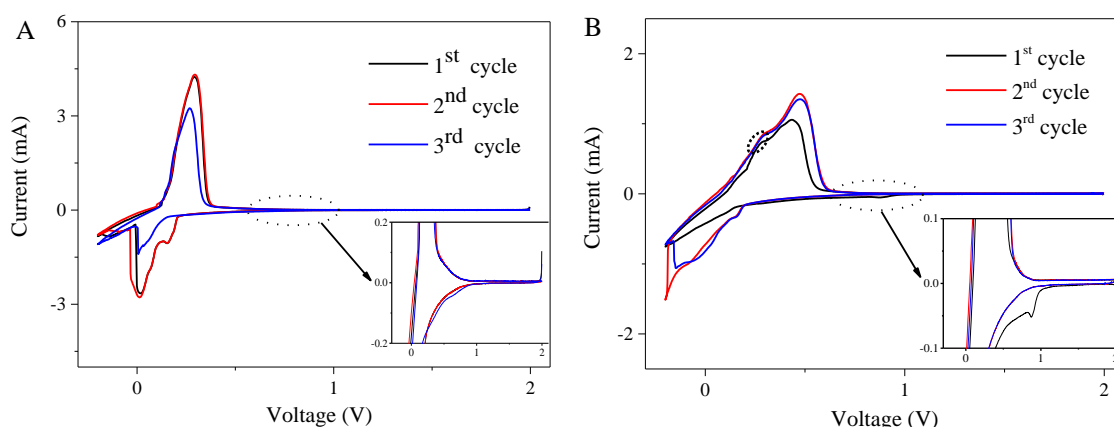


Fig. 5.13 Cyclic voltammogram curves of Li|Graphite cells in (A) LiPF_6 electrolyte, (B) LiPF_6 electrolyte with 2% of 2-FP electrolyte additive at a scan rate of 0.1 mV s^{-1} . Insets show the enlarge views of CV curves.

To verify the redox behaviour of 2-FP electrolyte additive on the electrode surface, as shown in **Fig. 5.13**, cyclic voltammograms were conducted using Li/graphite cells. Herein, the redox peaks below 0.3 V could be described to the lithiation/delithiation process of lithium ions on the graphite electrode [46], and the reduction peak at approximately 0.634 V signified the reductive decomposition of EC. Compared to the CV curve without the 2-FP, an obvious irreversible reduction peak occurring from about 0.875 V at the first cycle in the case with the 2-FP, which should be attributed to the preferential reduction of 2-FP to form the robust SEI layer. Similarly, the CV curve of the cell with the 2-FP electrolyte additive had a weak oxidation peak occurring

from approximately 0.27 V, which could be attributed to the preferential oxidation of 2-FP to form the pyridinic N oxides as well as the cathode electrolyte interface (CEI). These observations were consistent with the above DFT theoretical calculations and XPS analyses.

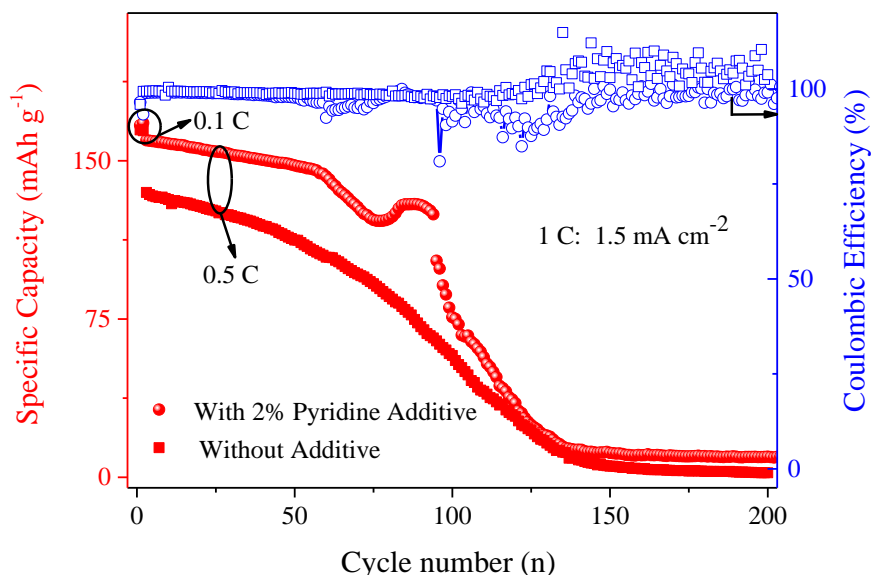


Fig. 5.14 Cycling performances of NMC111|Li metal batteries using the LiPF₆ electrolytes without and with 2% of Pyridine electrolyte additive under 30 °C.

In addition, due to the similar molecular structure and a high level of coordination ability to Li⁺ ions, the pyridine was selected as an electrolyte additive to further clarify the role of the 2-FP additive. DFT calculation results proved that the pyridine was preferentially reduced in the electrolyte since its LUMO energy of -2.8826 eV was significantly lower than that of 2-FP (-2.0300 eV). Subsequently, when the electrolyte additive was replaced with 2% pyridine, as shown in **Fig. 5.14**, the capacity retention of the NMC111|Li metal cell rivaling the 2-FP containing electrolyte was obtained in the first 50 cycles and then, a rapid loss of capacity with a low capacity of 35.15 mAh g⁻¹ after 120 cycles occurred, indicating that the lithiophilic sites and a small amount of metallic nitrides originated from the pyridine-N played a limited role in long-term stable cycling of LMBs when compared to the results by using 2-FP additive. Thus, the unique advantages of 2-

FP electrolyte additive on the formation of a low porosity, LiF and Li₃N rich robust SEI to facilitate uniform Li deposition over long cycling were further confirmed.

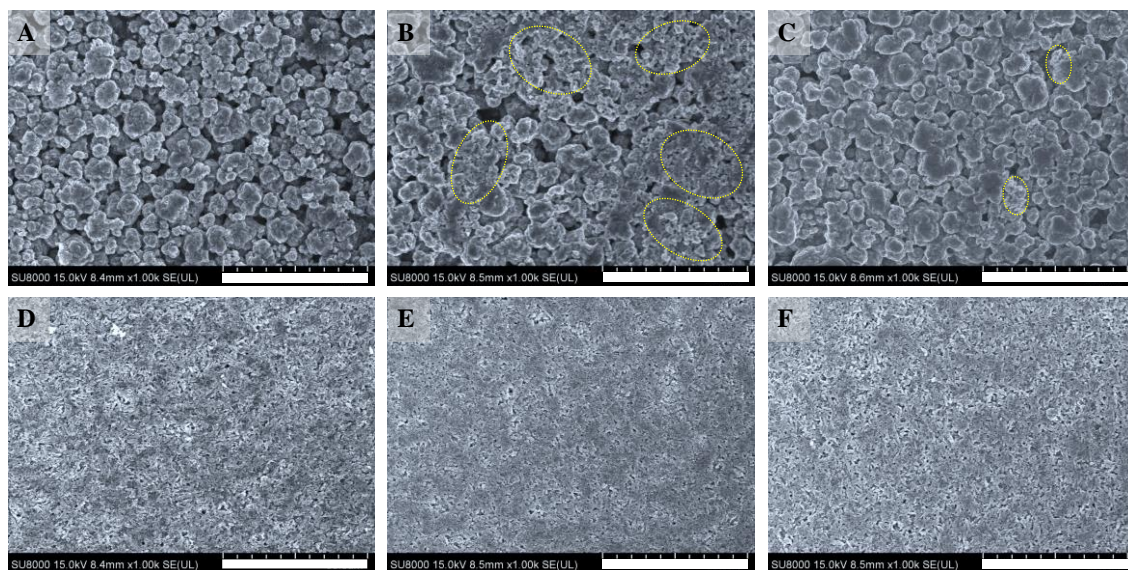


Fig. 5.15 SEM images of the NMC111(A-C) and LiFePO₄ (D-F) cathode surfaces before (A, D) and after cycling tests in the absence (B, E) and presence (C, F) of 2% 2-FP electrolyte additive. Scale bar: 50 μ m.

Fig. 5.15 shows the surface morphologies of the pristine and cycled cathodes in the absence and presence of 2-FP electrolyte additive. Compared to the uniform particle distribution morphology in the pristine NMC111 electrode (**Fig. 5.15A**), most of the NMC111 particles were cracked and pulverized into smaller particles after cycling with a routine LiPF₆ electrolyte (**Fig. 5.15B**), indicating the starting of chemical corrosion and exfoliation in the cathode during cycling [47]. In contrast, as displayed in **Fig. 5.15C**, the particles on the cycled NMC111 electrode were well maintained with a relatively uniform and compact surface in the presence of 2-FP electrolyte additive, which is in accordance with the superior capacity retention of LMBs with 2-FP additive. Interestingly, as shown in **Figs. 5.15D, 15E, and 15F**, it can be observed that the LiFePO₄ cathodes had almost the same surface morphology after cycling in different electrolytes. In this case, the

cathode morphology of LiFePO_4 should not be used as the main indicator of LMBs performance due to the highly stable nature of Ni-free LiFePO_4 cathode. Moreover, this phenomenon was consistent with the above conclusion that good electrolyte retentivity along with high-quality passivation SEI layer played a decisive role in prolonging the cycle life of LMBs using LiFePO_4 as the cathode. As such, drawing from the superior structural integrity of cathode with 2-FP additive compared to the base electrolyte, it is more likely that 2-FP contributed to the interfacial stabilization by robust CEI formation through preferential oxidation as well as LiF diffusion from the Li metal anode to the cathode surface [48]. Similarly, a desirable CEI layer could not only effectively suppress the side reactions between high-voltage cathode and electrolyte, but also prevent lattice oxygen exposure in cathode materials and enhance the safety of LMBs.

Based on the above study, the interface engineering strategy for fabrication of safe and reliable LMBs with such an effective electrolyte additive of 2-FP is illustrated in **Fig. 5.16**. In the absence of 2-FP, short needle-like Li dendrites with a disarrayed porous structure over the whole surface of Li anode surface are easily formed during the cycling process, and the continuous consumption of electrolyte always cause the failure operation of LMBs at an early stage. To solve this problem, the electrolyte additives such as 2-FP could be added in the electrolyte to improve the electrolyte wettability, lower the nucleation and deposition overpotential, and form the stable and robust SEI layer with the uniform dendrite-free Li deposition. As such, a safe and stable LMB with Li metal anode can be obtained.

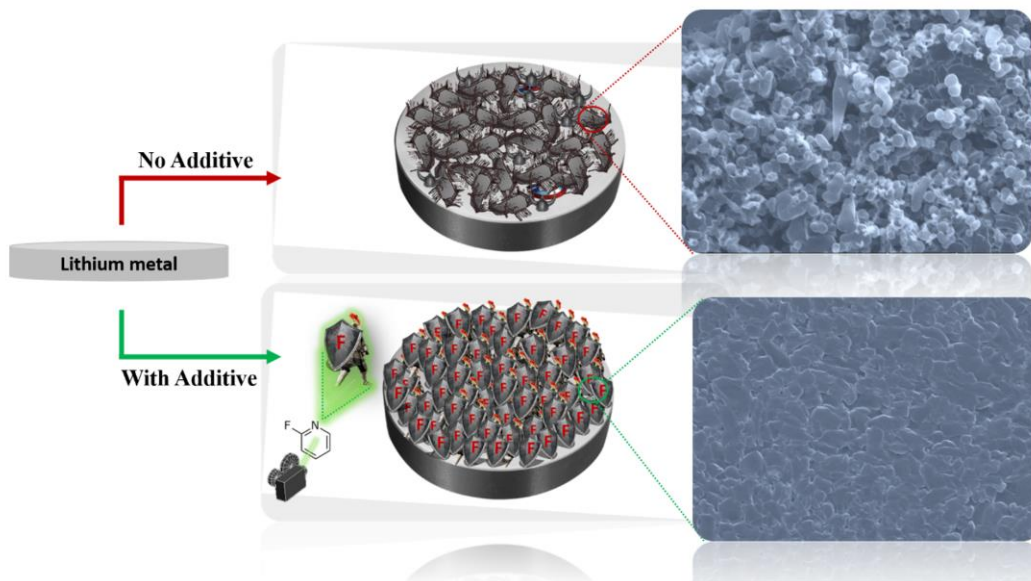


Fig. 5.16 A proposed evolution of SEI layer compositions with the electrolytes in the absence and presence of the 2-FP electrolyte additive.

Consequently, in comparison to the reported LMBs with different areal capacities in the presences of other kinds of electrolyte additives, as shown in **Table 5.1**, the 2-FP should be an effective electrolyte additive to enhance the discharge capacity as well as the cycling stability of LMBs. In addition, compared to the current commercial electrolyte additive FEC, the 2-FP had lower cost ($2.19\$ \text{ g}^{-1}$ versus $22.0\$ \text{ g}^{-1}$ of FEC, from www.sigmaaldrich.com/) as well as lower dosage demand, and better performance in spite of a similar working mechanism. Thus, it should become a commercial additive in near future.

Table 5.1 Comparison of various electrolyte additives for LMBs with different areal capacities.

Electrolyte and Amount	Electrolyte Additive	Areal Capacity (mAh cm ⁻²)	Capacity Retention (%)	Current density (mA cm ⁻²)	Cycles (n)	Ref
1 M LiTFSI _{0.6} -LiTFPFB _{0.4} in PC: EC: EMC, NG ^a	0.05 M LiPO ₂ F ₂	1.5	67.24%	0.75	100	[49]
1.2 M LiFSI in EC: EMC: BTFE, 75 μL ^b	0.15 M LiDFOB ^c	3.8	84%	1.0	100	[17]
1 M LiTFSI _{0.6} -LiBOB _{0.4} in EC: EMC, 100 μL ^d	0.05 M LiPF ₆	1.75	97.1%	1.75	500	[14]
1 M LiTFSI in DOL: DME + IL Pyr1(12) FSI, 50 μL ^e	IL/Solvent: 1:12 (v/v)	1.7	74.6%	0.8	500	[18]
1 M LiTFSI in DOL: DME, 110 μL	5 wt% TMS-FNFSI ^f	0.68	92%	0.136	100	[50]
1 M LiPF ₆ in EC: DMC, NG ^g	0.02 M TTFEB ^h	0.51	92%	0.51	500	[13]
1 M LiPF ₆ in EC: DEC;	0.02 M 2-FP	1.5	67.6%	0.75	300	This
1 M LiTFSI in DOL/DME +1% LiNO ₃ ;30 μL			68.04%	1.5	200	work

^a: lithium trifluoro(perfluoro-*tert*-butoxy) borate (LiTFPFB), propylene carbonate (PC), ethylene carbonate (EC)/ethyl methyl carbonate (EMC); ^b: bis(2,2,2-trifluoroethyl) ether (BTFE); ^c: lithium difluoro(oxalate)borate (LiDFOB); ^d: lithium bis(oxalato)borate (LiBOB); ^e: 1-dodecyl-1-methylpyrrolidinium bis(fluorosulfonyl)imide (Pyr1(12)FSI); ^f: (CH₃)₃Si-N[(FSO₂)(n-C₄F₉SO₂), trimethylsilyl (fluorosulfonyl) (n-nonafluorobutanesulfonyl) imide (FNFSI); ^g: dimethyl carbonate (DMC), Not Given (NG); ^h: Tris (2, 2, 2-trifluoroethyl) borate (TTFEB).

5.4 Conclusions

In summary, a reliable and low cost electrolyte additive of 2-FP was discovered for the first time and successfully applied in the commercial carbonate-based as well as ether-based electrolytes for the LMBs. When using this 2-FP-containing electrolyte to assemble the LMBs with a high areal capacity (1.5 mAh cm⁻²) as well as a high-voltage cathode of LiNi_{1/3}Mn_{1/3}Co_{1/3}O₂, the obtained LMBs exhibited substantially enhanced high voltage cyclability and high energy

density. Meanwhile, the $\text{LiFePO}_4|\text{Li}$ metal cell with only a limited amount of 2-FP-containing electrolyte still exhibited a capacity retention of 68.04% even after 200-cycle test at a high current density of 1.5 mA cm^{-2} . Furthermore, combining with the DFT calculations, it is confirmed that the 2-FP electrolyte additive not only plays a critical role in decreasing the nucleation and deposition overpotentials, but more importantly also induces the generation of the robust and dense SEI layer enriched with LiF and Li_3N components that can effectively suppress the parasitic reactions between Li metal and electrolyte and permit the prompt transport of Li^+ ions. Furthermore, the quantum chemistry calculations also verified that the reduction of the 2-FP molecule is inclined to break of the C-F bond so that the F atom is easily detached from the 2-FP molecule to form a stable SEI consisting of LiF during its preferential reduction process. It is expected that such a 2-FP electrolyte additive could be added to commercial electrolytes with various voltage windows for the improvement of the performances of next-generation LMBs.

References

- [1] K. Xu, Electrolytes and Interphases in Li-Ion Batteries and Beyond, *Chem. Rev.* 114 (2014) 11503–11618.
- [2] P. Albertus, S. Babinec, S. Litzelman, A. Newman, Status and challenges in enabling the lithium metal electrode for high-energy and low-cost rechargeable batteries, *Nat. Energy* 3 (2018) 16–21.
- [3] J. Liu, Z. Bao, Y. Cui, E.J. Dufek, J.B. Goodenough, P. Khalifah, Q. Li, B.Y. Liaw, P. Liu, A. Manthiram, Y.S. Meng, V.R. Subramanian, M.F. Toney, V. V Viswanathan, M.S. Whittingham, J. Xiao, W. Xu, J. Yang, X. Q. Yang, J.G. Zhang, Pathways for practical high-energy long-cycling lithium metal batteries, *Nat. Energy* 4 (2019) 180–186..
- [4] Z. Wu, Z. Xie, A. Yoshida, Z. Wang, X. Hao, A. Abudula, G. Guan, Utmost limits of various solid electrolytes in all-solid-state lithium batteries: A critical review, *Renewable*

Sustainable Energy Rev. 109 (2019) 367–385.

- [5] Z. Wu, Z. Xie, A. Yoshida, J. Wang, T. Yu, Z. Wang, X. Hao, A. Abudula, G. Guan, Nickel phosphate nanorod-enhanced polyethylene oxide-based composite polymer electrolytes for solid-state lithium batteries, *J. Colloid. Interf. Sci.* 565 (2020) 110-118.
- [6] Z. Xie, Z. Wu, X. An, A. Yoshida, Z. Wang, X. Hao, A. Abudula, G. Guan, Bifunctional ionic liquid and conducting ceramic co-assisted solid polymer electrolyte membrane for quasi solid-state lithium metal batteries, *J. Membr. Sci.* 586 (2019) 122-129.
- [7] J. Qian, W.A. Henderson, W. Xu, P. Bhattacharya, M. Engelhard, O. Borodin, J.G. Zhang, High rate and stable cycling of lithium metal anode, *Nat. Commun.* 6 (2015) 6362.
- [8] A. Basile, A. I. Bhatt, A. P. O'Mullane, Stabilizing lithium metal using ionic liquids for long-lived batteries, *Nat. Commun.* 7 (2016) 11794.
- [9] H. Zhang, G. G. Eshetu, X. Judez, C. Li, L. M. R. Martínez, and M. Armand, Electrolyte additives for lithium metal anodes and rechargeable lithium metal batteries: progresses and perspectives, *Angew. Chem. Int. Ed.* 57 (2018) 15002-15027.
- [10] E. Kazyak, K. N. Wood, N. P. Dasgupta, Improved cycle life and stability of lithium metal anodes through ultrathin atomic layer deposition surface treatments, *Chem. Mater.* 27 (2015) 6457-6462.
- [11] Y. Chen, M. Yue, C. Liu, H. Zhang, Y. Yu, X. Li, H. Zhang, Long cycle life lithium metal batteries enabled with upright lithium anode, *Adv. Funct. Mater.* 29 (2019) 1806752.
- [12] L.J. Chen, H. Chen, Z. Wang, X.H. Gong, X.H. Chen, M.Y. Wang, S.Q. Jiao, Self-supporting lithiophilic N-doped carbon rod array for dendrite-free lithium metal anode, *Chem. Eng. J.* 363 (2019) 270–277.
- [13] Y. Ma, Z. Zhou, C. Li, L. Wang, Y. Wang, X. Cheng, P. Zuo, C. Du, H. Huo, Y. Gao, G. Yin, Enabling reliable lithium metal batteries by a bifunctional anionic electrolyte additive,

- Energy Storage Mater. 11 (2018) 197–204.
- [14] J. Zheng, M.H. Engelhard, D. Mei, S. Jiao, B.J. Polzin, J.G. Zhang, W. Xu, Electrolyte additive enabled fast charging and stable cycling lithium metal batteries, *Nat. Energy* 2 (2017) 17012.
- [15] X.Q. Zhang, X.B. Cheng, X. Chen, C. Yan, Q. Zhang, Fluoroethylene carbonate additives to render uniform Li deposits in lithium metal batteries, *Adv. Funct. Mater.* 27 (2017) 1605989.
- [16] H. Ota, K. Shima, M. Ue, J.i. Yamaki, Effect of vinylene carbonate as additive to electrolyte for lithium metal anode, *Electrochim. Acta* 49 (2004) 565–572.
- [17] L. Yu, S. Chen, H. Lee, L. Zhang, M. H. Engelhard, Q. Li, S. Jiao, J. Liu, W. Xu, J. G. Zhang, A localized high-concentration electrolyte with optimized solvents and lithium difluoro(oxalate)borate additive for stable lithium metal batteries, *ACS Energy Lett.* 3 (2018) 2059–2067.
- [18] D.J. Yoo, K.J. Kim, J.W. Choi, The synergistic effect of cation and anion of an ionic liquid additive for lithium metal anodes, *Adv. Energy Mater.* 8 (2018) 1702744.
- [19] S. Liu, G. Li, X. Gao, Lanthanum nitrate as electrolyte additive to stabilize the surface morphology of lithium anode for lithium–sulfur battery, *ACS Appl. Mater. Interfaces* 8 (2016) 7783–7789.
- [20] J. Qian, W. Xu, P. Bhattacharya, M. Engelhard, W.A. Henderson, Y. Zhang, J.G. Zhang, Dendrite-free Li deposition using trace-amounts of water as an electrolyte additive, *Nano Energy* 15 (2015) 135–144.
- [21] W. Li, H. Yao, K. Yan, G. Zheng, Z. Liang, Y.M. Chiang, Y. Cui, The synergetic effect of lithium polysulfide and lithium nitrate to prevent lithium dendrite growth, *Nat. Commun.* 6 (2015) 7436.

- [22] J. Pires, A. Castets, L. Timperman, J. Santos-Peña, E. Dumont, S. Levasseur, C. Tessier, R. Dedryvère, M. Anouti, Tris (2, 2, 2-trifluoroethyl) phosphite as an electrolyte additive for high-voltage lithium-ion batteries using lithium-rich layered oxide cathode, *J. Power Sources* 296 (2015) 413–425.
- [23] T. Z. Hou, X. Chen, H. J. Peng, J. Q. Huang, B. Q. Li, Q. Zhang, B. Li, Design principles for heteroatom-doped nanocarbon to achieve strong anchoring of polysulfides for lithium-sulfur batteries, *Small* 12 (2016) 3283–3291.
- [24] N. von Aspern, G.V. Röschenthaler, M. Winter, I. Cekic-Laskovic, Fluorine and lithium: ideal partners for high-performance rechargeable battery electrolytes, *Angew. Chem. Int. Ed.* 58 (2019) 15978-16000.
- [25] X. Fan, L. Chen, O. Borodin, X. Ji, J. Chen, S. Hou, T. Deng, J. Zheng, C. Yang, S.C. Liou, K. Amine, K. Xu, C.S. Wang, Non-flammable electrolyte enables Li-metal batteries with aggressive cathode chemistries, *Nat. Nanotechnol.* 13 (2018) 715.
- [26] R. Fang, S. Zhao, Z. Sun, D.W. Wang, H.M. Cheng, F. Li, More reliable lithium-sulfur batteries: status, solutions and prospects, *Adv. Mater.* 29 (2017) 1606823.
- [27] H. Li, Practical evaluation of Li-ion batteries, *Joule* 3 (2019) 908-919.
- [28] C. Lee, W. Yang, R. G. Parr, Development of the Colle-Salvetti Correlation-Energy Formula Into a Functional of the Electron Density, *Phy. Rev. B: Condens. Matter.* 37 (1988) 785-789.
- [29] T. Yang, W. Fan, C. Wang, Q. Lei, Z. Ma, L. Yu, X. Zuo, J. Nan, 2,3,4,5,6-Pentafluorophenyl methanesulfonate as a versatile electrolyte additive matches $\text{LiNi}_{0.5}\text{Co}_{0.2}\text{Mn}_{0.3}\text{O}_2$ /graphite batteries working in a wide-temperature range, *ACS Appl. Mater. Interfaces* 10 (2018) 31735–31744.
- [30] H. Ota, Y. Sakata, A. Inoue, S. Yamaguchi, Analysis of vinylene carbonate derived SEI

- layers on graphite anode, *J. Electrochem. Soc.* 151 (2004) A1659-A1669.
- [31] J. Vatamanu, O. Borodin, G.D. Smith, Molecular dynamics simulation studies of the structure of a mixed carbonate/LiPF₆ electrolyte near graphite surface as a function of electrode potential, *J. Phys. Chem. C* 116 (2012) 1114-1121.
- [32] X. Chen, X.Q. Zhang, H.R. Li, Q. Zhang, Cation-solvent, cation-anion, and solvent-solvent interactions with electrolyte solvation in lithium batteries, *Batteries Supercaps* 2 (2019) 128-131.
- [33] X.Q. Zhang, X. Chen, X.B. Cheng, B.Q. Li, X. Shen, C. Yan, J.Q. Huang, Q. Zhang, Highly stable lithium metal batteries enabled by regulating the solvation of lithium ions in nonaqueous electrolytes, *Angew. Chem. Int. Ed.* 57 (2018) 5301-5305.
- [34] S. Zhu, C. Xing, W. Xu, Z. Li, Hydrogen bonding and halogen bonding co-existing in the reaction of heptafluorobenzyl iodide with N, N, N', N'-tetramethylethylene diamine, *Tetrahedron Lett.* 45 (2004) 777-780.
- [35] N. Q. Liang, J. H. Fang, X. X. Guo, A simple approach for preparation of porous polybenzimidazole membranes as a promising separator for lithium ion batteries, *J. Mater. Chem. A* 5 (2017) 15087-15095.
- [36] R. Zhang, X. R. Chen, X. Chen, X. B. Cheng, X.Q. Zhang, C. Yan, Q. Zhang, Lithiophilic sites in doped graphene guide uniform lithium nucleation for dendrite-free lithium metal anodes, *Angew. Chem. Int. Ed.* 56 (2017) 7764-7768.
- [37] A. Pei, G. Zheng, F. Shi, Y. Li, Y. Cui, Nanoscale nucleation and growth of electrodeposited lithium metal, *Nano Lett.* 2017, 17 (2017) 1132-1139.
- [38] A. Milchev, M.I. Montenegro, A galvanostatic study of electrochemical nucleation, *J. Electroanal. Chem.* 333 (1992) 93-102.
- [39] R. Weber, M. Genovese, A.J. Louli, S. Hames, C. Martin, I.G. Hill, J.R. Dahn, Long cycle

- life and dendrite-free lithium morphology in anode-free lithium pouch cells enabled by a dual-salt liquid electrolyte, *Nat. Energy* 4 (2019) 683–689.
- [40] Z. Xie, Z. Wu, X. An, X. Yue, P. Xiaokaiti, A. Yoshida, A. Abudula, G. Guan, A sandwich-type composite polymer electrolyte for all-solid-state lithium metal batteries with high areal capacity and cycling stability, *J. Membr. Sci.* 596 (2020) 117739.
- [41] K. Park, J. B. Goodenough, Dendrite-suppressed lithium plating from a liquid electrolyte via wetting of Li_3N , *Adv. Energy Mater.* 7 (2017) 1700732.
- [42] H. Kim, F. Wu, J. T. Lee, N. Nitta, H. T. Lin, M. Oschatz, W. I. Cho, S. Kaskel, O. Borodin, G. Yushin, In situ formation of protective coatings on sulfur cathodes in lithium batteries with LiFSI-based organic electrolytes, *Adv. Energy Mater.* 5 (2015) 1401792.
- [43] C. Yan, Y. X. Yao, X. Chen, X. B. Cheng, X. Q. Zhang, J. Q. Huang, Q. Zhang, Solvation chemistry of lithium nitrate in carbonate electrolyte for high-voltage lithium metal battery, *Angew. Chem. Int. Ed.* 130 (2018) 14251–14255.
- [44] H.T.T. Le, D.T. Ngo, V.C. Ho, G.Z. Cao, C.N. Park, C.J. Park, Insights into degradation of metallic lithium electrodes protected by a bilayer solid electrolyte based on aluminium substituted lithium lanthanum titanate in lithium-air batteries, *J. Mater. Chem. A* 4 (2016) 11124–11138.
- [45] N. Wang, B.Z. Lu, L.G. Li, W.H. Niu, Z.H. Tang, X.W. Kang, S.W. Chen, Graphitic nitrogen is responsible for oxygen electroreduction on nitrogen-doped carbons in alkaline electrolytes: Insights from activity attenuation studies and theoretical calculations, *ACS Catal.* 8 (2018) 6827–6836.
- [46] R. Wang, X. Li, Z. Wang, H. Zhang, Electrochemical analysis graphite/electrolyte interface in lithium-ion batteries: p-toluenesulfonyl isocyanate as electrolyte additive, *Nano Energy* 34 (2017) 131–140.

- [47] L. Wang, Y. Ma, P. Wang, S. Lou, X. Cheng, P. Zuo, C. Du, Y. Gao, G. Yin, Interface modifications by Tris(2,2,2-trifluoroethyl) borate for improving the high-voltage performance of $\text{LiNi}_{1/3}\text{Co}_{1/3}\text{Mn}_{1/3}\text{O}_2$ cathode, *J. Electrochem. Soc.* 164 (2016) A1924-A1932.
- [48] J. Alvarado, M.A. Schroeder, T.P. Pollard, X. Wang, J.Z. Lee, M. Zhang, T. Wynn, M. Ding, O. Borodin, Y.S. Meng, K. Xu, Bisalt ether electrolytes: a pathway towards lithium metal batteries with Ni-rich cathodes, *Energ Environ. Sci.* 12 (2019) 780-794.
- [49] X. Shanguan, G. Xu, Z. Cui, Q. Wang, X. Du, K. Chen, S. Huang, G. Jia, F. Li, X. Wang, D. Lu, S. Dong, G. Cui, Additive-assisted novel dual-salt electrolyte addresses wide temperature operation of lithium-metal batteries, *Small* 15 (2019) 1900269.
- [50] B. Tong, J.W. Wang, Z.J. Liu, L. Ma, P. Wang, W.F. Feng, Z.Q. Peng, Z.B. Zhou, $(\text{CH}_3)_3\text{Si-N}[(\text{FSO}_2)(\text{n-C}_4\text{F}_9\text{SO}_2)]$: An additive for dendrite-free lithium metal anode, *J. Power Sources* 400 (2018) 225-231.

Chapter 6 Conclusions and Prospect

6.1 Conclusions

Lithium metal batteries (LMB) are very attractive owing to their high energy density as well as low gravimetric density. Recently, persistent efforts have been devoted to suppressing the formation of Li dendrites and improving the cycling stability of LMBs. In this study, three different electrolyte formulations, i.e., quasi-solid-state electrolyte, solid-state-electrolyte and practical liquid electrolyte were prepared for LMBs, respectively. Among all of those proposed strategies, owing to the stable electrode/electrolyte interfaces and decreased side reactions, the obtained LMBs exhibited substantially enhanced cyclability. Moreover, the solid electrolyte interface formation mechanism in electrolyte system has been deeply investigated by the experimental analysis together with molecular scale modeling.

Chapter 1: the main progress and remaining obstacles for the development of LMBs are comprehensively discussed, the feasibility and limitations of the state-of-the-art LMBs designs are also emphasized, and then the objectives of this research were stated.

Chapter 2: various chemical reagents, characterization technologies, and Electrochemical measuring methods were displayed.

Chapter 3: the PEO-Li salt based flexible electrolyte of PEO₈-LiTFSI-15% TBPHP and PEO₈-LiTFSI-TBPHP-12.5% LLZTO were fabricated and applied in quasi-solid-state LMBs. Based on the experimental investigations and DFT calculations, the TBP⁺ cation and HP⁻ anion of TBPHP ionic liquid played significant roles in adjusting the crystallization of PEO and enhancing lithium-

ion transference number of t_{Li^+} , respectively. Meanwhile, the addition of fast-ion conductor ceramic filler of the LLZTO further improved the performance of the battery in terms of ionic conductivity, rigid strength, thermal and electrochemical stability of SPEs. As a result, PEO₈-LiTFSI-TBPHP-12.5% LLZTO SPE revealed a satisfied ionic conductivity of $9.39 \times 10^{-4} \text{ S} \cdot \text{cm}^{-1}$, a wide electrochemical window of more than 5.0 V and a high t_{Li^+} of 0.63 at 50 °C. Moreover, the quasi-solid-state LiFePO₄|Li battery assembled with the PEO₈-LiTFSI-TBPHP-12.5% LLZTO SPE exhibited excellent rate performance, coulombic efficiency and cycle stability with negligible discharge capacity decay in 100 cycles at 50 °C, indicating that it has a high potential to be applied in LMBs.

Chapter 4: a proof-of-concept sandwich-type CPE, PEO₈-LiTFSI/PVDF-HFP-15%LLZTO/PEO₈-LiTFSI membrane for low cell operating temperature, was successfully fabricated. It is found that the PEO-LiTFSI layers in two sides of the PVDF-HFP-LLZTO membrane ameliorated the ion conductivity, improved the intimate contact with the electrodes and suppressed the lithium dendrite growth for stabilizing the battery. Meanwhile, the crystallinity of PEO and PVDF-HFP polymer matrix also reduced greatly owing to the cross-linking between each other at the interfacial sections. With the synergistic effects of ceramics electrolyte filler and the low-crystallinity polymer matrix, the faster Li⁺ ions transportation ability of the CPE was obtained. As a result, the sandwich-type CPE membrane revealed a satisfied ionic conductivity of $3.3 \times 10^{-4} \text{ S} \cdot \text{cm}^{-1}$, a wide electrochemical window of over 5.0 V and a high t_{Li^+} of 0.52 at 40 °C. Moreover, the all-solid-state LiFePO₄|sandwich-type CPE| Li metal battery with a high areal capacity cathode (1.5 mAh cm^{-2}) exhibited excellent rate performance, high coulombic efficiency and long-term cycle stability with negligible discharge capacity decay from 100 to 300 cycles at 40 °C. Furthermore, the fabricated flexible pouch cell also had excellent performance. Meanwhile, the

all-solid-state LiCoO_2 (1.5 mAh cm^{-2})|Li-metal and $\text{LiNi}_{1/3}\text{Mn}_{1/3}\text{Co}_{1/3}\text{O}_2$ (1.5 mAh cm^{-2})|Li-metal battery assembled with this sandwich-type CPE membrane also exhibited high-voltage stability along with a satisfied energy density, indicating that this sandwich-type CPE membrane had a high potential to be applied in the next generation ASSLMs.

Chapter 5: to achieve a higher energy density with better compatibility for the widespread deployment of LMBs, a reliable electrolyte additive of 2-FP was successfully applied in the commercial carbonate-based as well as ether-based electrolytes for the long lifespan LMBs. When using this additive to assemble the LMBs with high areal capacity and high-voltage cathode cathodes, the obtained LMBs exhibited substantially enhanced high voltage cyclability and high energy density. When combining with the DFT calculations, it is confirmed that the 2-FP electrolyte additive not only plays a critical role in decreasing the nucleation and deposition overpotentials, but more importantly also induces the generation of the robust and dense SEI layer enriched with LiF and Li_3N components that can effectively suppress the parasitic reactions between Li metal and electrolyte and permit the prompt transport of Li^+ ions. Furthermore, the quantum chemistry calculations also verified that the reduction of the 2-FP molecule is inclined to break of the C-F bond so that the F atom is easily detached from the 2-FP molecule to form a stable SEI consisting of LiF during its preferential reduction process. It is expected that such a 2-FP electrolyte additive could be added to commercial electrolytes with various voltage windows for the improvement of the performances of next-generation LMBs.

6.2 Prospect

Since the early 1960s witnessed the first wave of enthusiasm in Li metal-based batteries, the Li metal is always considered as a “Holy Grail” anode for rechargeable batteries. However, Li metal anode has the dendrite issues, causing safety concerns, low energy efficiency, and short

lifespan of LMBs, which severely hamper their practical applications. Although tremendous efforts have been devoted to extending the cycle life of LMBs over the past decades, there still remain many challenges that need to be addressed in order to meet the benchmark requirements for commercialization of LMBs. Now armed with the capabilities in tailoring materials at molecular level, the advanced *in situ* characterization technologies, and the unprecedented power to compute, researchers are revisiting the Li metal anode [1-4]. As a summary, the following points should be considered in the future research and development of LMBs:

1. The micro- and nano-structures of current collector substrate could affect the long-term cycling stability of LMBs. However, it should be noted that the subsequent deposition of Li metal on it relies more on the electrolyte components. Thus, in the design of current collector substrate, the properties of the electrolyte should be also considered. Moreover, it is suggested to analyze the relative difference between theoretical simulations and actual results, which could open a new way for the design and fabrication of novel current collector substrates.
2. Designing of an artificial interface layer in the LMBs could greatly improve the performance. However, the economic viability and particles/solvent emissions originated from the complex physical-chemical deposition or spinning technology may limit the practical fabrication process, which will finally affect the commercialization process.
3. The electrolyte formulation is the center in the development of LMBs, which plays the key role in reducing the depletion of active Li as well as prolonging the cycle lifespan, and more importantly, provides broad compatibility with the current manufacturing industry of LIBs. Much more efforts should be devoted to the further development of effective electrolyte formulations, especially for the solid-state electrolyte formulations in the all-solid-state LMBs since it will be valuable for the next-generation low cost as well as safe high-energy-

density batteries. In addition, pursuing extremely high mechanical strength of solid-state-electrolyte is proved to be meaningless.

4. The volume expansion of Li metal anode during the Li plating/stripping process will lead to the pressure increasing on the battery components, which also needs to be considered, especially in parallel stacking cells.
5. It is expected to adopt a high-energy density cathode with a large active material mass loading, lean electrolyte (e.g. $\sim 3 \text{ g Ah}^{-1}$ for liquid electrolyte), reduced inactive materials, and fast-charging rate to meet the practical evaluation of LMBs.
6. In consideration of low abundance of Li in the earth's crust and the high cost of the ultrathin Li foil, the anode-free Lithium metal batteries, also called zero-excess Li anode, should be regarded as a candidate for next-generation high-energy density batteries [5].
7. A proof-of-concept Li-reservoir cathode is considered one of the most promising options to eliminate irreversible capacity loss and enhance the cycling stability of in-situ enabled anode-free Lithium metal batteries. Moreover, such Li-contributors, like $\text{Li}_{1+x}\text{Ni}_{0.5}\text{Mn}_{1.5}\text{O}_4$, $\text{Li}_{1+x}\text{VPO}_4\text{F}$, $\text{Li}_x\text{Mn}_2\text{O}_4$ and Li_6CoO_4 can also match with the pre-lithiated sulfur cathode or its intercalation compounds to further increase the energy density of LMBs.
8. A great motivation in exploiting Na metal anodes is their abundance and low cost of raw materials. Na metal battery is qualified owing to abundant sodium resources in nature and much lower cost. The Mg, along with other more abundant alkali metal anodes are also considered as the candidates for the next-generation alkali metal battery designs.
9. Further understanding of plating/stripping behaviors of alkali metals by combining theoretical modelling with advanced cryogenic electron microscopy and in-situ observation techniques, and continuous innovation in the field of interdisciplinary researches on high-energy density alkali metal battery could realize remarkable breakthrough.

References

- [1] K. Xu, Electrolytes and Interphases in Li-Ion Batteries and Beyond, *Chem. Rev.* 114 (2014) 11503–11618.
- [2] J. Xiao, How lithium dendrites form in liquid batteries, *Science*, 366 (2019) 426-427.
- [3] H. Li, Practical evaluation of Li-ion batteries, *Joule*, 3 (2019) 908-919.
- [4] M. Winter, B. Barnett, K. Xu, Before Li ion batteries, *Chem. Rev.* 118 (2018) 11433–11456.
- [5] R. Weber, M. Genovese, A.J. Louli, S. Hames, C. Martin, I.G. Hill, J.R. Dahn. Long cycle life and dendrite-free lithium morphology in anode-free lithium pouch cells enabled by a dual-salt liquid electrolyte, *Nat. Energy* 4 (2019) 683-689.

List of publications and presentations

Publications

- ① **ZHENGKUN XIE**, Zhijun Wu, Xiaowei An, Akihiro Yoshida, Zhongde Wang, Xiaogang Hao, Abuliti Abudula*, Guoqing Guan*, Bifunctional ionic liquid and conducting ceramic co-assisted solid polymer electrolyte membrane for quasi-solid-state lithium metal batteries, *Journal of Membrane Science*, 586 (2019) 122-129.
- ② **ZHENGKUN XIE**, Zhijun Wu, Xiaowei An, Xiyan Yue, Xiaokaiti Pairuzha, Akihiro Yoshida, Abuliti Abudula*, Guoqing Guan*, A sandwich-type composite polymer electrolyte for all-solid-state lithium metal batteries with high areal capacity and cycling stability, *Journal of Membrane Science*, 596 (2020) 117739.
- ③ **ZHENGKUN XIE**, Zhijun Wu, Xiaowei An, Xiyan Yue, Akihiro Yoshida, Xiao Du, Xiaogang Hao, Abuliti Abudula*, Guoqing Guan*, 2-Fluoropyridine: a novel electrolyte additive for lithium metal batteries with high areal capacity as well as high cycling stability, *Chemical Engineering Journal*, 393 (2020) 124789.
- ④ **ZHENGKUN XIE**, Zhijun Wu, Xiaowei An, Xiyan Yue, Jiajia Wang, Abuliti Abudula*, Guoqing Guan*, Anode-free rechargeable lithium metal batteries: progress and prospects, *Energy storage materials*, 32 (2020) 386-401.
- ⑤ **ZHENGKUN XIE**, Xiaowei An, Zhijun Wu, Xiyan Yue, Jiajia Wang, Xiaogang Hao, Abuliti Abudula*, Guoqing Guan*, Fluoropyridine family: Bifunction as electrolyte solvent and additive to achieve dendrites-free lithium metal batteries, *Journal of Materials Science & Technology*, (In revision).
- ⑥ Zhijun Wu, **ZHENGKUN XIE**, Akihiro Yoshida, Zhongde Wang, Xiaogang Hao, Abuliti Abudula, Guoqing Guan*, Utmost limits of various solid electrolytes in all-solid-state

lithium batteries: A critical review, *Renewable & Sustainable Energy Reviews*, 109 (2019) 367-385.

- ⑦ Zhijun Wu, **ZHENGKUN XIE**, Akihiro Yoshida, Xiaowei An, Zhongde Wang, Xiaogang Hao, Abuliti Abudula, Guoqing Guan*, Novel SeS₂ doped Li₂S-P₂S₅ solid electrolyte with high ionic conductivity for all-solid-state lithium sulfur batteries, *Chemical Engineering Journal*, 380 (2020) 122419.
- ⑧ Zhijun Wu, **ZHENGKUN XIE**, Akihiro Yoshida, Jing Wang, Tao Yu, Zhongde Wang, Xiaogang Hao, Abuliti Abudula, Guoqing Guan*, Nickel phosphate nanorod-enhanced polyethylene oxide-based composite polymer electrolytes for solid-state lithium batteries, *Journal of Colloid and Interface Science*, 565 (2020) 110-118.
- ⑨ Zhijun Wu, **ZHENGKUN XIE**, Jing Wang, Tao Yu, Xiao Du, Zhongde Wang, Xiaogang Hao, Abuliti Abudula, Guoqing Guan*, Simultaneously enhancing the thermal stability and electrochemical performance of solid polymer electrolytes by incorporating rod-like Zn₂(OH)BO₃ particles, *International Journal of Hydrogen Energy*, 45 (2020) 19601-19610.
- ⑩ Zhijun Wu, **ZHENGKUN XIE**, Jing Wang, Tao Yu, Zhongde Wang, Xiaogang Hao, Abuliti Abudula, Guoqing Guan*, A lithium-salt-containing ionic liquid incorporated Li-Al layered double hydroxide based solid electrolyte with high-performance and safety in solid-state lithium batteries, *ACS Sustainable Chemistry & Engineering*, 8 (2020) 12378-12387.
- ⑪ Xiyan Yue, Jiajia Wang, **ZHENGKUN XIE**, Amar M. Patil, Tao Yu, Xiao Du, Zhongde Wang, Xiaogang Hao, Abuliti Abudula*, Guoqing Guan*, Coral reef-like MoS₂ microspheres with 1T/2H phase as high-performance anode material for sodium ion batteries, *Journal of Material Science*, 55 (2020) 14389-14400.

International presentations

- ① **ZHENGKUN XIE**, Zhijun Wu, Xiyan Yue, Akihiro Yoshida, Abuliti Abudula, Guoqing Guan, “Effect of electrolyte additive on the performance of Lithium metal batteries”, 18th Asian Pacific Confederation of Chemical Engineering Congress (APCChE 2019), Sapporo, Hokkaido, Japan, September 23-27, 2019.
- ② **ZHENGKUN XIE**, Zhijun Wu, Xiyan Yue, Akihiro Yoshida, Tao Yu, Katsuki Kusakabe, Abuliti Abudula, Guoqing Guan, “Functional ionic liquid assisted commercial separator for advanced lithium metal batteries”, The 32nd International Symposium on Chemical Engineering (ISChE 2019), Chungnam National University, Daejeon, Korea, December 6-8, 2019.

Domestic presentations

- ① **ZHENGKUN XIE**, Akihiro Yoshida, Tao Yu, Abuliti Abudula, Guoqing Guan, “Novel electrochemical sensor for sensitive determination of hordenine based on BP particles modified carbon paste electrode”, The Society of Chemical Engineers, Japan (SCEJ) 83th Annual Meeting, Osaka, Japan, March 13-15, 2018.
- ② **ZHENGKUN XIE**, Zhijun Wu, Tao Yu, Akihiro Yoshida, Abuliti Abudula, Guoqing Guan, “Ionic liquid incorporated solid polymer electrolyte for all-solid-state lithium rechargeable batteries”, Joint Meeting of the Tohoku Area Chemistry Societies of 2018, Akita, Japan, September 15-16, 2018.

- ③ **ZHENGKUN XIE**, Zhijun Wu, Akihiro Yoshida, Abuliti Abudula, Guoqing Guan, “Sandwiched polymer-ceramics electrolyte for high voltage all-solid-state lithium rechargeable batteries”, The Society of Chemical Engineers, Japan (SCEJ) 84th Annual Meeting, Tokyo, Japan, March 13-15, 2019.
- ④ **ZHENGKUN XIE**, Zhijun Wu, Xiyan Yue, Tao Yu, Akihiro Yoshida, Abuliti Abudula, Guoqing Guan, " Enabling reliable lithium metal batteries by an organic electrolyte additive", The Electrochemical Society of Japan, ECSJ Fall Meeting, Yamanashi, Japan, September 5-6, 2019.
- ⑤ Zhijun Wu, **ZHENGKUN XIE**, Akihiro Yoshida, Abuliti Abudula, Guoqing Guan, “SeS₂ doped Li₂S-P₂S₅ glass-ceramic electrolyte with high ionic conductivity for all-solid-state lithium sulfur batteries”, Joint Meeting of the Tohoku Area Chemistry Societies of 2018, Akita, Japan, Sept 15-16, 2018.
- ⑥ Zhijun Wu, **ZHENGKUN XIE**, Akihiro Yoshida, Abuliti Abudula, Guoqing Guan, “A novel solid electrolyte of Li_{7+x}P_{3-x}Mo_xS_{11-2x}Se_{2x} for all-solid-state lithium-sulfur batteries”, The Society of Chemical Engineers, Japan (SCEJ) 84th Annual Meeting, Tokyo, Japan, Mar 13-15, 2019.
- ⑦ Zhijun Wu, **ZHENGKUN XIE**, Xiyan Yue, Jiajia Wang, Kitiphatpiboon Nutthaphak, Tao Yu, Akihiro Yoshida, Abuliti Abudula, Guoqing Guan, Simultaneously enhancing the thermal stability and electrochemical performance of solid polymer electrolytes by incorporating rod-like Zn₂(OH)BO₃ particles, The Electrochemical Society of Japan, ECSJ Fall Meeting, Yamanashi, Japan, Sept 5-6, 2019.

List of patents

- ① **謝正坤**、武志俊、吉田曉弘、官国清、阿布里提、関和治、“リチウムイオン伝導性ポリマー電解質”、出願番号：特願 2018-159952、出願日：2018 年 8 月 29 日.
- ② **謝正坤**、武志俊、吉田曉弘、官国清、阿布里提、関和治、“ポリマーセラミックス複合電解質膜”、出願番号：特願 2019-029487、出願日：2019 年 2 月 21 日.
- ③ **謝正坤**、武志俊、吉田曉弘、官国清、阿布里提、関和治、“電池用電解質及びその製造方法並びに二次電池”、出願番号：特願 2019-030552、出願日：2019 年 2 月 22
- ④ **謝正坤**、武志俊、吉田曉弘、官国清、阿布里提、関和治、“電解質用添加剤及びその製造方法”、出願番号：特願 2019-030549、出願日：2019 年 2 月 22 日.
- ⑤ **謝正坤**、武志俊、吉田曉弘、官国清、阿布里提、関和治、“電解質用添加剤、リチウムイオン二次電池用電解質及びリチウムイオン二次電池”、出願番号：特願 2019-105399、出願日：2019 年 6 月 5 日.
- ⑥ **謝正坤**、武志俊、吉田曉弘、官国清、阿布里提、関和治、“電解質用添加剤、リチウム二次電池用電解質及びリチウム二次電池”、出願番号：特願 2019-110272、出願日：2019 年 6 月 13 日.
- ⑦ **謝正坤**、官国清、武志俊、吉田曉弘、関和治、阿布里提、“電解質用添加剤、リチウム二次電池用電解質及びリチウム二次電池”、出願番号：特願 2019-155559、出願日：2019 年 8 月 28 日.
- ⑧ **謝正坤**、官国清、武志俊、吉田曉弘、関和治、阿布里提、“セパレータ用浸漬及び / 又は塗布剤、リチウム二次電池用セパレータ及びリチウム二次電池”、出願番号：特願 2019-155561、出願日：2019 年 8 月 28 日.

- ⑨ 謝正坤、官国清、岳喜岩、武志俊、吉田曉弘、阿布里提、関和治、“生物材料由来のハードカーボン、負極材料、負極、及びアルカリイオン電池”、出願番号：特願 2019-192989、出願日：2019 年 10 月 23 日.
- ⑩ 謝正坤、官国清、武志俊、岳喜岩、関和治、阿布里提、“二次電池用正極活物質前駆体、二次電池用正極活物質、二次電池用陰極液、二次電池用正極及び二次電池”、日本特許、出願番号：特願 2020-019666、出願日：2020 年 2 月 7 日.
- ⑪ 謝正坤、官国清、武志俊、岳喜岩、関和治、阿布里提、“電池用電解液及びリチウム電池”、日本特許、出願番号：特願 2020-102684、出願日：2020 年 6 月 12 日.
- ⑫ 武志俊、謝正坤、吉田曉弘、官国清、阿布里提、関和治、“ $\text{Li}_2\text{S}-\text{P}_2\text{S}_5-\text{SeS}_2$ 系ガラスセラミックからなる全固体リチウム硫黄電池用固体電解質、前記固体電解質に適した正極材料及びこれらの製造方法、並びにこれらを含む全固体リチウム硫黄電池”、出願番号：特願 2018-157667、出願日：2018 年 8 月 24 日.
- ⑬ 武志俊、謝正坤、吉田曉弘、官国清、阿布里提、関和治、“全固体二次電池用電解質”、出願番号：特願 2019-029489、出願日：2019 年 2 月 21 日.
- ⑭ 武志俊、官国清、謝正坤、吉田曉弘、関和治、阿布里提、“電解質用添加剤、固体電解質及びリチウムイオン二次電池”、出願番号：特願 2019-150307、出願日：2019 年 8 月 20 日.
- ⑮ 武志俊、官国清、謝正坤、関和治、阿布里提、“リチウムイオン電池用固体電解質及びその製造方法、リチウムイオン電池”、日本特許、出願番号：特願 2020-080743、出願日：2020 年 4 月 30 日.

Award

1. Excellent Student Recognition, Hirosaki University, Japan, March, 2020.